LLE Review

Quarterly Report

UR
LLE

1-μm defect, 5 μm into ablator

Wavefront in ice

C⁻ at shock-wave front

Trail from wave in ice

Wave in plastic

Cone of influence

Reflection from ablation front (from rarefaction-wave breakout)
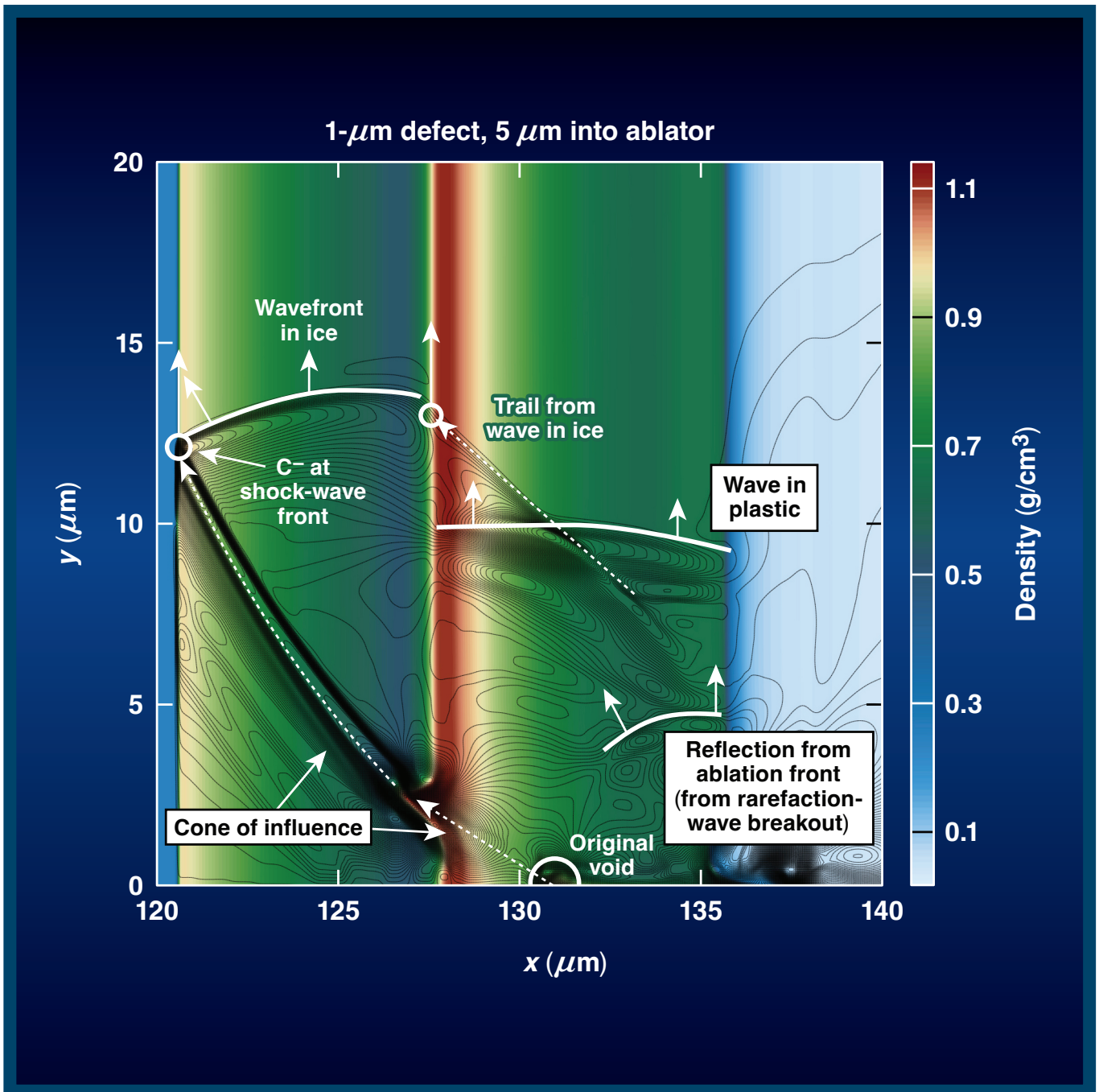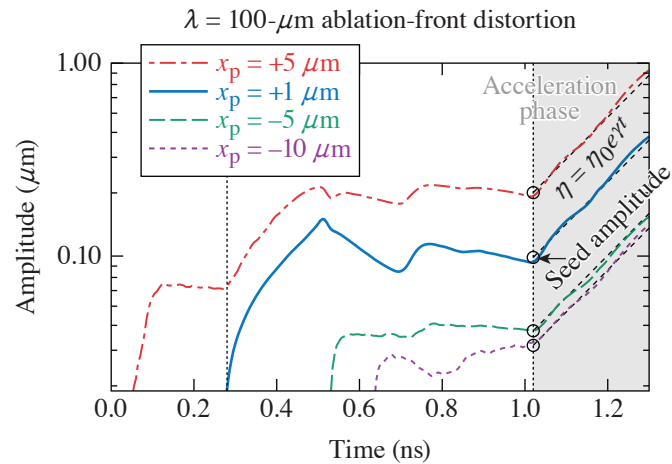
Original void

Density (g/cm³)

y (μm)

x (μm)

About the Cover:

The cover photo shows the density contour from a *Cygnus* simulation of a 2-D planar foil that contains a 1-μm defect located in the ablator (5 μm from the CH–DT interface). The color corresponds to density and the black lines correspond to y-velocity contours. The target accelerates from right to left, and the axis of symmetry is at $y = 0$. This shows the target after the first shock has passed through the CH–DT interface and into the ice. The shock front is located near $x = 121$ μm and the CH–DT interface is near $x = 128$ μm. The 1-D entropy wave that originates with the defect is labeled in the image just behind the CH–DT interface [near $(x, y) = (131, 0)$ μm]. In the image, perturbation information can be seen propagating along various ripples, after the shock has passed through the defect. When the shock interacts with the defect, the shock front becomes locally deformed. Since the perturbation wave has both x and y components, this deformation spreads laterally along the shock front, leaving a "trail" of vorticity in a cone-like manner, with its origin at the fluid trajectory of the original defect. The extent of this vorticity cone (labeled in the image by the dashed white line) is determined by the material sound speed, shock strength, and defect placement. As the original perturbation cone from the first shock front expands into the target, new waves (such as rarefaction waves) carry this updated information back to the ablation front. Additionally, the distortion laterally expands along the surface of the ablation front due to the 2-D nature of the flow.

Internal target defects create complex wave phenomena, yet simple single-mode (cosine) perturbations can provide clues as to how these complex wave dynamics evolve. In the image on the right, four different single-mode perturbations (λ = wavelength) are applied at different locations (x_p) relative to the interface within the ice or ablator material of a planar 2-D foil. This image shows that distortion growth is larger for large-wavelength modes that originate closer to the outer surface of the target due to shock transit time and the rarefaction wave created by the material interface.

$\lambda = 100$-μm ablation-front distortion

E30033JR

For questions or comments, contact Milton J. Shoup III, Editor, Laboratory for Laser Energetics, 250 East River Road, Rochester, NY 14623-1299, (585) 275-9636.

www.lle.rochester.edu

LLE Review
Quarterly Report

UR
LLE

Contents

In Brief

This volume of LLE Review 170 covers the period from January–March 2022. Articles appearing in this volume are the principal summarized results for long-form research articles. Readers seeking a more-detailed account of research activities are invited to seek out the primary materials appearing in print, detailed in the publications and presentations section at the end of this volume.

Highlights of research presented in this volume include:

- S. C. Miller and V. N. Goncharov model instability seeding mechanisms caused by internal defects in inertial confinement fusion targets (p. 1).

- A. Colaïtis *et al.* present detailed calculations that capture the persistent low-mode asymmetries evident in laser-direct-drive implosions on the OMEGA Laser System (p. 5).

- V. Gopalaswamy *et al.* present an analysis of limited coverage effects on areal-density measurements in inertial confinement fusion implosions on the OMEGA Laser System (p. 10).

- P. V. Heuer *et al.* report on diagnosing magnetic fields in cylindrical implosions with oblique proton radiography on the OMEGA Laser System (p. 16).

- L. S. Leal *et al.* model the effect of laser preheat in magnetized liner inertial fusion at the Omega Laser Facility (p. 19).

- K. M. Woo *et al.* present an analysis of core asymmetries in inertial confinement fusion implosions using 3-D hot-spot reconstruction of experimental data from the OMEGA Laser System (p. 21).

- J. R. Davies and P. V. Heuer conduct an evaluation of the direct inversion of proton radiographs in the context of cylindrical implosions (p. 24).

- H. Wen *et al.* report particle-in-cell modeling of plasma-jet merging in the large-Hall-parameter regime (p. 27).

- K. Weichman *et al.* present progress in modeling relativistic laser–plasma interaction with kilotesla-level applied magnetic fields (p. 30).

- G. Bruhaug *et al.* report the first single-shot electron radiography images using an electron beam from a 100-J-class laser-plasma accelerator (p. 35).

- G. Bruhaug *et al.* present on the development of a hardened THz energy meter for use on the kilojoule-scale, short-pulse OMEGA EP laser (p. 38).

- C. Dorrer and J. L Shaw demonstrate a single-shot cross-correlator based on the sum–frequency generation of counter-propagating beams in SBN61 ($Sr_xBa_{1-x}Nb_2O_6$ with $x = 0.61$) using the Multi-Terawatt laser ($\lambda_A = 1053$ nm) and the idler of the MTW-OPAL laser ($\lambda_B = 1170$ nm) (p. 41).

- K. L. Marshall *et al.* report on the multiparameter laser performance characterization of liquid crystals for polarization control devices in the nanosecond regime (p. 44).

- M. Sharpe, W. T. Shmayda, and J. Ruby report on the experimentally determined influence of heat treatments on the near-surface tritium concentration profiles in 316 stainless steel (p. 47).

- G. Chen *et al.* experimentally determine the electron effective mass in highly resistive GaAs by exploiting the influence of a magnetic field on optically excited transient THz surface emissions (p. 50).

- J. L. Peebles *et al.* provide an assessment of generating quasi-static magnetic fields using laser-driven "capacitor" coils (p. 53).

- R. B. Spielman discusses pulsed-power innovations for next-generation, high-current drivers (p. 57).

- J. Puth *et al.* summarize operations of the Omega Laser Facility during the second quarter of FY22 (p. 60).

Milton Shoup III
Editor

Instability Seeding Mechanisms due to Internal Defects in Inertial Confinement Fusion Targets

S. C. Miller and V. N. Goncharov

Laboratory for Laser Energetics and Department of Mechanical Engineering, University of Rochester

Performance degradation in laser-driven inertial confinement fusion implosions is caused by several effects, one of which is Rayleigh–Taylor instability growth. Target imperfections from manufacturing processes create instability seeds in the form of roughness or isolated "dome" features on the outer surface, gaps or separation between material layers, ice-layer roughness, and internal defects such as voids and bubbles. Additionally, tritium decay from the DT fuel can deposit energy into the ablator and DT ice layers and cause localized swelling in the plastic ablator material.1 A comprehensive understanding of seeding mechanisms is essential to characterize the impact of target defects on in-flight shell integrity and mass injection into the central, lower-density vapor region. An analysis of early-time behavior of both single-mode shell mass modulations and isolated voids is performed by examining the evolution of the acoustic waves launched by these target imperfections. A systematic study of localized perturbation growth as a function of defect placement and size is presented. The use of low-density ablator materials (such as foams) is suggested as a potential mitigation strategy to improve target robustness against the impact of defect-initiated growth.

A new parallel high-order multiphysics code (*Cygnus*[2]) is used to simulate internal ("bulk") perturbations inside the solid-density DT ice and plastic ablator materials. Perturbations are applied to planar 2-D foils (driven by a laser-like heat flux up to the start the acceleration phase) to study hydrodynamic wave propagation and seeding mechanisms at the ablation front. Convergence effects are not significant in early-time evolution, and the use of planar foils simplifies the analysis.

The foils used in this work are defined by three fluid regions: a 100-μm-thick, low-density $\rho = 0.001$-g/cm^3 layer representing the vapor region; a 40-μm-thick, $\rho = 0.25$-g/cm^3 layer representing DT ice; and an 8-μm-thick, heavier-density $\rho = 1$-g/cm^3 layer to mimic the plastic (CH) ablator. Density perturbations are applied in two forms: single-mode sinusoidal (to study basic seeding mechanisms) and isolated Gaussian voids (to closer mimic a realistic defect).

Figure 1 shows the trajectories of the ablation front, CH–DT interface, DT gas–ice interface, and two shocks created by the single-picket laser pulse (plotted in the lower pane). When shocks pass through an internal perturbation, such as a defect, a void in the material, or an interfacial gap, perturbation waves are launched that travel along characteristic hypersurfaces. For small perturbations decomposed into Fourier harmonics, each wave harmonic travels along characteristics defined as $(dx/dt)_{C^+} = U + c_s$ (the C$^+$ characteristic), as $(dx/dt)_{C^-} = U - c_s$ (the C$^-$ characteristic), and $(dx/dt)_e = U$ (the entropy wave that travels with the local fluid velocity), where U is local fluid velocity and c_s is local sound speed. These characteristic trajectories define how perturbations propagate throughout the target and deposit seeds for instability growth. In the event of a shock-perturbation interaction, the C$^+$ characteristic wave carries the information back to the ablation front, the C$^-$ characteristic wave catches up to and perturbs the shock front, and the entropy wave travels with the original defect (and defines the trajectory of the shock-induced vorticity).

Figure 2 shows the results from single-mode sinusoidal perturbations applied at various depths in the ice and ablator material of the foil. These depths are reported as relative to the CH–DT interface (where a positive value denotes a position inside the ablator material). Figure 2 plots the evolution of the distortion amplitude (peak to valley) of the ablation front due to perturbations with a single-mode wavelength of 100 μm. The time history of the ablation-front distortion shows the arrival of particular hydrodynamics waves such as shocks, rarefaction waves, and other characteristic waves. The two perturbations that start in the
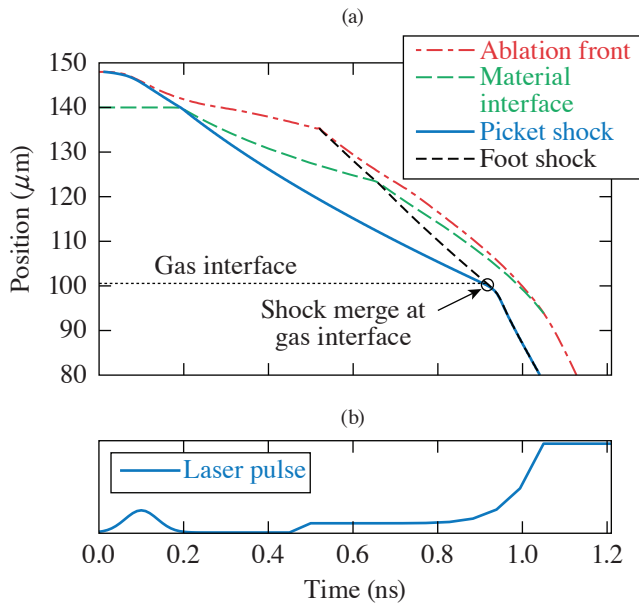
Figure 1
Interface and shock trajectories (position versus time) for the target and laser pulse.

E30028JR
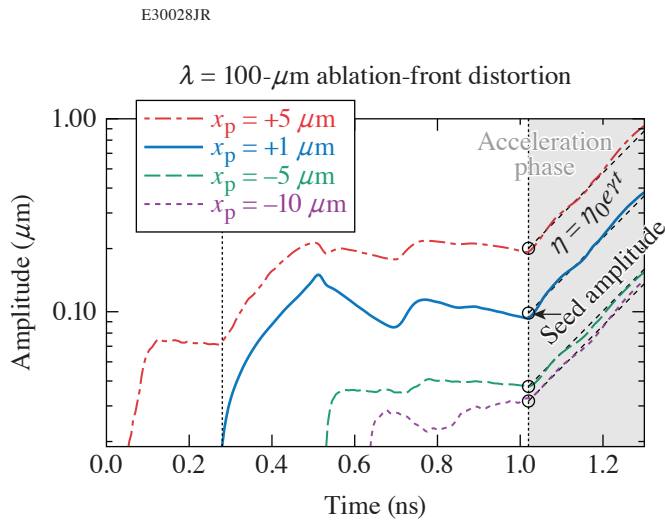
Figure 2
Ablation-front distortion history corresponding to perturbations at different locations in the ablator and DT ice. The acceleration phase is shaded in light gray. The dashed line is the exponential fit to $\eta = \eta_0 e^{\gamma t}$, and the seed amplitude is extracted from this curve. The initial perturbation depths (x_p) are +5, +1, –5, and –10 μm relative to the CH–DT interface for the red, blue, green, and purple lines, respectively. The vertical dotted black line near $t = 0.3$ ns indicae the arrival of the rarefaction wave at the ablation front.

E30033JR

ablator (red and blue curves) show significantly larger growth due to the rarefaction wave created by the interaction of the first shock (from the picket) and the CH-DT interface. This feedout growth process causes perturbations that start in the ablator to create larger seeds for instability growth when compared to those that originate in the ice. These seeds are defined as the amplitude of the distortion at the ablation front at the start of the acceleration phase (after which exponential RT growth occurs, or $\eta \sim \eta_0 e^{\gamma t}$, where γ is the growth rate and η is distortion). Figure 3 summarizes the seed amplitude (η_0) for perturbation wavelengths from 5 to 100 μm at different depths within the target material and shows the trend that perturbation seeds are largest when defects originate in the ablator and reduce as the initial position moves farther into the ice. As the wavelength reduces, however, interactions like destructive interference and phase change create wavelength-dependent behavior that complicates the position versus seed amplitude relationship. One region of particular interest [in Fig. 3(b)] is just inside of the CH–DT interface (near $x_p = -5$ μm). Here the interaction of the distorted CH–DT interface effectively cancels out or delays the onset of distortion growth at the ablation front (and reduces the acceleration-phase seed).

Simulations of isolated defects create complex wave interactions more likely to mimic target manufacturing defects, but much of the trends from single-mode perturbations apply. Figure 4(a) shows the density contour of the foil after the second shock has passed through a 1-μm defect (in the ablator). The black contour lines show velocity in the y direction and help to highlight
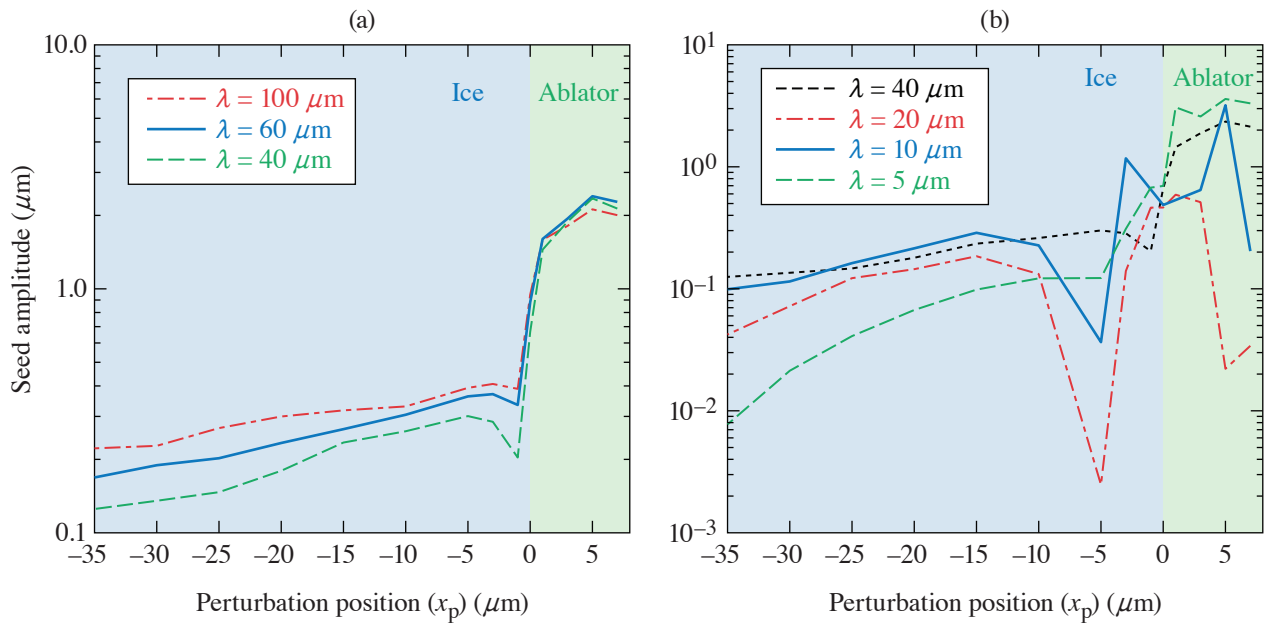
E30035JR

Figure 3

Scaled seed amplitudes as a function of perturbation position for (a) long-wavelength ($\lambda \geq 40$-mm) and (b) short wavelength ($\lambda < 40$-mm), single-mode perturbations.
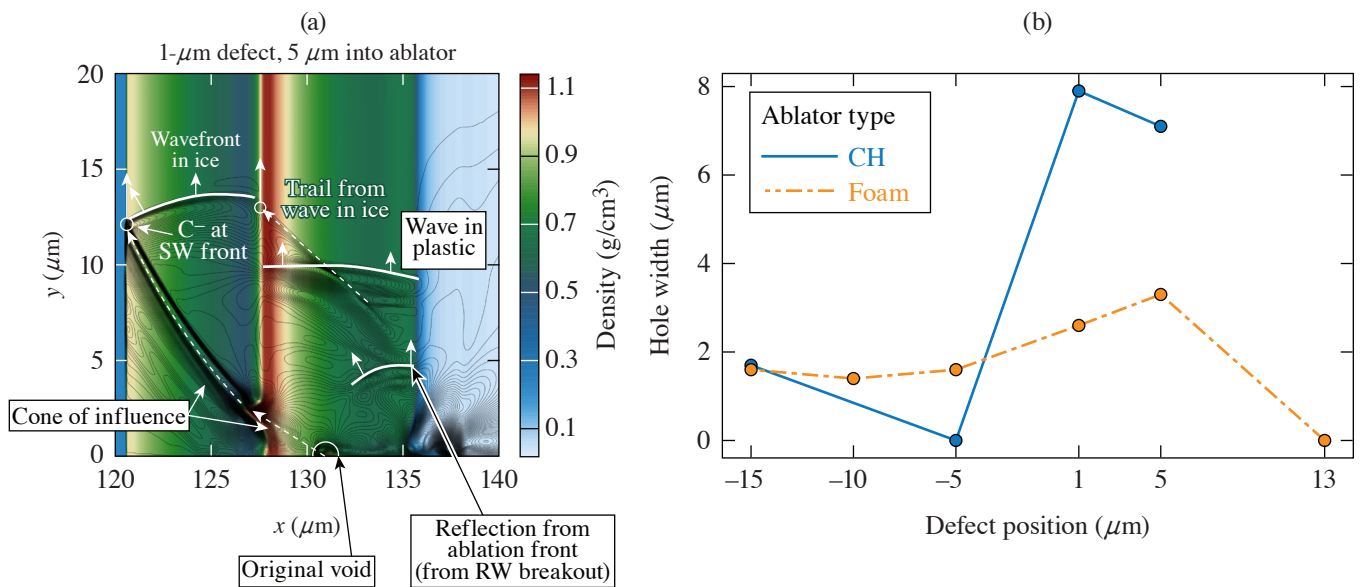
E30051JR

Figure 4

(a) Wave evolution for an isolated ablator defect (5 μm into the ablator from the CH–DT interface) at 0.5 ns after the first shock passage. Evolution in the y direction contributes to an extension of the maximum perturbation in y compared to the initial defect size. The contour colors show density and contour black lines show y velocity. (b) Hole sizes from shell punctures as a result of isolated defects in CH and wetted-foam targets approximately 300 ps after the start of the acceleration phase. RW: rarefaction wave; SW: shock wave.

particular wave features. These features include the wavefronts propagating through the different materials (ice and CH) and the lateral expansion of the defect perturbation. The lateral propagation is a unique feature of isolated defects (compared to sinusoidal perturbations). Isolated defect simulations show significant shell mass modulations and punctures at the start of the acceleration phase, depending on the position and size of the defect. Figure 4(b) shows the width of the hole due to a 1-μm defect located at various positions in the ice and ablator. Here, the degradation effects mimic the trend from short-wavelength, single-mode perturbations; ablator defects are more detrimental, and the effect is reduced just inward of the CH–DT interface.

A surrogate model that uses a wetted-foam ablator is proposed as a potential mitigation strategy to minimize the effects of manufacturing defects. In this design, the density is reduced from 1.0 (for CH) to 0.3 g/cm^3, and the shell thickness is increased to 26.7 μm (up from 8 μm) to conserve total shell mass compared to the CH ablator design. The smaller density reduces the strength of the rarefaction wave that travels from the ablator–ice interface (this rarefaction wave creates the large feedout growth shown in Fig. 1), and the increased thickness is beneficial because it isolates the defect perturbation (similar to how ice defects evolve). This effect can be seen in Fig. 4(b), where the foam ablator shows an overall reduction in hole width created by the defect.

Future work will examine internal defect evolution in 3-D and will include additional effects like convergent geometry along with and a more-detailed treatment of the materials (material-specific equations of state, radiation opacity, multiple materials, etc.). Additional work will seek to optimize shell thickness and continue to study alternative foam-like ablator designs.

1. D. R. Harding and W. T. Shmayda, Fusion Sci. Technol. **63**, 125 (2013).
2. S. C. Miller, "Hydrodynamic Instabilities in Inertial Confinement Fusion: Physics, Numerical Methods, and Implementation," Ph.D. Thesis, University of Rochester, 2022.

Three-Dimensional Simulations Capture the Persistent Low-Mode Asymmetries Evident in Laser-Direct-Drive Implosions on OMEGA

A. Colaïtis,[1] I. V. Igumenshchev,[2] D. H. Edgell,[2] D. Turnbull,[2] R. C. Shah,[2] O. M. Mannion,[2] C. Stoeckl,[2] D. W. Jacobs-Perkins,[2] A. Shvydky,[2] R. T. Janezic,[2] A. Kalb,[2] D. Cao,[2] C. J. Forrest,[2] J. Kwiatkowski,[2] S. P. Regan,[2] W. Theobald,[2] V. N. Goncharov,[2] and D. H. Froula[2]

[1]Université de Bordeaux, Centre Lasers Intenses et Applications, France
[2]Laboratory for Laser Energetics, University of Rochester

In this summary, detailed calculations are presented that include the first 3-D hydrodynamic simulations with sufficient physics models included to reproduce and quantify the anomalies observed in direct-drive implosions on OMEGA. When including all the known effects [polarized cross-beam energy transfer (CBET), mispointing, target offset], the simulations reproduce the measurements for bang time, yield, hot-spot flow velocity, and direction. To quantify these effects within the integrated experiments and describe the complex physical processes of polarized CBET and its interplay with multidimensional plasma hydrodynamics, an inline CBET model capable of accounting for polarization was implemented in a 3-D hydrodynamic code with a 3-D laser propagation solver. These integrated simulations were used to assess the effect of unpolarized and polarized CBET, explore the sensitivity of current direct-drive experiments to the various low-mode sources, and assess the predictive capabilities of such detailed 3-D modeling tools—an important component of the inertial confinement fusion program. Notably, current levels of beam mispointing, imbalance, target offset, and asymmetry from polarized CBET were found to degrade yields by more than 40%. Finally, mitigation strategies are explored: attempting to compensate the mode-1 asymmetry with a preimposed target offset and redesigning the double polarization rotators. These results were summarized in Ref. 1 and detailed in Refs. 2 and 3.

For the past few years, direct-drive implosion experiments conducted on the OMEGA Laser System[4] have reached a sufficient degree of control such that the errors induced by beam power imbalance, beam pointing inaccuracy, and target offset are relatively small. Despite these improvements, a large flow anomaly is still observed across many experiments, with a flow direction that appears systematic[5] (Fig. 1). Recently, it was proposed in Ref. 6 that a potential source of systematic low modes on the OMEGA laser[4] originates from polarized CBET. According to the authors of Ref. 6, the polarization dependency of CBET induces a significant low-mode anomaly in the laser drive, with its direction (in terms of spherical harmonics mode $\ell = 1$) being consistent with typical measured flow velocities from neutron diagnostics. Conclusions were reached, however, using post-processing of 1-D hydrodynamics simulations, which do not allow for a quantitative assessment of the final influence of polarized CBET on measured flow velocity and direction, for which inline modeling is required. Moreover, accounting for the compounded effect of beam balance, beam pointing error, and target offset in addition to polarized CBET requires a 3-D modeling of both the laser and hydrodynamics.

This lead to the development of the first inline-capable polarized CBET model, implemented within the inverse ray-tracing framework of the *IFRIIT*[7] code. Inline simulations were performed using a heterogeneous multiple-data, multiple-program framework coupling the *ASTER*[9,10] 3-D radiation-hydrodynamic code with the *IFRIIT*[7,10] 3-D laser propagation solver, running on 6000 cores of the French Commission for Atomic Energy and Alternative Energies' Très Grand Centre de Calcul (CEA TGCC) supercomputer, making it possible to describe the complex physical processes of polarized CBET and its interplay with plasma hydrodynamics. These integrated simulations were used to (1) quantify the sensitivity of current target designs to the best setup performances of the OMEGA Laser System, (2) assess if the source of the systematic flow can be identified, and (3) test various strategies for mitigation of the low-mode asymmetries.
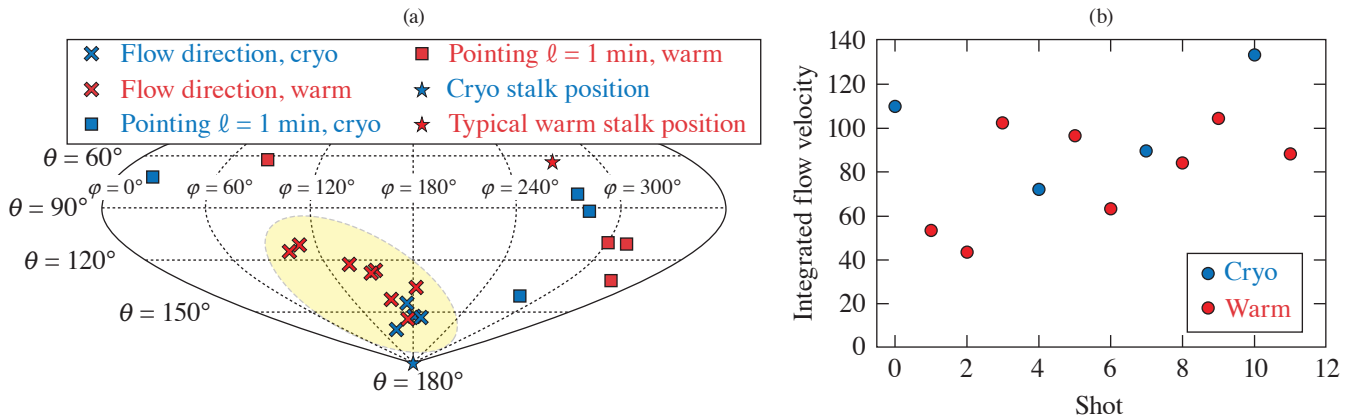
TC16211JR

Figure 1

(a) Fusing DT flow direction shown in a sinusoidal projection of the OMEGA chamber and (b) associated flow magnitude in km/s in best-setup implosions (see also Refs. 5 and 11). The yellow region highlights the systematic anomaly.

The inline polarization model proposed here was developed within the field formulation of geometrical ray optics. The ray electric field is written $a = A \exp k_0 \psi$, where k_0 is the vacuum wave number, A is the field swelling due to refraction, and ψ is a phase that includes the effects of absorption and energy exchange. The field at caustics is described using an etalon integral method,[12] which allows reconstruction of the Airy pattern without introducing free parameters. The ray field is then described onto the Frenet reference frame,[13] an orthogonal basis associated with the ray and defined at every point by a tangent $\mathbf{1} = \mathbf{k}/|\mathbf{k}|$, a normal ν parallel to the permittivity gradient component transverse to the ray, and a binormal $\mathbf{b} = \mathbf{1} \times \nu$. The Frenet frame rotates with the ray, which allows for local accounting of polarization transport through refraction. The exchange of amplitude between the ray-field components in the Frenet frame, denoted $(A_n)^T = (a_{n,\nu_n}, a_{n,b_n})$ for field n, can be written[13] as $\partial_{1_n} A_n = \underline{\underline{D_n}} A_n$ with $\underline{\underline{D_n}}$ a tensor that accounts for three polarization effects: polarization rotation due to refraction, polarization rotation of the probe beam toward the pump beam, and ellipticity induced in the initially linear polarizations due to CBET-induced plasma birefringence.

In the final model, the ray amplitude A is computed according to ray theory from a single inverse ray-tracing step,[14] while the ray phase is obtained by integrating the permittivity along the ray trajectory, $\psi = \int \varepsilon'' [\mathbf{r}(\hat{\tau}) d\hat{\tau}/2]$, which includes ε'', the effect of polarized CBET from $\underline{\underline{D_n}}$, as well as collisional absorption and Langdon effect.[10,15] Pump depletion is obtained by iterating the ray phase computation until convergence. The final formulation of the laser propagation model has no free parameters, contrary to what is commonly used in inline CBET models to either limit caustic fields or tune the CBET interaction.[16–19] This polarized CBET model was validated against academic test cases and against the *BeamletCrosser* post-processor[2,6] and is now used in inline 3-D *ASTER/IFRIIT*[9,10] simulations. The full polarized CBET model and its validation are presented in Ref. 2.

The 12 shots reported in Fig. 1 span 19 months of operation and were obtained with good performance metrics for beam pointing, beam balance, offset error, target quality, and diagnostic quality. Out of these 12, three shots were modeled; 94343, 98755, and 98768. Among those, 94343 and 98768 are cryogenic shots, whereas 98755 is a warm plastic shot. Shot 98768 is a large-diameter shot with $D_t = 1012$ μm, while the others are smaller targets with $D_t \sim 980$ μm. To this set, we also add shot 94712 (Ref. 11), which was a cryogenic shot with poor pointing performances, contrary to the other three noted above. For these experiments, the beam pointing was measured at the beginning of the shot day. In addition, for shot 98755, pointing was also measured at the end of the shot day, providing two references. Finally, the ice-thickness uniformity was characterized using optical measurements prior to the shots. For the targets of interest, the ice layer nonuniformity was estimated to be less than the instrument resolution, i.e., <1% for the mode $\ell = 1$.

An extensive set of simulations was executed while varying the CBET model and/or the number of low-mode sources, which are included. The CBET model was toggled from off, to the commonly used unpolarized model[20] where the polarization effect for polarization-smoothed beams [e.g., distributed polarization rotation (DPR)] is modeled with fixed polarization and without any

rotation or ellipticity effects to the fully polarized model presented here. In all simulations, the Spitzer–Härm[21] heat conduction model was used at all times except in the first picket where the flux was limited with $f_{lim} = 0.1$ (Ref. 8).

The inline simulations are compared to various measurements: peak rise time of the neutron rate, yield, flow velocity magnitude, and direction. Several conclusions can be drawn from the simulations results for neutron data, some of which are reported in Fig. 2: (1) The CBET model alone gets nuclear bang time correctly, implying that the zero-order drive energetics are correct and well described by the model [Fig. 2(a)]. This also suggests that other effects not accounted for here, such as two-plasmon decay, do not significantly modify the total drive.[22] (2) Unpolarized and polarized CBET simulations with power balance and pointing variations get the neutron yield correct because both drive energetics and symmetry are important for the yield [Fig. 2(b)]. (3) Both CBET models with power balance and pointing variations match the flow velocity correctly for shot 94712 because the large pointing error dominates the low-mode sources. (4) Polarized CBET with power balance and pointing is needed to get the flow velocity correct for the more-accurately pointed shot 94343 (the low offset of 3.5 μm is seen to play a minor role). This indicates that the polarization effect becomes more important as other low-mode sources become smaller. The flow direction is reproduced correctly in all simulations as long as the effects of polarized CBET, beam imbalance, and beam pointing are accounted for. The full comparison to experiments is reported in Ref. 3.
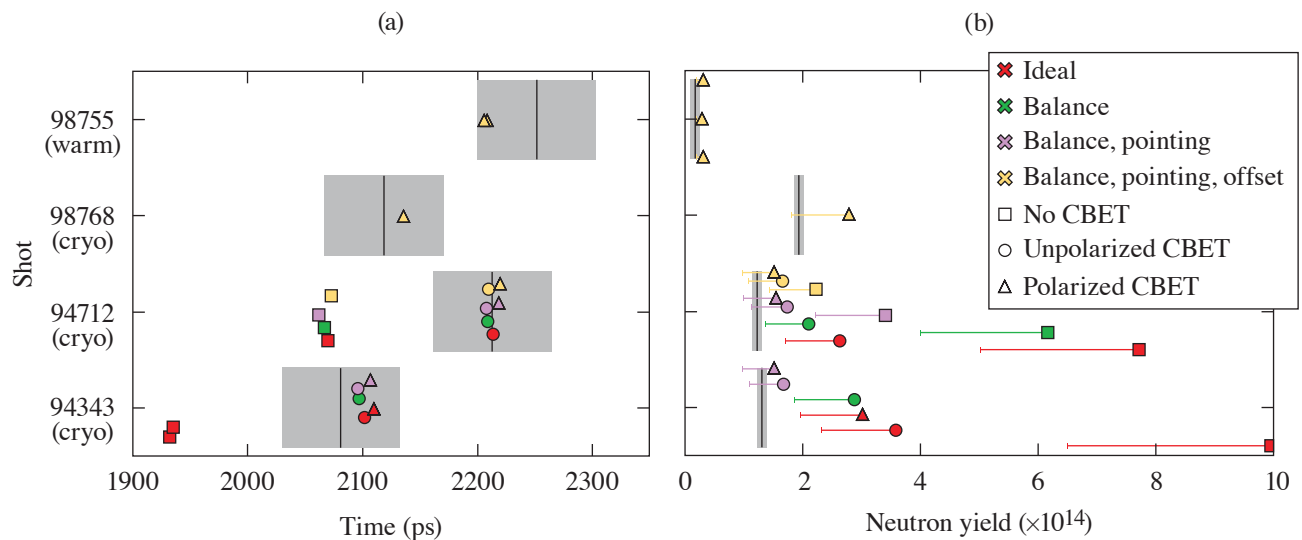
Figure 2

[(a),(b)] Comparison of the simulated (colored symbols) and measured (gray-shaded areas) (a) peak neutron rise time and (b) neutron yield. Simulations include a variety of low-mode sources and were conducted with and without CBET (see legends). Error bars on the simulated neutron yield account for the effect of small-scale mixing. Experimental yields are corrected for tritium aging.[23]

By examining the various simulations, it is observed that these best-setup OMEGA implosions lose ~40% in yield due to effects of balance, pointing, and offset alone [Fig. 3(a)]. In that framework, the polarization effect of CBET causes only a small drop in yield, by about 6%. However, in cases where there is no prior low-mode asymmetry from balance or pointing, the polarized CBET alone reduces the yield by 18% and induces an ~90-km/s flow anomaly compared to an unpolarized CBET case. In addition, the effect of unpolarized CBET alone reduces the yield by ~65% and amplifies the mode-10 anomaly by a factor of 2 to 3, leading to target perforation [Fig. 3(c)]. This is a strong argument for mitigation of the polarized CBET anomaly. It is observed, however, that the yield's dependency on low modes is more severe in cases without CBET because the latter was acting to mitigate drive asymmetries. These results highlight how CBET is a coupling loss mechanism that should be mitigated altogether in future driver designs.
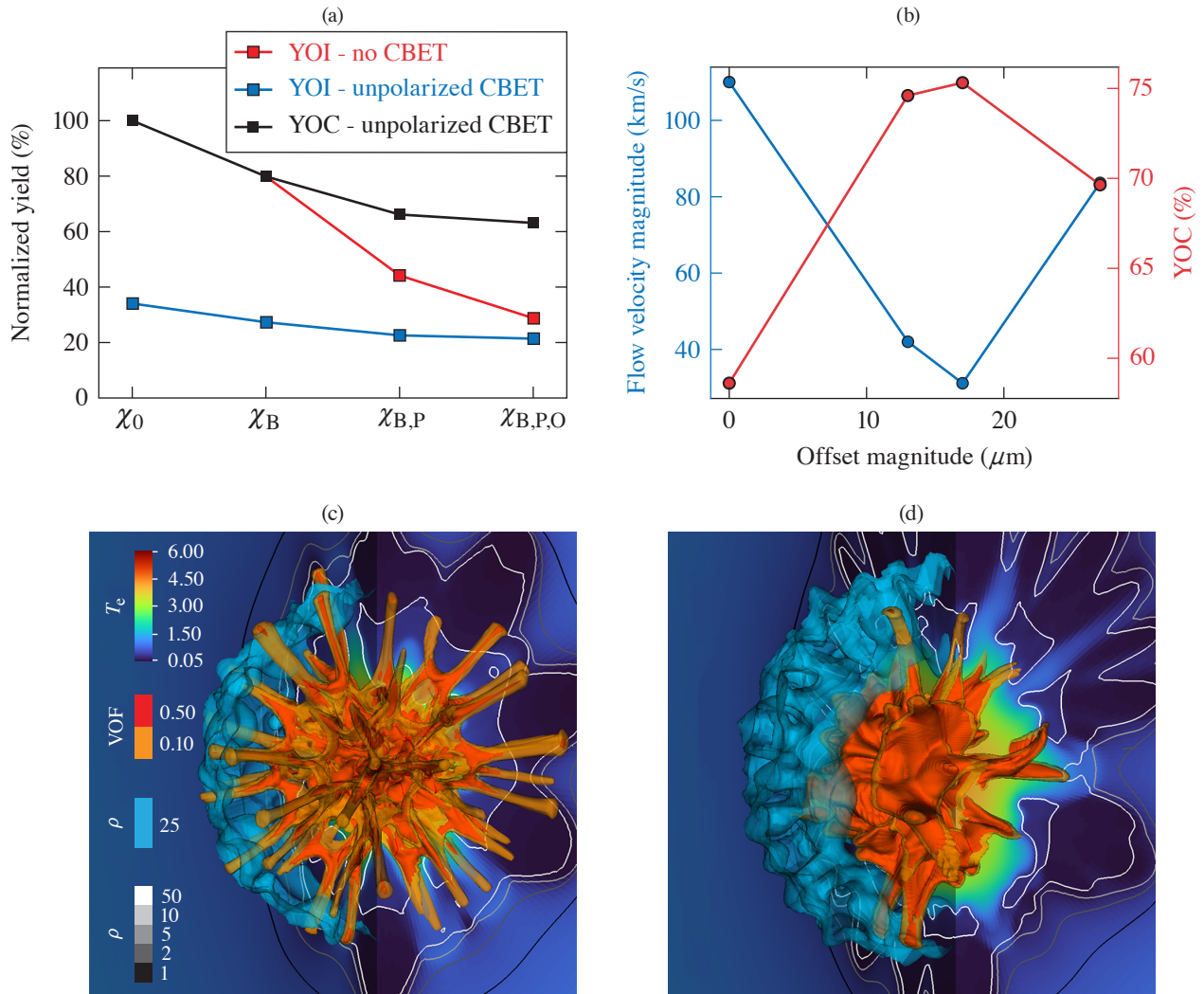
TC161213JR

Figure 3

(a) Scaling of the YOI (yield-over-ideal case in the absence of CBET) and YOC (yield-over-clean case in the presence of CBET) for simulations with and without unpolarized CBET, as a function of low-mode asymmetry sources (cases are labeled with a χ on the x axis; subscript 0 refers to the ideal case; B, P, and O indicate that beam balance, pointing, and offset were accounted for, respectively). (b) Flow anomaly (blue) and YOC (red) as functions of offset magnitude for a case with measured power balance and beam pointing ($\chi_{B,P}$). The target offset is in the opposite direction of the measured flow without offset. [(c),(d)] Target hot-spot electron temperature [colored background (keV)], 10% and 50% volume fraction of DT gas (orange and red volume contours, respectively), 25-g/cm^3 density isovalue (light blue volume contour), and 1-, 2-, 5-, 10-, and 50-g/cm^3 isocontours (black to white contour lines), for (c) an ideal case (χ_0) with unpolarized CBET. (d) A "real-setup" implosion accounting for power balance and beam pointing ($\chi_{B,P}$), with polarized CBET, is shown for comparison. All figures here relate to shot 94343.

Finally, two mitigation strategies are explored to compensate for the low-mode polarized CBET anomaly: offset compensation and DPR redesign. The offset compensation is able to increase the yield by ~15% [Fig. 3(b)] and reduce the modal $\ell = 1$ anomaly from the polarization effect by a factor of ~3. The offset compensation is not able to further improve the performances, however, due to the presence of other modes, notably from the polarized CBET anomaly but also from pointing and balance errors. Alternatively, considering a design of the DPR with only a 10-μm spot separation and half the smoothing by spectral dispersion (SSD) bandwidth, the simulations show that the flow direction and magnitude anomaly from the polarization effect disappear, and the unpolarized result is recovered. It is noted that halving the SSD bandwidth must be done in consideration of the potential effect on high mode-growth (not modeled here).

1. A. Colaïtis *et al.*, Phys. Rev. Lett. **129**, 095001 (2022).
2. A. Colaïtis *et al.*, "3-D Simulations of Implosions in Presence of Low Mode Asymmetries Part 1: Inline Polarized Cross Beam Energy Transfer Modeling," submitted to Plasma Physics and Controlled Fusion.
3. A. Colaïtis *et al.*, "3-D Simulations of Implosions in Presence of Low Mode Asymmetries Part 2: Systematic Flow Anomalies and Low Modes Impact on Performances on OMEGA," submitted to Plasma Physics and Controlled Fusion.
4. T. R. Boehly *et al.*, Opt. Commun. **133**, 495 (1997).
5. S. P. Regan *et al.*, Bull. Am. Phys. Soc. **66**, CO04.00011 (2021).
6. D. H. Edgell *et al.*, Phys. Rev. Lett. **127**, 075001 (2021).
7. A. Colaïtis *et al.*, Phys. Plasmas **26**, 072706 (2019).
8. I. V. Igumenshchev *et al.*, Phys. Plasmas **23**, 052702 (2016).
9. I. V. Igumenshchev *et al.*, Phys. Plasmas **24**, 056307 (2017).
10. A. Colaïtis *et al.*, J. Comput. Phys. **443**, 110537 (2021).
11. O. M. Mannion *et al.*, Phys. Plasmas **28**, 042701 (2021).
12. Yu. A. Kravtsov and Yu. I. Orlov, *Caustics, Catastrophes and Wave Fields*, 2nd ed., Springer Series on Wave Phenomena (Springer-Verlag, Berlin, 1993).
13. Yu. A. Kravtsov and N. Y. Zhu, *Theory of Diffraction: Heuristic Approaches*, Alpha Science Series on Wave Phenomena (Alpha Science International Ltd., Oxford, United Kingdom, 2010).
14. A. Colaïtis *et al.*, Phys. Plasmas **26**, 032301 (2019).
15. A. B. Langdon, Phys. Rev. Lett. **44**, 575 (1980).
16. I. V. Igumenshchev *et al.*, Phys. Plasmas **17**, 122708 (2010).
17. J. A. Marozas *et al.*, Phys. Plasmas **25**, 056314 (2018).
18. D. H. Edgell *et al.*, Phys. Plasmas **24**, 062706 (2017).
19. R. K. Follett *et al.*, Phys. Rev. E **98**, 043202 (2018).
20. P. Michel *et al.*, Phys. Plasmas **16**, 042702 (2009).
21. L. Spitzer, Jr. and R. Härm, Phys. Rev. **89**, 977 (1953).
22. D. Turnbull *et al.*, Phys. Rev. Lett. **124**, 185001 (2020).
23. A. Lees *et al.*, Phys. Rev. Lett. **127**, 105001 (2021).

Analysis of Limited Coverage Effects on Areal-Density Measurements in Inertial Confinement Fusion Implosions

V. Gopalaswamy,[1,2] R. Betti,[1,2,3] P. B. Radha,[1] A. J. Crilly,[4] K. M. Woo,[1] A. Lees,[1,2] C. A. Thomas,[1]
I. V. Igumenshchev,[1] S. C. Miller,[1,2] J. P. Knauer,[1] C. Stoeckl,[1] C. J. Forrest,[1] O. M. Mannion,[1,3,5] Z. L. Mohamed,[1,3]
H. G. Rinderknecht,[1] and P. V. Heuer[1]

[1]Laboratory for Laser Energetics, University of Rochester
[2]Department of Mechanical Engineering, University of Rochester
[3]Department of Physics and Astronomy, University of Rochester
[4]Imperial College London
[5]Sandia National Laboratories

To assess the quality of an inertial confinement fusion (ICF) experiment, various performance metrics based on the Lawson triple product[1–8] have been devised. These performance metrics must exceed a critical number to provide net energy gain. In direct-drive ICF implosions at the Omega Laser Facility,[9] the performance metric of interest is the so-called no-alpha normalized Lawson parameter χ

$$\chi = \rho R^{0.6} \left(0.12 \frac{Y_{16}}{M} \right)^{0.34}. \tag{1}$$

In an experiment, the areal density and yield can be diagnosed directly, while the stagnated DT mass can be estimated from simulations or from experimental data to infer χ. When χ is close to unity, alpha heating dominates the energetics of a hot spot, leading to ignition, which is a prerequisite for high-gain implosions. Due to the strong dependence of χ on the ρR, an accurate diagnosis is of critical importance. On OMEGA, an approach that synthesizes experiments and simulations[10–12] to create predictive models has led to dramatic increases in experimental performance, primarily through increases in neutron yield. References 10–12 present highly accurate predictive models for the neutron yield, but do not address the ρR—primarily because these models are not sufficiently accurate to drive experimental design. Achieving a comparable quality of predictive capability for ρR as exists for the yield is a necessary prerequisite for the predictive-model–driven campaign on OMEGA to optimize ρR since the effective "step-size" of an iterative scheme to improve the ρR is roughly bounded below by the prediction uncertainty.

One reason for the lack of predictive capability for ρR is that it is an inherently 3-D measurement with different diagnostics integrating over varying regions of the sphere relative to a fixed line of sight. A predictive model for the 1-D–equivalent ρR, which is what we are attempting to optimize in experiments, will have an uncertainty that is at least as large as this limited coverage error, which in turn sets the minimum step-size of the iterative scheme to improve the ρR in experiments.

To generate physically reasonable 3-D configurations for use in *IRIS*, the 3-D radiation-hydrodynamic simulation *ASTER*[13] is used. Three configurations are considered. In the first, the effect of illumination asymmetry arising from the beam geometry is considered. In the second and third configurations, the illumination resulting from a fixed beam size of $R_b = 330\ \mu$m is modulated with varying $\ell = 1$, $m = 0$ and $\ell = 2$, $m = 0$ perturbations, respectively, both aligned along the $+z$ axis. The detectors used are specified in Table I, and the detector permutations are specified in Table II. The MRS virtual detector simulates the action of the magnetic recoil spectrometer,[14] while the P7/H10 BS virtual detectors simulate the action of the neutron-time-of-flight (nTOF) backscatter measurement.[15] The P7/H10 FW virtual detectors simulate the action of a hypothetical forward scatter measurement

Table I: Detector configurations used in this work. See Table II for the permutations used. The P7 and H10 nTOF detectors are located at the center of P7 and H7 in the OMEGA target chamber, respectively. At the present time, the nTOF's are only capable of backscatter (BS) measurements. The forward scatter (FW) measurement on the nTOF's is under investigation.

| Detector	θ_{det} (rad)	ϕ_{det} (rad)
P7 FW	2.03	2.83
P7 BS	2.03	2.83
H10 FW	1.35	2.83
H10 BS	1.35	5.27

Table II: Detector perumutations that are considered in this work. Note that the MRS + P7BS permutation is the one that is currently used in OMEGA experiments. Due to the unique details of each detector and experiment, it is possible that some measurements may be compromised on certain experiments.

Configuration	P7 FW	P7 BS	H10 FW	H10 BS	MRS FW
MRS Only					
MRS + P7BS					
MRS + H10BS					x
MRS + P7/H10BS		x			x
MRS + P7/H10BS + P7FW		x		x	x
MRS + P7/H10BS + H10FW	x	x		x	x
All	x	x	x	x	x

from the nTOF's that are under investigation on OMEGA. Note that the "MRS + P7BS" permutation represents the currently used permutation on OMEGA to assess the 1-D–equivalent ρR. For each simulation, each permutation of detectors is evaluated for each pair of $(\theta,'\phi')$. The 1-D–equivalent ρR [that is, the areal density of a perturbed implosion that is appropriate to use in Eq. (1)], $\langle \rho R \rangle$, is calculated by a harmonic average over the observed ρL by virtual detectors that are distributed uniformly over the sphere, where the ρL of a particular virtual detector is the neutron-averaged path length integral of the density for all primary (i.e., not scattered) virtual particles binned in that virtual detector and is the best estimate of the "real" areal density that would be seen by that detector.

First, consider the highest ℓ-mode simulation case of the beam mode. At stagnation, the shell can be moderately to severely perturbed due to the driven mode.[12] However, ρR is inferred in experiments from integrals over the neutron spectrum, which corresponds (assuming a point source) to sampling over conical sections of the shell. Combined with the distributed source of a real hot spot, the inferred ρR from either the backscatter or forward-scatter measurement is found to be uniform over the sphere (although it may still be degraded with respect to 1-D), as seen in Fig. 1.

Next, consider the effect of the $\ell = 1$ mode. The strength of the mode is parametrized by the effective ion-temperature asymmetry $R_T = T_{\text{max}}/T_{\text{min}}$ it generates, and bin configurations belonging to similar R_T together to visualize the results. It is found that as the number of detectors used to infer an average ρR increases, the error in that inference decreases, although some detectors are more valuable than others (e.g., P10 backscatter is more valuable than P7 backscatter), as visualized in Fig. 2. This is due to the fixed positions of the diagnostics with respect to each other. With sufficient detectors, the error due to the mode 1 for high-performance–relevant implosions (i.e., $R_T \rightarrow 1$) approaches the acceptable limit of 5%.
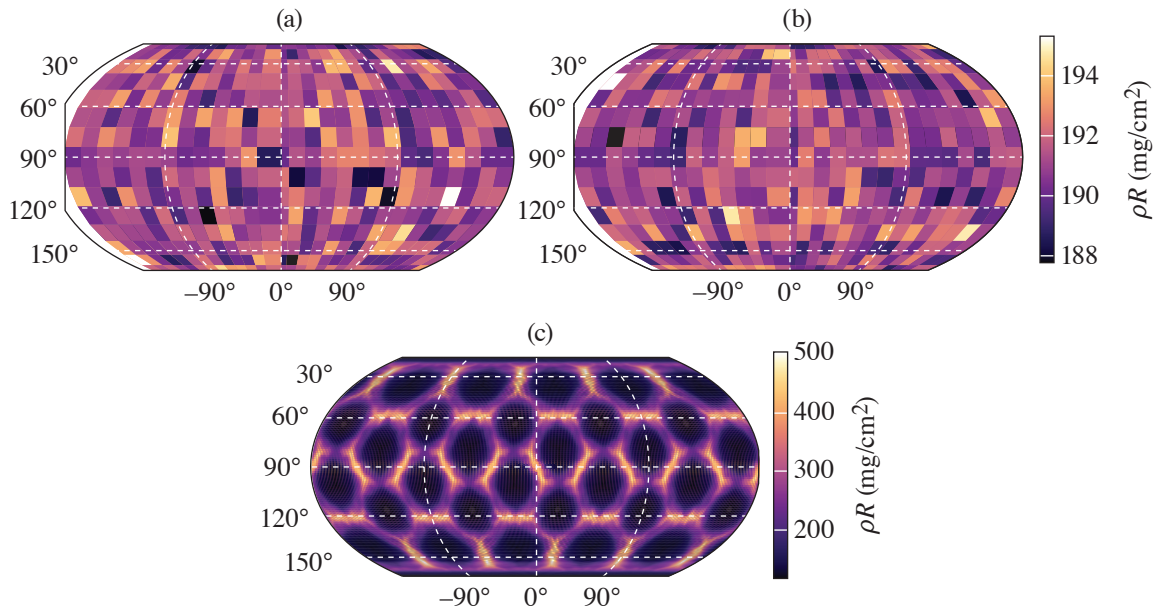
TC15973JR

Figure 1

A projection of (a) the inferred ρR from the backscatter edge, (b) the inferred ρR from the forward-scatter edge for a simulation, and (c) $\int \rho \, dr$ at bang time for a simulation with a target of radius 490 μm and a laser beam with radius 330 μm. Despite a rather large perturbation being driven, the effects of distributed source and integration over the edge result in no observable structured variation.
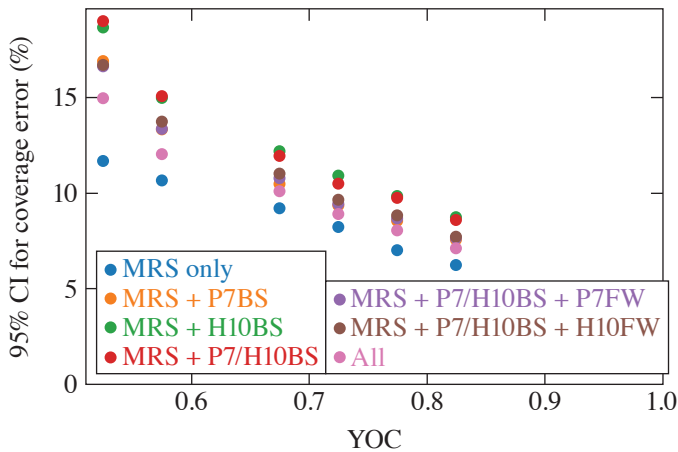
TC15977JR

Figure 2

The 2σ upper bound on the coverage error for each detector permutation for simulations with similar yield over clean (YOC), over a range of YOC's. Unlike with the $\ell = 1$ case, there is no observable parameterizing the degradation due to $\ell = 2$, and so the YOC is used directly. Unlike the $\ell = 1$ case, adding any one backscatter detector increases the error rather than decreasing it. Although the addition of the forward-scatter measurements on the nTOF's does decrease the error relative in the case where only backscatter nTOF measurements are considered, they nevertheless are not reduced below the level when only the MRS is considered. Since this is a result of the relative orientations of the nTOF and MRS detectors on OMEGA, this is a result specific to the OMEGA setup, and not a general observation. CI: confidence interval.

In the $\ell = 2$ mode case, the strength of the mode is parametrized by its yield degradation $\text{YOC} = Y_{3\text{-D}}/Y_{1\text{-D}}$, and bin the various configurations accordingly, as before. The results are visualized in Fig. 3. First, using only the MRS forward-scatter measurement results in a lower error than combining the MRS with any backscatter measurement. This counterintuitive result can be understood when the relative orientations of various integration regions are considered. In the $\ell = 1$ case considered above, the orientations meant that the H10 backscatter measurement was strongly anticorrelated with the MRS (since the ρR varied with an $\ell = 1$ pattern), while the P7 backscatter measurement was only weakly correlated with the MRS. Since the $\langle \rho R \rangle$ lies in between the maxima and minima, an average (by whatever mechanism) of measurements best reproduces the $\langle \rho R \rangle$ if some measurements are greater than $\langle \rho R \rangle$, and some are less. In the $\ell = 2$ case, H10 and P7 backscatter measurements are, due to their specific orientations on the
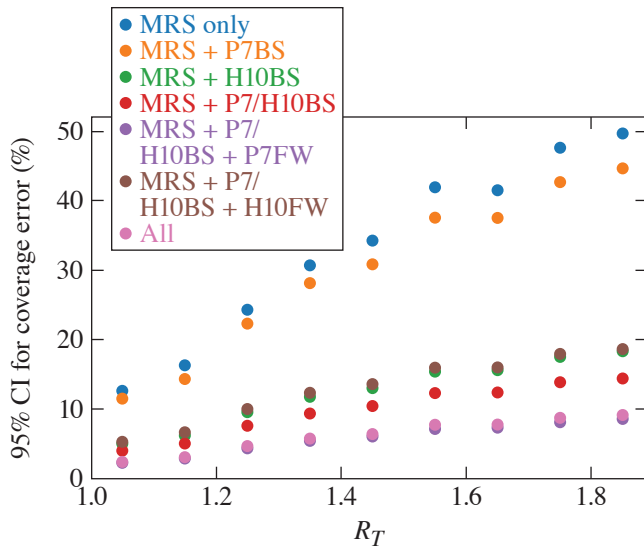
Figure 3
The 2σ upper bound on the coverage error for each detector permutation for all simulations with similar R_T over a range of R_T. First, note that having only the MRS (blue circles) has an extremely high error for even small values of R_T. Adding the P7 nTOF (orange circles) is not as valuable as adding the H10 nTOF (green circles) since the P7 backscatter and MRS forward-scatter regions are nearer to each other than the H10 backscatter and MRS forward scatter, and vice versa for the hypothetical P7 and H10 forward-scatter measurement. Nevertheless, adding all five detector configurations significantly reduces error from the currently used detector configuration.

TC15975JR

OMEGA system, well correlated with the MRS (H10 more so than P7). In addition, the backscatter measurements sample a much smaller region of the shell than the forward scatter and, thus, have a higher probability of measuring an extremely different ρR from the MRS (again, H10 more than P7). Therefore, when including them in an average, it is possible to move the average further away from the $\langle \rho R \rangle$, and thereby increase the composite error. From there, including additional forward-scatter measurements either from P7 or H10 detectors reduces the error since a larger region of the shell is sampled. However, it is insufficient to correct for the bias induced by the backscatter measurement.

Finally, having established a measure of the likely values of how the measured ρR deviates from $\langle \rho R \rangle$ that can be expected under reasonable conditions, one considers whether it is possible to recover $\langle \rho R \rangle$, even if only in restricted cases. Here, the only case considered will be where the $\ell = 1$ mode dominates. The reason for choosing only this case is that the $\ell = 1$ case is the only one where the yield degradation due to the mode can be inferred on OMEGA at this time. Defining $R_{\rho R} = \rho R / \langle \rho R \rangle$ as the deviation of the measured ρR at some line of sight from the true 4π average $\langle \rho R \rangle$, it is noted that since the orientation of the mode with respect to each detector is known and deterministic, it is reasonable to presume that there ought to be a relationship between the $R_{\rho R}$ at the detector location and both a measure of the mode amplitude and the central angle y between the mode maximum and detector position. The mode amplitude can be parametrized either by the R_T, or by the ratio of the bulk flow to the implosion velocity $\tilde{v}$. A suggested ansatz for $R_{\rho R}$ is given by

$$R_{\rho R} \cdot (R_T, \psi) = R_T \alpha + A(R_T - 1)\beta \cos(\psi - \psi_0), \tag{2}$$

$$R_{\rho R} \cdot (\tilde{v}, \psi) = \exp(\alpha \tilde{v}) + A\tilde{v}\beta \cos(\psi - \psi_0), \tag{3}$$

where A, α, β, and ψ_0 are constants that differ for forward and backward scatter and will be determined by fitting to the data, and are summarized in Table III. A graphic presentation the quality of the fits is shown in Fig. 4 and indicates that Eqs. (2) and (3) accurately represent the modulation of ρR over the sphere.

Using the coefficients in Table I, it is also possible to calculate a final "prediction" of the ρR that would be used in experiments, assuming only the existing OMEGA detectors are used. This is shown in Fig. 5, where the arithmetic average of the detector predictions using the coefficients in Table III is shown for each simulation in the $\ell = 1$ dataset. If such a reconstruction could be performed on OMEGA, the uncertainty from the $\ell = 1$ modes can be made sufficiently low (<3.5%) for incremental iterative schemes to be successful on OMEGA. This suggests that generating such procedures for $\ell = 2$ should be a high priority since these modes are known to exist on OMEGA.

Table III: Fit parameters of Eqs. (2) and (3) for the forward and backscatter detectors.

Detector	α	β	ψ	A
Forward scatter (R_T)	0.34	0.62	−0.21	0.65
Backscatter (R_T)	0.46	0.64	−0.24	−0.78
Forward scatter ($\tilde{v}$)	0.32	1.09	−0.24	1.07
Backscatter ($\tilde{v}$)	0.44	1.05	0.37	−1.22

TC15980JR
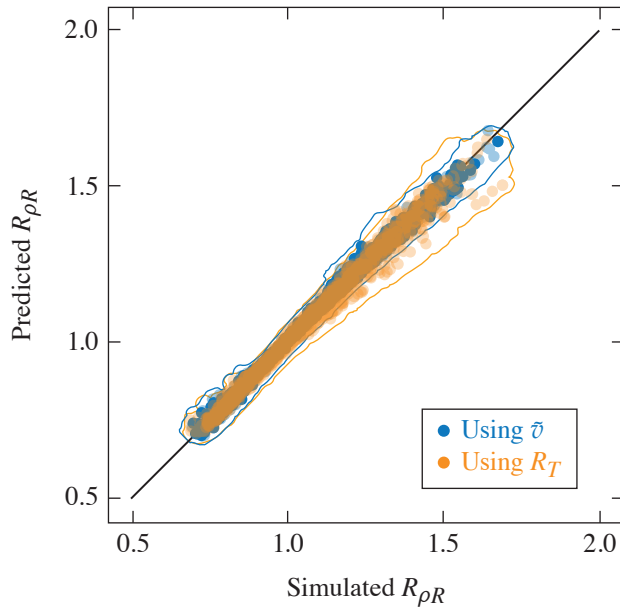
Figure 4
The accuracy of Eq. (2) (orange circles) and Eq. (3) (blue circles) in reconstructing the $R_{\rho R}$ across the entire dataset for each detector separately, assuming the orientation and amplitude of the $\ell = 1$ mode is known. Due to the large number of points in the full dataset, 10% are selected randomly and plotted. The solid line shows the extent of the full dataset for both cases. The $R_{\rho R}$ calculated from the simulations is on the horizontal axis, while the prediction from Eqs. (2) and (3) is on the vertical axis.

TC15981J1
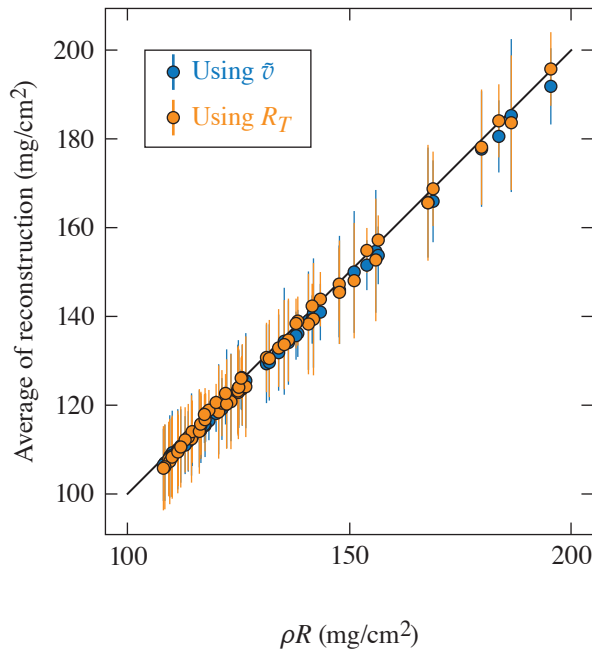
Figure 5
The accuracy of harmonically averaging the reconstructed ρR inferred using Eq. (2) (blue circles) and Eq. (3) (orange circles) in predicting $\langle \rho R \rangle$ for all simulations in the dataset using only the MRS and P7/H10 backscatter detectors, assuming the orientation and amplitude of the $\ell = 1$ mode is known. Error bars represent the 2σ range of the reconstruction when varying mode orientations with respect to fixed detector locations. The method is clearly accurate across the full range of conditions, with an rms error of roughly 3.5% for both the R_T and ($\tilde{v}$) models.

Accurate measurements of the ρR are integral to an accurate understanding of the performance of cryogenic direct-drive ICF experiments on OMEGA. Quantifying and rectifying the errors that are incurred by incomplete coverage are a necessary step toward achieving the accuracy necessary to design OMEGA experiments that will scale to hydrodynamically equivalent ignition. Quantifying this error is also a step toward a quantification of the total uncertainty in the 1-D–equivalent ρR that arises as a combination of coverage and measurement uncertainty. Considered here are the effects of limited detector coverage over a range of core conditions using *ASTER* simulations, post-processed with *IRIS* with varying $\ell = 1$ and 2 modes, for a number of permutations of existing and hypothetical detectors used on OMEGA. The expected uncertainty is quantified due to the induced asymmetry over the credible range of expected perturbations on OMEGA. It is then found that the error due to limited detector coverage tends to decrease as additional detectors are added in the $\ell = 1$ case, but find that due to the specific detector geometry on OMEGA, the $\ell = 2$ coverage uncertainty can increase as additional backscatter measurements are made. The coverage error due to the $\ell = 1$ mode is robustly eliminated if the existing nTOF detectors on OMEGA were capable of forward-scattering measurements. After postulating that the orientation and yield degradation caused by a mode could be used to reconstruct the 1-D–equivalent ρR, it is shown that this is indeed possible in cases that are dominated by large $\ell = 1$ modes, and that the error in reconstructing the true 1-D–equivalent ρR can be made acceptably low with existing OMEGA diagnostics.

1. J. D. Lawson, Proc. Phys. Soc. Lond. B **70**, 6 (1957).
2. R. Betti and O. A. Hurricane, Nat. Phys. **12**, 435 (2016).
3. A. R. Christopherson *et al.*, Phys. Plasmas **25**, 012703 (2018).
4. R. Betti *et al.*, Phys. Plasmas **17**, 058102 (2010).
5. P. Y. Chang *et al.*, Phys. Rev. Lett. **104**, 135002 (2010).
6. B. K. Spears *et al.*, Phys. Plasmas **19**, 056316 (2012).
7. R. Betti *et al.*, Phys. Rev. Lett. **114**, 255003 (2015).
8. C. D. Zhou and R. Betti, Phys. Plasmas **14**, 072703 (2007).
9. T. R. Boehly *et al.*, Opt. Commun. **133**, 495 (1997).
10. V. Gopalaswamy *et al.*, Nature **565**, 581 (2019).
11. A. Lees *et al.*, Phys. Rev. Lett. **127**, 105001 (2021).
12. V. Gopalaswamy *et al.*, Phys. Plasmas **28**, 122705 (2021).
13. I. V. Igumenshchev *et al.*, Phys. Plasmas **23**, 052702 (2016).
14. M. Gatu Johnson *et al.*, Rev. Sci. Instrum. **89**, 10I129 (2018).
15. C. J. Forrest *et al.*, Rev. Sci. Instrum. **83**, 10D919 (2012).

Diagnosing Magnetic Fields in Cylindrical Implosions with Oblique Proton Radiography

P. V. Heuer,[1] L. S. Leal,[1] J. R. Davies,[1] E. C. Hansen,[1] D. H. Barnak,[1] J. L. Peebles,[1] F. García-Rubio,[1] B. Pollock,[2] J. Moody,[2] A. Birkel,[3] and F. H. Séguin[3]

[1]Laboratory for Laser Energetics, University of Rochester
[2]Lawrence Livermore National Laboratory
[3]Plasma Science and Fusion Center, Massachusetts Institute of Technology

Cylindrical implosions can be used to amplify an applied axial magnetic field via flux compression, which can be used to study fundamental plasma physics in high magnetic fields[1] and is a key feature of the magnetized liner inertial fusion (MagLIF) energy scheme.[2] Previous experiments on the OMEGA Laser System have measured flux compression in cylindrical implosions using proton radiography.[3,4] These experiments were followed by the development of the laser-driven MagLIF platform,[5] which uses smaller-diameter cylindrical targets with a higher maximum convergence that reach maximum convergence more quickly. However, attempts to use proton radiography with this platform to measure the compressed axial magnetic field in the same manner as previous work have so far been unsuccessful, primarily due to the impact on the radiographs of other strong electric and magnetic fields near the target. This summary analyzes the results of two recent experiments that attempted to measure the compressed magnetic field in a cylindrical implosion using the laser-driven MagLIF platform and demonstrate how the measurement is obscured by the presence of self-generated magnetic fields.

Two experiments were conducted [hereinafter Exp. 1 and Exp. 2 using the setup shown in Fig. 1(a)]. In both experiments, the target is a plastic (CH) cylinder imploded using 40 beams (1.5-ns square-shaped pulse, total energy 16 kJ) with an overlapped intensity of 10^{14} W/cm^2. In Exp. 1 the target is gas filled (14 atm H$_2$), which is preheated by an axial beam prior to compression as in MagLIF. In Exp. 2 the cylinder interior is initially vacuum but soon fills with CH plasma when the shock driven by the compression beam breaks out into the interior. A set of external coils driven by MIFEDS (magneto-inertial fusion electrical discharge system)[6] provides an axial magnetic field (9 T in Exp. 1, 5 T in Exp. 2). An unmagnetized shot (with the coils in place but not energized) was taken in Exp. 1. Experiment 2 was identical except for the thickness of the cylinder and the addition of a foil to block some of the protons [visible in Fig. 1(d)].

Proton radiography[7] is used to diagnose the fields. A D^{3}He backlighter capsule 11 mm from the cylinder is imploded by 16 beams to produce 3-MeV and 15-MeV protons. The protons pass through the target cylinder walls with negligible scattering (verified on the unmagnetized shot) but are deflected by electric and magnetic fields in the vicinity of the target. The protons are then recorded on two CR-39 plates (shielded by 7.5 μm of tantalum and separated by 200 μm of aluminum to differentiate between the two proton energies) at a distance of 270 mm. In both experiments, the timing of the proton source is chosen to match the peak convergence of the implosion (which is also the peak of neutron production, or "bang time") at $t = 1.5\pm0.1$ ns. Due to the target chamber geometry, in both experiments the proton radiography axis is tilted relative to the target normal by an angle θ_T, making this "oblique" proton radiography.

To directly compare simulations to experimental results, synthetic proton radiographs are generated using an open-source particle-tracing algorithm that was developed for the PlasmaPy project as part of this work.[8] Three-dimensional simulations of the experiment, including the coronal plasma produced by the compression beams, were performed using the multiphysics
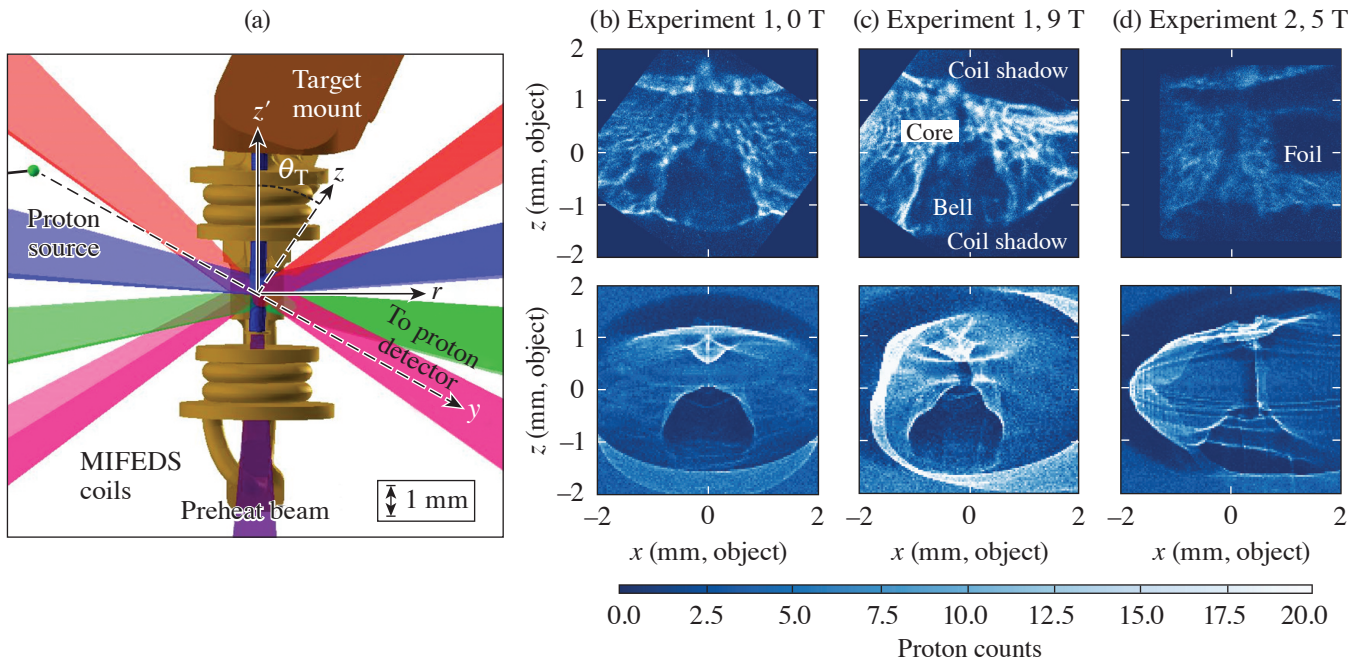
E30122JR

Figure 1
(a) A diagram of the setup for Exp. 1, with only a subset of the compression beams shown for clarity. (The setup for Exp. 2 is similar.) [(b)–(d)] Experimental proton radiographs (top row) for both experiments and the corresponding synthetic radiographs (bottom row) show good agreement.

radiation-hydrodynamic code *HYDRA*. A population of test protons was then traced through the simulated electric and magnetic fields and onto a detector to create synthetic radiographs. The resulting radiographs for Exp. 1 are shown in Figs. 1(b)–1(c) and Fig. 1(d) shows the radiograph for Exp. 2. All radiographs contain similar features. The "bell"-shaped feature is created by self-generated azimuthal magnetic fields in the coronal plasma produced by the drive beams, while the "core" feature visible on the magnetized radiographs is due to the compressed axial field. Small ripple features on the experimental data are not reproduced in the synthetic radiographs: this "small-scale structure" is likely due to kinetic effects such as instabilities or charge-separation fronts. Shadows are visible at the top and bottom of the experimental radiographs where protons are blocked by the MIFEDS coils.

Several approaches, including direct inversion algorithms, are applied to try and recover the line-integrated magnetic field from the experimental radiographs. However, while these techniques work reasonably well with the synthetic data, the loss of protons in the shadows of the MIFEDS fields and the presence of the small-scale structure prevent them from working with the experimental data. It is concluded that these experimental radiographs are consistent with the presence of a compressed axial field, but that a measurement of the compressed field is prevented by the self-generated azimuthal magnetic fields in the coronal plasma and the small-scale structure fields.

These results are compared to previous experiments on the OMEGA Laser System,[3,4] which successfully measured the compressed axial magnetic field in a similar cylindrical implosion. Comparing the design of this experiment to the current work provides guidance for the design of future work, suggesting that the radiography angle θ_T, target dimensions, laser pulse duration, and coil geometry are important parameters that determine the feasibility of this type of measurement. In many experiments, the ability to change these features is limited by other design considerations. However, future attempts to measure compressed axial magnetic fields in cylindrical implosions should include among these considerations the potential impact of self-generated fields on the measurement.

1. C. A. Walsh *et al.*, Plasma Phys. Control. Fusion **64**, 025007 (2022).

2. S. A. Slutz *et al.*, Phys. Plasmas **17**, 056303 (2010).

3. O. V. Gotchev *et al.*, Phys. Rev. Lett. **103**, 215004 (2009).

4. J. P. Knauer *et al.*, Phys. Plasmas **17**, 056318 (2010).

5. J. R. Davies *et al.*, Phys. Plasmas **24**, 062701 (2017).

6. G. Fiksel *et al.*, Rev. Sci. Instrum. **86**, 016105 (2015).

7. N. L. Kugland *et al.*, Rev. Sci. Instrum. **83**, 101301 (2012).

8. PlasmaPy Community *et al.*, PlasmaPy (Version 0.8.1), Zenodo, Accessed 14 September 2022, https://doi.org/10.5281/zenodo.6774350.

The Effect of Laser Preheat in Magnetized Liner Inertial Fusion at the Omega Laser Facility

L. S. Leal,[1,2] A. V. Maximov,[1,3] E. C. Hansen,[1,2] J. R. Davies,[1] D. H. Barnak,[1] J. L. Peebles,[1] K. M. Woo,[1] P. V. Heuer,[1] A. B. Sefkow,[1,2,3] and R. Betti[1,2,3]

[1]Laboratory for Laser Energetics, University of Rochester
[2]Department of Physics and Astronomy, University of Rochester
[3]Department of Mechanical Engineering, University of Rochester

An important effect in magnetized transport is represented by the Nernst term in Ohm's law that advects magnetic fields down electron temperature gradients.[1–3] This term has been shown to be dominant over the fluid motion in plasmas below the critical density of the preheating laser. It is also possible that magnetic-flux transport in the hot spot is dominated by Nernst advection.[4] The preheat laser can also lead to material from the window or wall of the targets mixing with the fuel region.[5] This summary is focused on modeling the effect of preheat on the dynamics of the fuel in magnetic liner inertial fusion (MagLIF) experiments and the importance of certain terms in the magnetohydrodynamics model, specifically the Nernst effect, as well as the effect of wall material being mixed with the fuel within the capsule. Three-dimensional simulations are used to characterize the effects on yield and implosion characteristics when varying the preheat laser energy.

Three-dimensional radiation-hydrodynamic simulations show there is an optimal laser preheat energy for laser-driven MagLIF on OMEGA, with a 27-T initial magnetic field, resulting in a peak in neutron yield. A similar peak in neutron yield as a function of laser preheat energy was observed in experiments; however, the experimental yield and the optimal laser preheat energy were lower than predicted in simulations. By comparing simulations that do or do not include the Nernst effect, it was found that the Nernst effect is necessary to properly model how laser preheat affects the field dynamics in the fuel region of MagLIF. The drop from the peak in neutron yield with increasing laser preheat energy past the optimal value is larger with the Nernst effect. It is noted that with increasing preheat laser energy, there is less magnetic-field enhancement due to compression and the radial profile of the density becomes less dominated by edge effects.

A 2-D slice of the magnetic field was normalized to the initial seed magnetic field with and without Nernst effect at bang time where the fuel region is outlined. In the case without the Nernst effect, the magnetic field peaks at the radial edge of the fuel region in the center of the z axis. The magnetic field at the edges is convected with the blast wave during the preheat stage, remains at the edge throughout the implosion, and experiences flux compression. In Fig. 1(a) where the simulation includes the Nernst effect, flux compression occurs at the overdriven ends; however, the magnetic field at the center of the z axis has largely been advected out of the fuel region.

Simulations using a mix model show that including mix in implosions leads to yield degradation and can also shift the optimal laser preheat energy to a lower value. The use of premixed region limits the simulation's ability to exactly match the material penetrations occurring in experiments, but gives some insight to the effects of mix. Unlike MagLIF at Sandia National Laboratories, the primary-yield degradation mechanism from mix in MagLIF on OMEGA is not only from radiative losses (since neutron-averaged ion temperatures are not consistently lower between clean simulation and simulations with mix). The added mass from mix lowers the convergence ratios and the Hall parameter across the capsule fuel region, modifying plasma transport coefficients. Simulations also suggest that higher seed magnetic fields available from upcoming generations of MIFEDS (magneto-inertial fusion electrical discharge system) will further enhance yield in D–D cylindrical implosions. A future expanded study
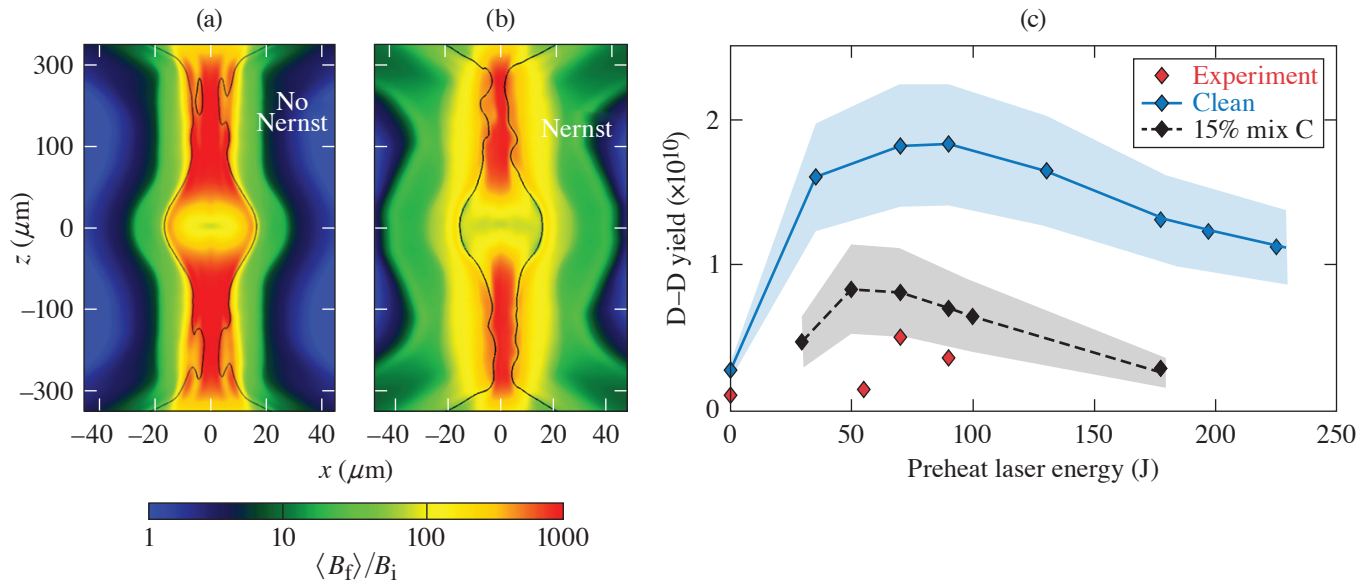
TC15789JR

Figure 1

Two-dimensional slice of log scale magnetic-field enhancement (magnetic field over the initial seed field) at bang time for 90-J preheat laser energy and 27-T seed magnetic field from simulations (a) without the Nernst effect and (b) with the Nernst effect where the fuel region is outlined in black. (c) D–D neutron yield over varying preheat laser energies from experiments (red), clean simulations (blue), and simulations mixed with 15% C in the fuel region (black) with 27-T seed field including the Nernst effect.

of the mix effect will be needed to ascertain the degree to which mix products may penetrate the core, as well as its behavior at different preheat laser energies. Simulations can then attempt to model mix nonuniformly to study the impact on transport in the fuel region. As simulations with the mix model see a large drop in yield, they can lead to estimates on when yield degradation from increasing preheat laser energy could impact future experiments.

1. S. I. Braginskii, Sov. Phys. JETP **6**, 358 (1958).
2. E. M. Epperlein and M. G. Haines, Phys. Fluids **29**, 1029 (1986).
3. D. H. Froula *et al.*, Phys. Rev. Lett. **108**, 125003 (2012).
4. A. L. Velikovich, J. L. Giuliani, and S. T. Zalesak, Phys. Plasmas **26**, 112702 (2019).
5. A. J. Harvey-Thompson *et al.*, Phys. Plasmas **25**, 112705 (2018).

Analysis of Core Asymmetries in Inertial Confinement Fusion Implosions Using Three-Dimensional Hot-Spot Reconstruction

K. M. Woo,[1] R. Betti,[1] C. A. Thomas,[1] C. Stoeckl,[1] K. Churnetski,[1] C. J. Forrest,[1] Z. L. Mohamed,[1] B. Zirps,[2]
S. P. Regan,[1] T. J. B. Collins,[1] W. Theobald,[1] R. C. Shah,[1] O. M. Mannion,[1] D. Patel,[1] D. Cao,[1] J. P. Knauer,[1]
V. Yu. Glebov,[1] V. N. Goncharov,[1] P. B. Radha,[1] H. G. Rinderknecht,[1] R. Epstein,[1] V. Gopalaswamy,[1] F. J. Marshall,[1]
S. T. Ivancic,[1] and E. M. Campbell[1]

[1]Laboratory for Laser Energetics, University of Rochester
[2]Department of Mechanical Engineering, University of Rochester

Three-dimensional effects play a crucial role during the hot-spot formation in inertial confinement fusion implosions. To characterize effects of low modes on hot-spot formations, a data-analysis technique for 3-D hot-spot reconstruction from experimental observables was developed. In summary, the effective flow direction, governed by the maximum eigenvalue in the velocity variance of apparent ion temperatures, was found to agree with the measured hot-spot flows for implosions dominated by mode $\ell = 1$. Asymmetries in areal-density (ρR) measurements were found to be characterized by a unique cosine variation along the hot-spot flow axis. A 3-D hot-spot x-ray emission tomography method was developed to reconstruct the 3-D hot-spot plasma emissivity using a generalized spherical-harmonic Gaussian function. The mapping between the projections from the 3-D hot-spot emission model and the measured x-ray images along multiple views is obtained by a gradient descent optimization algorithm.

Spherically symmetric flows,[1,2] turbulences,[3] and 3-D flows[4] are sources of velocity variances in neutron velocity spectra. Non-stagnating hot-spot flows kinematically boost the velocity of neutrons, produced from deuterium (D) and tritium (T) nuclear fusion reactions. The hot-spot residual fluid motion modifies the neutron velocity distribution so that the width of a neutron velocity spectrum is broadened according to a unique function of the velocity variance $\sigma = \mathrm{var}\,[v_{\mathrm{flow}} \cdot d_{\mathrm{LOS}}]$, where v_{flow} is the hot-spot flow velocity measured in the laboratory frame and d_{LOS} is the line of sight (LOS) unit vector, pointing from the target chamber center to the position of a detector. The velocity variance is a measurement for the hot-spot flow residual kinetic energy (RKE) since it measures the square of hot-spot flow velocity fluctuations. It contains six independent components $\sigma_{ij} = \langle\langle(v_i - \bar{v}_i) \cdot (v_j - \bar{v}_j)\rangle\rangle$, including three directional variances with $i = j$ and three covariances with $i \neq j$. Indices i and j go from 1 to 3, representing x, y, and z Cartesian coordinates, respectively. Since covariances are unchanged upon exchanging i and j indices, the velocity variance matrix is Hermitian. This implies that σ is diagonalizable with real eigenvalues λ_i, which are the components of the hot-spot RKE along three orthonormal eigenvector directions e_i. This behavior is consistent with the fact that the trace of σ, the total hot-spot residual kinetic energy, is invariant under the special orthogonal SO(3) transformation in the 3-D Euclidean space. Hence, an apparent ion temperature measured at a given LOS is related to the hot-spot RKE's along the three eigenvector directions through the SO(3) transformation

$$T_{\mathrm{LOS}} = T_{\mathrm{thermal}} + M_{\mathrm{DT}} \sum_{i=1}^{3} \lambda_i \langle d_{\mathrm{LOS}} \,|\, e_i \rangle^2, \tag{1}$$

where T_{thermal} is the ion thermal temperature in the center of mass frame of D–T nuclear reactions, and the bracket notation represents the inner product between the LOS unit vector and the ith eigenvector. Equation (1) is a generalized result to explain variations in apparent ion temperatures nonrelativistically. When implosions are dominated by mode 1, Eq. (1) implies a cosine-square variation along the eigenvector direction with the maximum eigenvalue, i.e., the hot-spot RKE of the jet. The extrapolation

for the cosine-square variation in OMEGA ion-temperature measurements using Eq. (1) is illustrated in Fig. 1(a). When implosions contain mode 2, the difference between eigenvalues parallel $\lambda_\parallel$ and perpendicular $\lambda_\perp$ to the rotational axis implies a nonvanishing ion-temperature asymmetry. Even the measured hot-spot flow velocity is zero since symmetric mode-2 hot-spot flows do not change the first moment of neutron velocity spectra. This phenomenon is illustrated by Fig. 1(b). A good agreement between the trend of experimental data and *DEC3D* simulations with a uniform 2% initial velocity perturbation of mode 2 on varying mode-1 perturbations is obtained. A semi-analytic model is derived to explain the mode-1 ρR degradation. Both 4π averaged and variations in ρR are found to be a function of the ion-temperature ratio $R_T = T_{\max}/T_{\min}$,

$$
\frac{(\rho R)\text{LOS}}{(\rho R)\text{1-D}} = R_T^\alpha + \sqrt{R_T^{2\alpha} - R_T^{2\beta}} \cos\theta_{\text{LOS-flow}},
\tag{2}
$$

where $\alpha = -0.3$ and $\beta = -0.47$ are parameters obtained from *DEC3D* mode-1 simulations, and $\theta_{\text{LOS-flow}}$ is the inclination angle between the LOS and the measured hot-spot flow vectors. The extrapolation for the mode-1 angular-dependence in areal density measurements is illustrated by Fig. 1(c). The 3-D kernel as stated by Eq. (2) is shown to accurately fit the H10 ρR measurements. A 3-D x-ray emission tomography method was devised to reconstruct arbitrary hot-spot shapes using a generalized spherical harmonic Gaussian function,
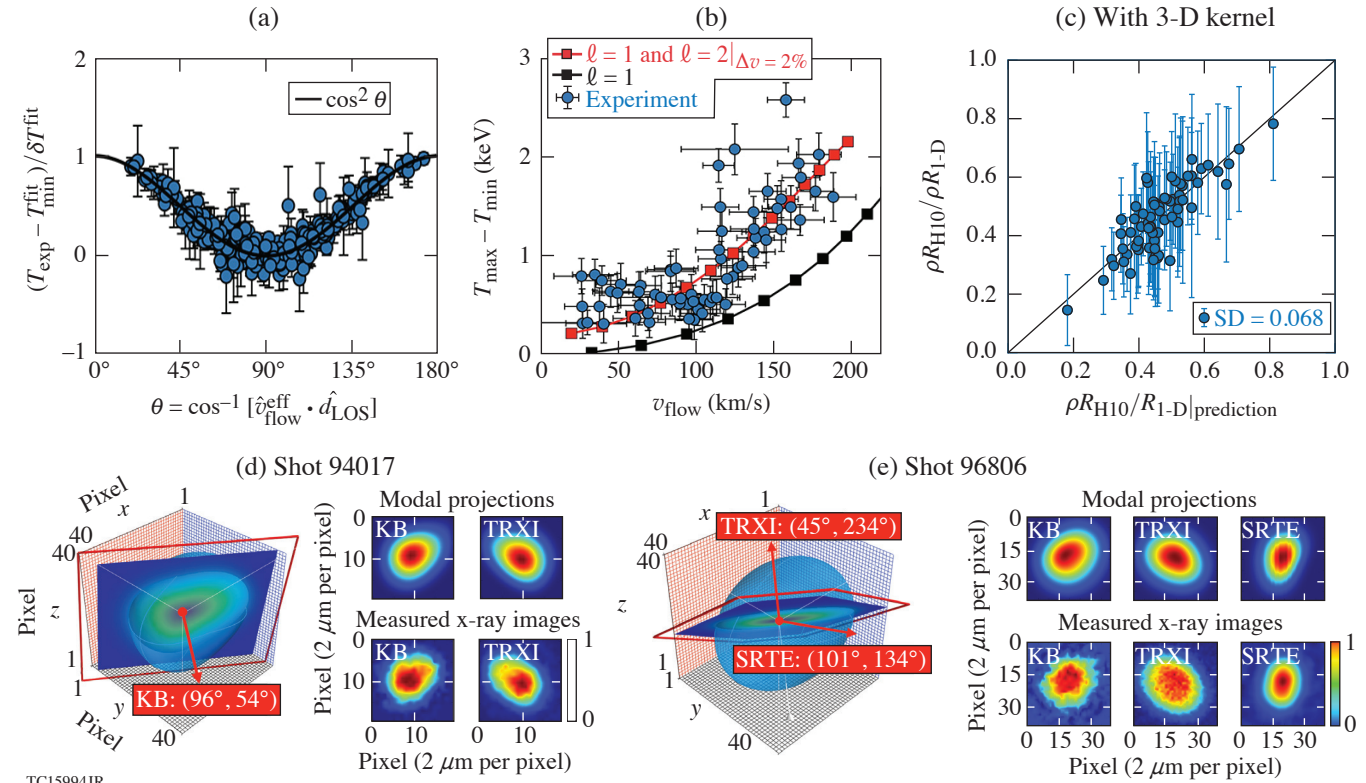
Figure 1

Analysis of core asymmetries in OMEGA implosion experiments. (a) The extrapolation for the cosine-square variation in ion-temperature measurements using Eq. (1). (b) The reconstruction for the trend of T_i and flow relation using *DEC3D* simulations. (c) The extrapolation for the mode-1 angular-dependence in areal density measurements using the 3-D kernel in Eq. (2). [(d),(e)] Three-dimensional hot-spot reconstructions for shots 94017 and 96806 using the generalized spherical-harmonic Gaussian model in Eq. (3). SD: standard deviation; KB: Kirkpatrick–Baez; TRXI: time-resolved x-ray imager; SRTE: spatially resolved x-ray imager.

$$\ln \varepsilon_v = \sum_{n=0}^{\infty} \sigma_n R^n \left[1 + \sum_{\ell=1}^{\infty} \sum_{m=-\ell}^{\ell} \sum_{k=0}^{\infty} A_{\ell m k} R^k Y_{\ell m}(\theta, \phi) \right]^n. \tag{3}$$

Expansion coefficients in Eq. (3) are determined by minimizing the root-mean-square deviations between modal projections and measured x-ray images measured at multiple views using the gradient descent optimization algorithm. Three-dimensional hot-spot reconstructions are illustrated in Fig. 1(d) and 1(e). The mode-1 skew signature and the mode-2 ellipticity are well reconstructed for shots 94017 and 96806, respectively.

1. R. E. Chrien, K. A. Klare and T. J. Murphy Rev. Sci. Instrum. **68**, 607 (1997).
2. T. J. Murphy, R. E. Chrien and K. A. Klare Rev. Sci. Instrum. **68**, 614 (1997).
3. T. J. Murphy, Phys. Plasmas **21**, 072701 (2014).
4. K. M. Woo *et al.*, Phys. Plasmas **25**, 102710 (2018).

Evaluation of Direct Inversion of Proton Radiographs in the Context of Cylindrical Implosions

J. R. Davies and P. V. Heuer

Laboratory for Laser Energetics, University of Rochester

Proton radiography is frequently used on OMEGA and OMEGA EP to infer electric and magnetic fields. If proton energy loss and scattering are negligible, proton deflection at the detector will be determined by the path-integrated transverse Lorentz force experienced by the protons. The most common technique used to infer fields from intensity modulations on the detector has been proton tracing in given fields, either assumed or obtained from simulations. Recently, a number of authors have used direct inversion to infer the fields,[1–6] and many of these direct inversion routines are publicly available on GitHub.[1–5] Direct inversion provides a solution independent of biases; particle tracing in specified forces is subject to user biases, and tracing in forces determined from simulations is limited by knowledge of the experimental conditions to be simulated and the physics included in the simulations. Publicly available direct inversion routines were applied to proton radiography data from cylindrical implosion experiments on OMEGA. As a first step, a series of test problems is generated using proton tracing to evaluate the routines.[7] These test problems are publicly available[8] as hdf5 files in pradformat.[9] The test results are summarized here.

Direct inversion determines deflections at the detector that map the source intensity (I_0) to the measured intensity (I). There is no unique solution to this problem, as demonstrated by the trivial case of simply swapping two particles on the detector. There is a unique solution, however, that minimizes total deflection and does not allow particles to be moved over one another. If proton trajectories to the detector do not cross, direct inversion will give the solution. If proton trajectories do cross, direct inversion will give one out of an infinite family of solutions, which is still useful information. In mathematics, direct inversion is known as the optimal transport problem, first described in a paper by Monge published in 1781 (Ref. 10), which derives what is now known as the Monge–Ampère equation. All but one of the publicly available direct inversion routines solve the Monge–Ampère equation.[1–4] The other routine[5] uses iterative methods to construct power diagrams (weighted Voronoi diagrams) of the source and measured intensities with equal flux in each cell, determining the deflections from the movement of cell centroids. Direct inversion can be applied to radiography with any charged particle, and to shadowgraphy where photons are deflected by gradients in refractive index.[5] In order to relate the deflections obtained at the detector to the forces in the object, one must assume a small angle deflection in the object (≪1 rad or 57.3°) so that the deflections are proportional to the line-integrated force along the original trajectory. In practice, this is not a major restriction since the proton radiography and shadowgraphy setups used on OMEGA and OMEGA EP subtend a small angle at the target. If there are regions where large angle deflections occur, information on the forces in these regions will be lost.

Test radiographs or, equivalently, shadowgraphs, were generated by particle tracing through purely radial force profiles in cylinders and spheres for a range of force amplitudes with uniform source intensities. In cylinders a Gaussian potential [$F_r \propto r \exp(-r^2/R_2)$], a linear profile ($F_r \propto r$ for $r \le R$)], and a top-hat profile (F_r = constant for $r \le R$) were used. The linear profile was chosen to represent the electric field in an isothermal, cylindrical expansion,[11] ignoring the rapidly decaying field in the electron sheath beyond the ion front. The top-hat profile was chosen to represent the axial magnetic field in a cylindrical implosion, which is discontinuous at the inner surface of the shell. For spheres, a Gaussian potential was used. Force is expressed as a dimensionless parameter

$$\mu = \frac{2LF}{Mpv},$$

where L is object-to-detector distance, M is magnification, F is Lorentz force, p is particle momentum, and v is particle velocity, or

$$\mu = \frac{L}{M} \frac{\mathrm{d}(n_\mathrm{e}/n_\mathrm{c})/\mathrm{d}r}{\sqrt{1-n_\mathrm{e}/n_\mathrm{c}}}$$

for shadowgraphy, where n_e is electron density and n_c is the critical density of the probe. All distances are expressed in terms of the object size R. Trajectories cross in all cases for the linear and top-hat profiles and for both cylindrical and spherical Gaussian potentials when $\mu_\mathrm{max} \geq 1.08$ or $\mu_\mathrm{max} \leq -0.484$, negative values indicating a focusing force.

Five direct inversion routines were found on GitHub.[1–5] Two of the routines, both Monge–Ampère solvers, did not run.[1,2] The other two Monge–Ampère solvers were found to be essentially identical, which is not surprising considering they are implementations of the same algorithm by the same author.[3,4] Therefore, one Monge-Ampère routine and one power-diagram routine[5] was available to evaluate. The Monge–Ampère routine could not solve the cylindrical problems because it uses fixed deflection potential boundary conditions, which would also cause issues with any problem that has modulations near the boundary. The correct boundary conditions to obtain a minimum deflection from the Monge–Ampère equation are to set the deflections across the boundaries to zero.[2] The Monge-Ampère routine accurately inverted the spherical Gaussian tests when trajectories did not cross and did so roughly 1000× faster than the power-diagram routine, but failed when trajectories crossed. The failure was obvious from the poor reproduction of the measured intensity. The failure appears to be caused by the adaptive time step, which rapidly falls to the specified minimum value for tests where deflected trajectories cross. The power-diagram routine successfully inverted all but two of the test problems. The power diagram failed for the top-hat profile with $\mu_\mathrm{max} = 2$ and a smaller bin width (0.015R) than the final value we settled on (0.025R); however, for the coarser bin width an adequate solution was obtained. The power-diagram routine failed for a spherical Gaussian with $\mu_\mathrm{max} = -0.5$ and the issue was not resolved by coarser binning, the bin width of 0.052R already being too coarse to resolve the sharp peak. The power-diagram routine moves the sites closest to the corners into the corners in order to interpolate the deflections to all points on the original grid, which, for this strongly focusing test, leads to significant distortion of the entire region. Examples of the line-integrated forces obtained by the power-diagram routine for the cylindrical tests are given in Fig. 1. In all cases the measured intensity was accurately reproduced. The inversion underestimates the original line-integrated forces when trajectories cross because it gives a minimum deflection solution. It should be remembered that when trajectories cross, there exists an infinite family of solutions for the line-integrated force. As a result of these tests, only the power-diagram routine was used to analyze the proton radiographs of cylindrical implosions.[12]

1. C. Graziani *et al.*, Rev. Sci. Instrum. **88**, 123507 (2017).

2. A. F. A. Bott *et al.*, J. Plasma Phys. **83**, 905830614 (2017); PROBLEM Solver (PROton-imaged B-field nonLinear Extraction Module), Accessed 12 July 2021, https://github.com/flash-center/PROBLEM.

3. M. F. Kasim, Invert Shadowgraphy and Proton Radiography, Accessed 8 July 2021, https://github.com/mfkasim1/invert-shadowgraphy.

4. M. F. Kasim *et al.*, Phys. Rev. E **100**, 033208 (2019); M. F. Kasim, PRNS (Proton Radiography with No Source), Accessed 12 July 2021, https://github.com/OxfordHED/proton-radiography-no-source.

5. M. F. Kasim *et al.*, Phys. Rev. E **95**, 023306 (2017); M. F. Kasim, Invert Shadowgraphy and Proton Radiography, Accessed 8 July 2021, https://github.com/mfkasim1/invert-shadowgraphy.

6. N. F. Y. Chen *et al.*, Phys. Rev. E **95**, 043305 (2017).

7. J. R. Davies and P. V. Heuer, "Evaluation of Direct Inversion of Proton Radiographs in the Context of Cylindrical Implosions," Physics Archive: https://doi.org/10.48550/arXiv.2203.00495 (2022).

8. J. Davies and P. Heuer, Synthetic Proton Radiographs for Testing Direct Inversion Algorithms, Zenodo, Accessed 3 August 2022, https://doi.org/10.5281/zenodo.6632986.

E29654JR
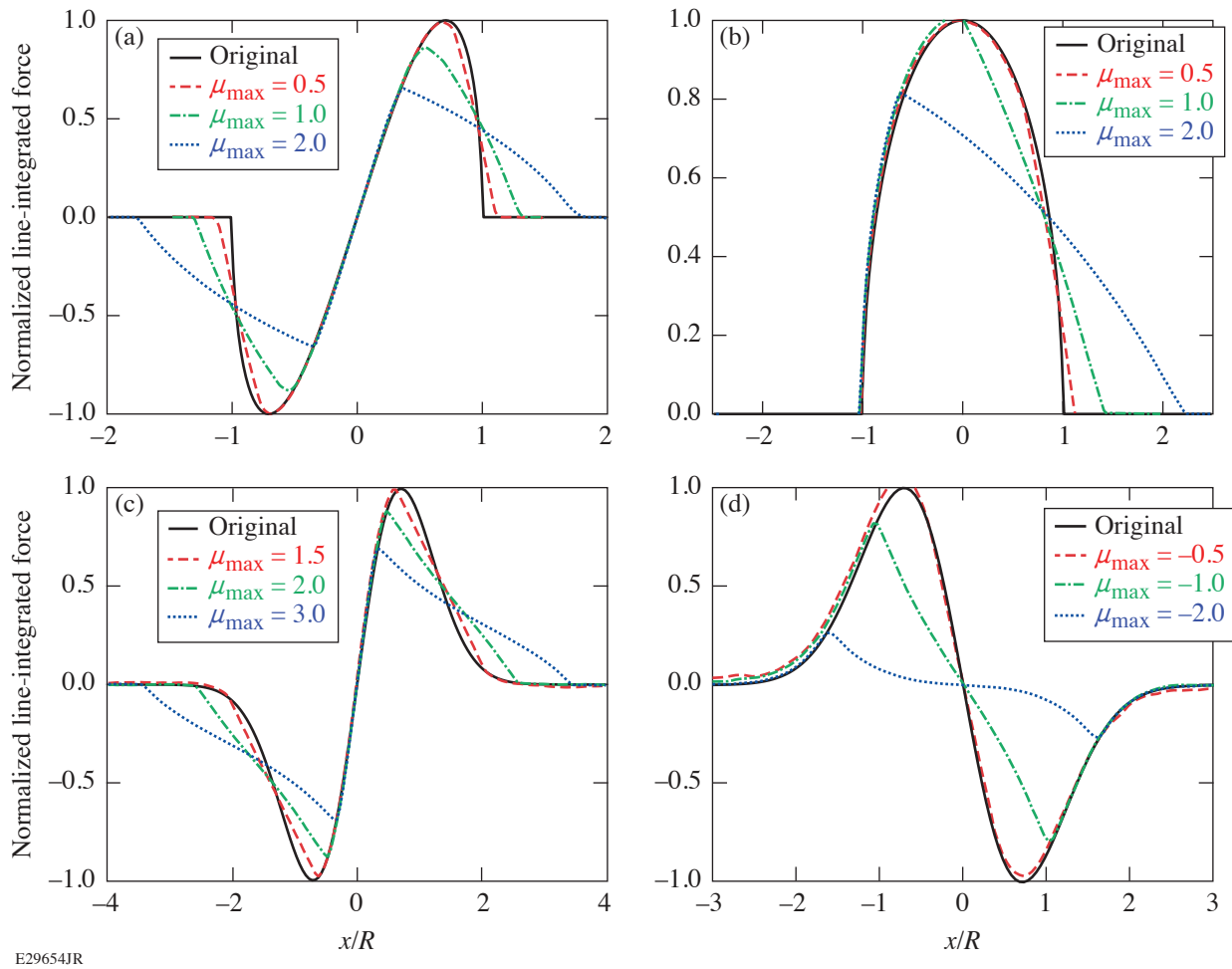
Figure 1
Line-integrated forces from the power-diagram routine for cylindrical test problems from (a) the linear profile, (b) the top-hat profile, and [(c),(d)] the Gaussian potential, normalized so that the maximum of the original is 1.

9. Pradformat (Proton Radiography File Format Tools), Accessed 12 July 2021, https://github.com/phyzicist/pradformat.

10. G. Monge, Mém. de l'Ac. R. des. Sc. An., 666 (1781).

11. M. Murakami and M. M. Basko, Phys. Plasmas **13**, 012105 (2006).

12. P. V. Heuer *et al.*, Phys. Plasmas **29**, 072708 (2022).

Particle-in-Cell Modeling of Plasma-Jet Merging in the Large-Hall-Parameter Regime

H. Wen,[1] C. Ren,[2,3] E. C. Hansen,[2] D. Michta,[2] Y. Zhang,[3] S. Langendorf,[4] and P. Tzeferacos[1,2]

[1]Laboratory for Laser Energetics, University of Rochester
[2]Department of Mechanical Engineering, University of Rochester
[3]Department of Physics and Astronomy, University of Rochester
[4]Physics Division, Los Alamos National Laboratory

Plasma-jet–driven magneto-inertial fusion (PJMIF) offers a novel "reactor-friendly" alternative approach to fusion energy that assembles targets by launching magnetized plasma jets from plasma guns at large standoff distances.[1] Fusion reactions take place in an all-gas/plasma architecture, avoiding repetitive hardware destruction. Furthermore, magnetic fields in the assembled target reduce thermal conduction and facilitate ignition. Most of the previous studies on this concept focused on the hydrodynamics,[2–5] while possible kinetic physics,[6] especially in target formation and compression, have not been well explored. Presented here are particle-in-cell (PIC) simulations with the code *OSIRIS* of two colliding counter-propagating magnetized jets to study the kinetic physics in the target formation process. The *OSIRIS* simulation results show that the fuel plasma jets can be stopped due to a microinstability—the modified two-stream instability (MTSI)[7,8]—rather than coulomb collisions. A comparison of 2-D simulations with *OSIRIS* and the single-fluid magnetohydrodynamic code *FLASH* shows that the codes predict similar macroscopic behaviors of the jets stopping and their subsequent expansion, despite the lack of kinetic physics in the *FLASH* simulations. The results provide validation for using *FLASH* to model target formation and beyond for plasma liner experiments (PLX's).

The total ion v_x– x phase space and the spectrum of the longitudinal electric field E_x are shown in Fig. 1 to illustrate the two dominant MTSI modes identified in the simulation. One of the MTSI modes corresponded to the interaction between the incoming ions and the interpenetrated ions from the counter-propagating jet. This MTSI mode is localized in region 1 [locations between the two solid black vertical lines in the ion phase space as shown in Figs. 1(a)–1(c)]. The incoming and interpenetrating jets can be easily identified since the distribution within region 1 has two distinct peaks on the v_x axis. Using the parameters obtained in region 1, we found that the MTSI growth rate was $\gamma_{MTSI} = 0.1$ ns^{-1} for the fastest growing mode at $k = 0.65\omega_{pe}/c$, where ω_{pe} is the local plasma frequency and c is the speed of light. The MTSI mode in region 1 initiated a shock that propagated to the left. A localized electrostatic field started to build up across the shock front as the MTSI grew. The interpenetrated ions were accelerated by this field to a longitudinal velocity of about 240 km/s (the sum of the plasma jet velocity and the shock velocity) and sustained that velocity afterward, as illustrated by the phase space features in region 1 in Figs. 1(b) and 1(c). The fastest-growing modes evaluated using parameters obtained from region 1 at different times are overlaid as the black solid line in Fig. 1(d), which agrees reasonably well with the dominant MTSI mode (the bright feature started around $k = 0.7\omega_{pe}/c$ at $t \approx 70$ ns), including the shift to lower k at a later time. The other MTSI mode (first appeared around $t \approx 85$ ns with $k = 1.2\omega_{pe}/c$) in Fig. 1(d) corresponded to the interaction between the incoming ions and the reflected ions. This MTSI mode was localized in region 2, locations between the two dashed vertical lines in Figs. 1(b) and 1(c), which tracked the shock-front propagation. Figure 1(d) plots the fastest-growing MTSI mode as a dashed black line that agreed well with the bright feature to the right of the initial MTSI mode corresponding to region 1. As evident in Fig. 1(d), this MTSI mode occurred later than the initial MTSI mode because the shock was generated by the initial MTSI mode. The wave number k_x of these two MTSI modes both shifted to smaller values over time, mainly due to the decreasing density and magnetic field in regions 1 and 2.
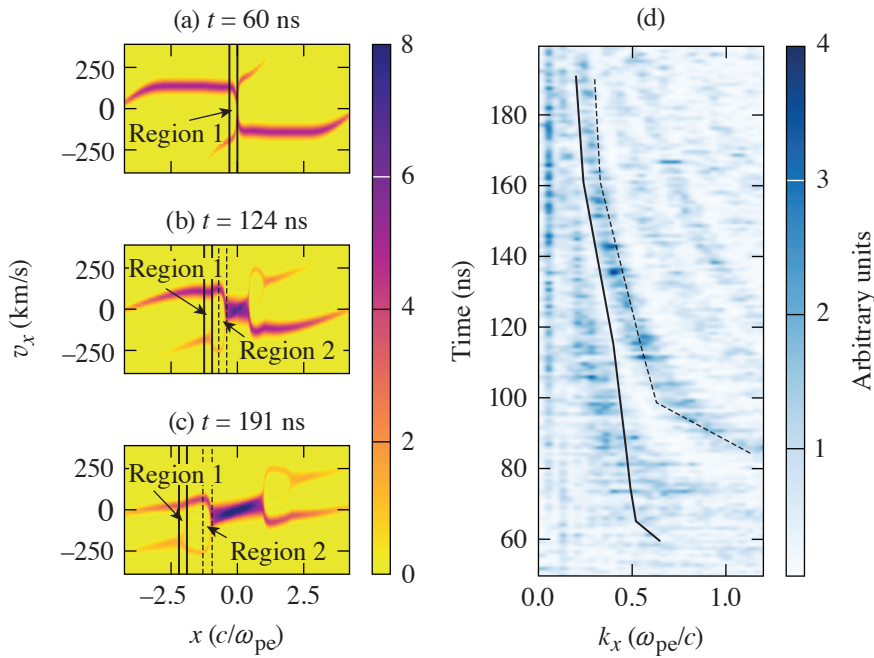
Figure 1

Ion v_x–x phase space at (a) $t = 60$ ns, (b) $t = 124$ ns, and (c) $t = 191$ ns; (d) the spectrum of longitudinal electric field E_x. The solid and dashed black lines in the plot (d) correspond to the fastest-growing MTSI modes with parameters obtained from the regions 1 and 2 [plots (a)–(c)], respectively.

TC16003JR

Figure 2 shows the time evolution of the plasma β, the electron Hall parameter χ_e, and the ion Hall parameter χ_i in the central merging region obtained from *OSIRIS* and *FLASH* simulations. The dimensionless parameters predicted by the two codes were on the same order of magnitude. During the jet-merging process and before the merged plasma expansion, i.e., between 50 and 200 ns, χ_e, and χ_i were greater than unity; the plasma β was close to unity. This is the desired characteristic of planned PLX. The same level of agreement between the two codes was achieved for the electron and ion Hall parameters. The plasma β differed more in the antiparallel-B case: β in *OSIRIS* was consistently larger than in *FLASH*. This is likely due to the interpenetrated species carrying magnetic fields to the other jet, leading to the enhanced magnetic-field cancellation.

Figure 2

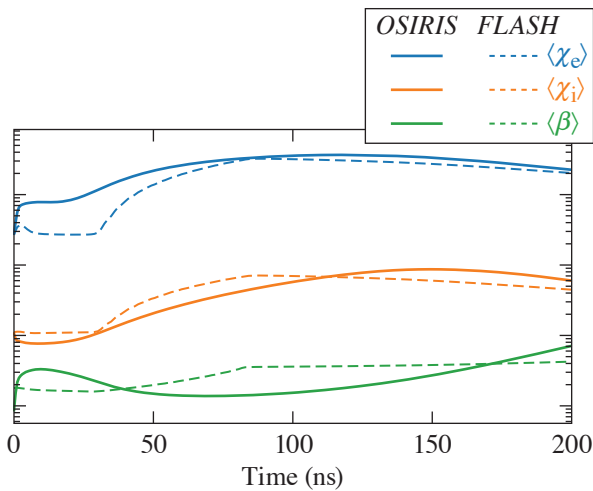The dimensionless parameters near the merging region obtained in *OSIRIS* (solid lines) and *FLASH* (dashed lines) simulations of a 5-eV plasma jet collision: electron Hall parameter $\langle \chi_e \rangle$ parameter (blue lines), ion Hall parameter $\langle \chi_i \rangle$ (orange lines), and plasma $\langle \beta \rangle$ (green lines). The angle bracket corresponds to spatial average.

TC16011JR

In summary, the MTSI is identified to be the main mechanism responsible for stopping the plasma jets and preventing species interpenetration. The 2-D PIC simulations validate the results of the radiation magneto-hydrodynamics code *FLASH*, which will be the primary tool for modeling various stages of future PJMIF experiments.

1. S. C. Hsu and S. J. Langendorf, J. Fusion Energy **38**, 182 (2019).
2. J. S. Davis *et al.*, Phys. Plasmas **19**, 102701 (2012).
3. J. T. Cassibry, M. Stanic, and S. C. Hsu, Phys. Plasmas **20**, 032706 (2013).
4. W. Shih *et al.*, Phys. Plasmas **26**, 032704 (2019).
5. K. Schillo and J. Cassibry, Phys. Plasmas **27**, 042707 (2020).
6. C. Thoma, D. R. Welch, and S. C. Hsu, Phys. Plasmas **20**, 082128 (2013).
7. J. B. McBride *et al.*, Phys. Fluids **15**, 2367 (1972).
8. S. P. Gary, *Theory of Space Plasma Microinstabilities*, Cambridge Atmospheric and Space Science Series (Cambridge University Press, Cambridge, 1993).

Progress in Relativistic Laser–Plasma Interaction with Kilotesla-Level Applied Magnetic Fields

K. Weichman,[1] A. P. L. Robinson,[2] M. Murakami,[3] J. J. Santos,[4] S. Fujioka,[3] T. Toncian,[5] J. P. Palastro,[1] and A. V. Arefiev[6,7]

[1]Laboratory for Laser Energetics, University of Rochester
[2]Central Laser Facility, STFC Rutherford Appleton Laboratory
[3]Institute of Laser Engineering, Osaka University, Japan
[4]University of Bordeaux, CNRS, CEA, CELIA, France
[5]Institute for Radiation Physics, Helmholtz-Zentrum Dresden-Rossendorf, Germany
[6]Department of Mechanical and Aerospace Engineering, University of California, San Diego
[7]Center for Energy Research, University of California, San Diego

Recent advances in vacuum magnetic-field–generation techniques[1–6] have renewed interest in the fundamentals of laser–plasma interaction in the presence of strong magnetic fields. In part, this interest has been motivated by the potential for applied magnetic fields to benefit applications of laser–plasma interaction at relativistic intensity ($I_0 \sim 10^{18}$ W/cm^2 for ~1-μm wavelength), including ion acceleration, inertial fusion energy, and the laboratory study of astrophysical phenomena. This summary builds on recent progress in understanding the basic physics of relativistic laser–plasma interaction with kilotesla-level applied magnetic fields: surface magnetic fields and the diamagnetic effect in laser–solid interaction, the effect of embedded magnetic fields on plasma expansion and ion acceleration, and magnetic-field–associated changes in the direct laser acceleration of electrons.

First, although plasma is conventionally considered diamagnetic and often acts to exclude magnetic fields, laser–plasma interactions have long been known to self-generate strong fields[7] and amplify applied magnetic fields.[8] The spatial localization of hot-electron production from an overdense target and the presence of a neutralizing cold return current offer additional opportunities for magnetic-field generation and amplification associated with kinetic electron dynamics, among which is surface magnetic-field generation arising from the inability of the hot-electron current to change the applied field in a conductive opaque target.[9] This surface magnetic field can influence later plasma dynamics including target expansion[9] and may reverse the sign of the magnetic field generated by laser-driven implosions when it is destabilized.[10] The latter case is of particular interest as a platform for extreme magnetic-field amplification. However, the process underlying the sign reversal phenomenon[10,11] has yet to be conclusively settled. This work introduces a computationally efficient model that is predictive of the sign of the magnetic field produced in implosions. This model demonstrates correlation between sign reversal in cylindrical implosions and instability of the surface magnetic field in a simplified planar configuration (Fig. 1).

Second, until recently, the effect of applied magnetic fields on laser-driven plasma expansion and ion acceleration has primarily been studied in the context of astrophysical jet dynamics[12] involving long time-scale (~nanosecond) evolution in sub-100-tesla magnetic fields, which necessitates magnetohydrodynamic modeling and eliminates the consideration of kinetic effects. The sheath-based ion-acceleration regime driven by short, relativistic intensity laser pules, on the other hand, is conducive to multidimensional kinetic modeling. Recent work in this regime has revealed the possibility of using an applied magnetic field to reverse the typical outward divergence associated with target normal sheath acceleration into focusing and improving the ion energy and number.[13,14] In this case, ion focusing, which is highly desirable and much studied under nonmagnetized conditions, is produced by eventual magnetization of the electron sheath as the plasma expands.[14] Observing ion focusing experimentally, however, will require the spatial scale of the applied magnetic field to be comparable to or greater than the focal length. This work introduces
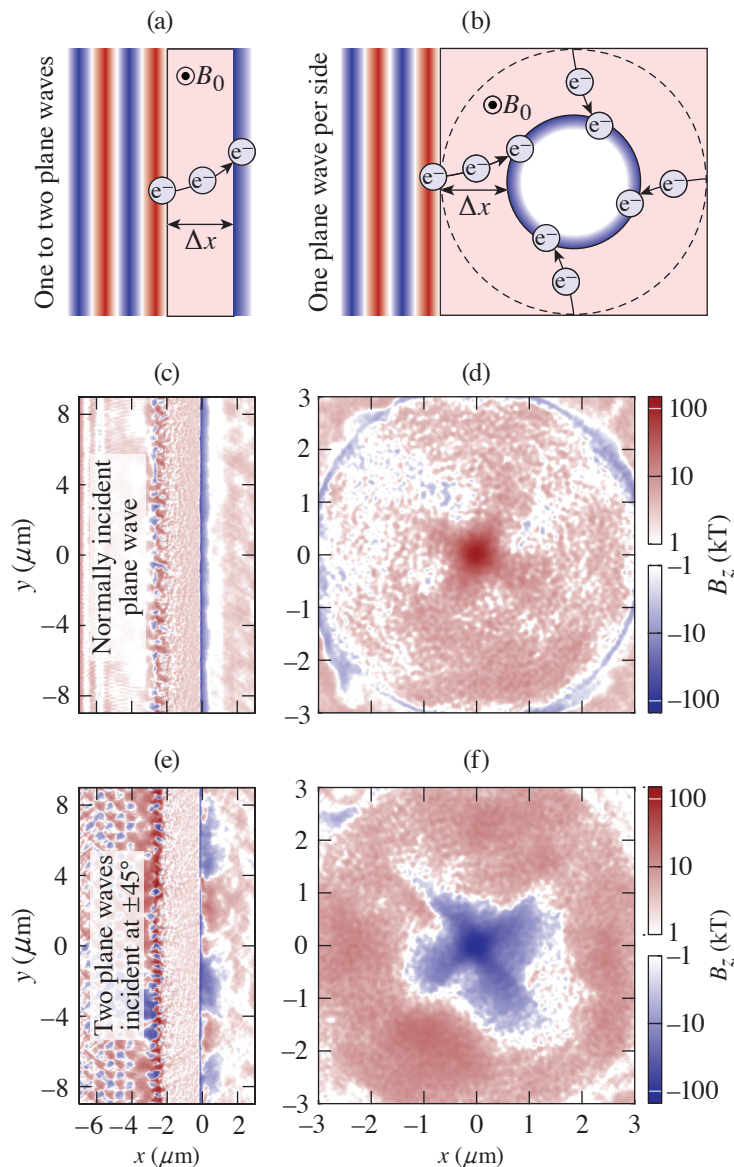
Figure 1
Planar model capturing surface magnetic-field stability and sign of the amplified field in implosions. [(a),(b)] Schematic of surface magnetic-field generation in (a) a planar target and (b) an implosion target with either square (solid line) or circular (dashed line) outer cross section. (c) Stable surface magnetic field in a planar target with normally incident plane wave pulse and (d) seed-aligned amplified magnetic field in a square implosion target. (e) Unstable surface magnetic field in a planar target with two obliquely incident pulses and (f) an amplified field in a circular implosion target.

a simple scaling model for sheath magnetization and subsequent ion focusing (Fig. 2). From this, realistic ion focal lengths are predicted that are likely compatible with the spatial extent of currently available applied magnetic fields.

Finally, while conventional electron acceleration mechanisms typically leave the majority of electrons cold either spectrally or spatially after the laser pulse has passed, direct laser acceleration (DLA) with an applied magnetic field is capable of volumetrically heating electrons to relativistic energy.[15–17] In the regime where the applied magnetic field affects the acceleration dynamics in a single accelerating laser half-cycle,[18] even modestly relativistic laser pulses can deliver significantly relativistic electron energy ($\gamma \sim 10$ or more). A configuration employing a secondary laser pulse prior to the main accelerating pulse (to provide the preheating necessary to enter this regime) was recently demonstrated to heat the majority of electrons in a large plasma volume to nonperturbatively relativistic energy.[18] The resulting optically diagnosable, relativistically thermal plasma is highly desirable for fundamental experimental studies in basic plasma physics, astrophysics and laboratory astrophysics, and laser-plasma physics. This work obtains an estimate for the average electron energy generated via magnetically assisted DLA (Fig. 3), which suggests plasma heating is most efficient for long, low (relativisitic)-intensity laser pulses.

(a)

(b)
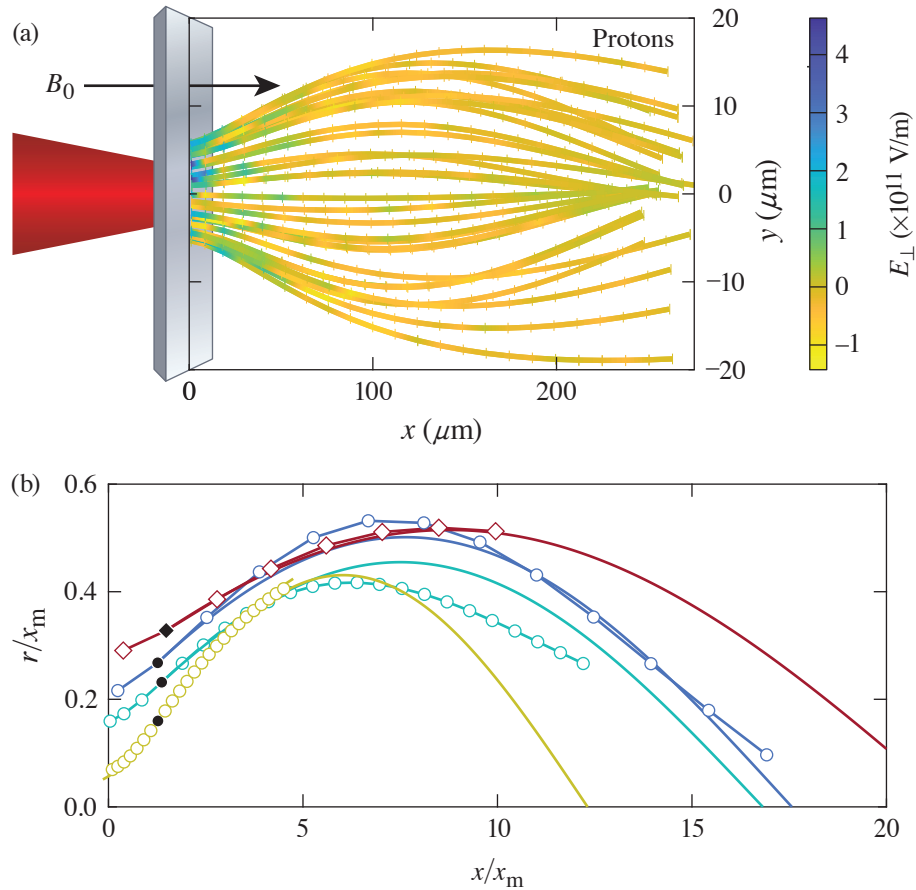
Figure 2

Model of ion focusing in magnetized electron sheath acceleration. (a) Schematic of ion acceleration with a target-normal applied magnetic field with proton trajectories. (b) Average high-energy proton trajectories from simulations keeping the laser waist divided by B_0 constant. $x_m \equiv (2\varepsilon_i T_e)^{1/2}/|e|B_0$.

TC16018JR

Together, these results highlight the promise of applied magnetic fields in relativistic laser–plasma interactions. Current magnetic-field capabilities can already enable novel and highly desirable phenomena relevant to laser-plasma applications. The continual development of magnetic-field–generation techniques supports these efforts by opening new parameter regimes to exploration.

1. S. Fujioka *et al.*, Sci. Rep. **3**, 1170 (2013).
2. J. J. Santos *et al.*, New J. Phys. **17**, 083051 (2015).
3. L. Gao *et al.*, Phys. Plasmas **23**, 043106 (2016).
4. C. Goyon *et al.*, Phys. Rev. E **95**, 033208 (2017).
5. V. V. Ivanov *et al.*, Rev. Sci. Instrum. **89**, 033504 (2018).
6. G. Fiksel *et al.*, Rev. Sci. Instrum. **86**, 016105 (2015).
7. Z. M. Sheng and J. Meyer-ter Vehn, Phys. Rev. E **54**, 1833 (1996).

(a)

(b)
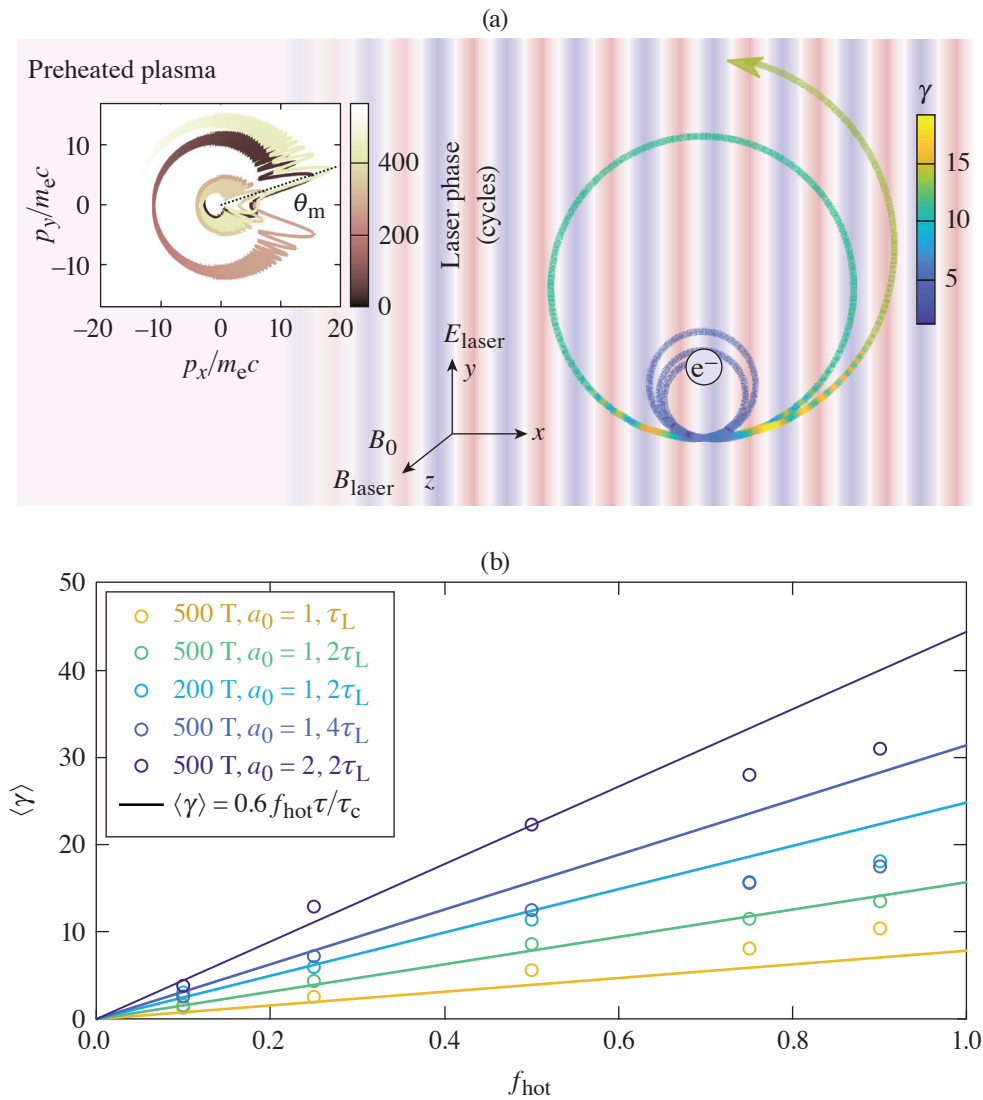
TC16020JR

Figure 3

Half-cycle magnetically assisted direct laser acceleration in a preheated plasma. (a) Example of the many-kick electron acceleration process. (b) Average electron energy from particle-in-cell simulations varying the initial fraction of electrons above the the threshold for energy gain (f_{hot}). τ, τ_L, and τ_C are the pulse duration, the maximum Larmor period after a single kick, and the non-relativistic cyclotron period, respectively.

8. O. V. Gotchev *et al.*, Phys. Rev. Lett. **103**, 215004 (2009).

9. K. Weichman *et al.*, New J. Phys. **22**, 113009 (2020).

10. K. Weichman *et al.*, Appl. Phys. Lett. **117**, 244101 (2020).

11. Y.-J. Gu and M. Murakami, Sci. Rep. **11**, 23592 (2021).

12. B. Albertazzi *et al.*, Science **346**, 325 (2014).

13. A. Arefiev, T. Toncian, and G. Fiksel, New J. Phys. **18**, 105011 (2016).

14. K. Weichman *et al.*, Sci. Rep. **10**, 18966 (2020).

15. A. V. Arefiev, A. P. L. Robinson, and V. N. Khudik, J. Plasma Phys. **81**, 475810404 (2015).

16. A. P. L. Robinson and A. V. Arefiev, Phys. Plasmas **27**, 023110 (2020).

17. K. Weichman *et al.*, "Underdense Relativistically Thermal Plasma Produced by Magnetically Assisted Direct Laser Acceleration," Physics Archive: https://doi.org/10.48550/arXiv:2202.07015 (2022).

18. A. Arefiev, Z. Gong, and A. P. L. Robinson, Phys. Rev. E **101**, 043201 (2020).

19. T. D. Arber *et al.*, Plasma Phys. Control. Fusion **57**, 113001 (2015).

20. J. Towns *et al.*, Comput. Sci. Eng. **16**, 62 (2014).

Single-Shot Electron Radiography Using a Laser-Plasma Accelerator

G. Bruhaug,[1,2] M. S. Freeman,[3] H. G. Rinderknecht,[1] L. P. Neukirch,[3] C. H. Wilde,[3] F. E. Merrill,[3] J. R. Rygg,[1,2,4] M. S. Wei,[1] G. W. Collins,[1,2,4] and J. L. Shaw[1]

[1]Laboratory for Laser Energetics, University of Rochester
[2]Department of Mechanical Engineering, University of Rochester
[3]Los Alamos National Laboratory
[4]Department of Physics and Astronomy, University of Rochester

To investigate the physical structure of compressed targets, laser-generated x-ray[1,2] or proton radiography[3–5] is typically used, with protons providing the extra feature of electromagnetic field sensitivity. Although x-ray and proton probes are the standard laser-generated diagnostic, there is another laser-generated probe that has seen little use: namely, relativistic electrons. Small-scale high-energy-density (HED) research facilities have performed electron radiography of ultrafast laser–plasma interactions,[6] but this capability has never before been extended to kJ- or MJ-class facilities. The work presented in this summary builds upon previous electron radiography (eRad) work using radio-frequency (rf) linear accelerators[7–9] and small-scale lasers[6–10] and extends it to kJ-class facilities via the already available picosecond lasers for electron-beam generation using a laser-plasma accelerator (LPA).[11,12]

Here, we report the first single-shot eRad images using an electron beam from a 100-J-class LPA. Both contact and projection radiography images of static targets were obtained in materials ranging from plastic to tungsten, and resolutions as good as 90-μm were achieved. This work lays the foundation for future electron radiography of laser-driven targets at kJ- and MJ-class facilities.

Radio-frequency–powered linear accelerators generate monochromatic, low-emittance electron beams suitable for high-quality electron radiography.[7–9] Such systems are rarely available, however, at the same facilities as large HED drivers and cannot easily be installed for experiments due to cost and space constraints. Nevertheless, these HED facilities often have ps lasers available, such as the OMEGA EP, NIF-ARC, PETAL, and Z-Petawatt lasers, which can be used to efficiently generate relativistic electron beams via LPA techniques.[11] This method could allow electron beams to be generated for radiography without needing to add a large and costly rf linear accelerator to an HED facility. A laser-driven eRad system also possesses the temporal characteristics that could make it an ideal diagnostic of other picosecond-scale processes for which linear accelerators do not provide sufficient instantaneous electron flux.

Electron radiography provides a complementary probe to existing x-ray and proton radiography techniques. Unlike laser-generated protons, laser-generated electrons are able to penetrate more material at a given energy. For example, a typical laser-generated 15-MeV proton will be fully stopped by ~2 mm of plastic at standard density and temperature, while a 15-MeV electron will require multiple centimeters of plastic to be fully stopped.[13] Relativistic electrons are also more sensitive to magnetic fields than protons for a given energy, but less sensitive to electric fields. This makes electrons an excellent complement to protons for radiography of electromagnetic fields.

The experiments were performed using the OMEGA EP LPA electron beam[11] and performed in both contact and projection radiography configurations (see Fig. 1).
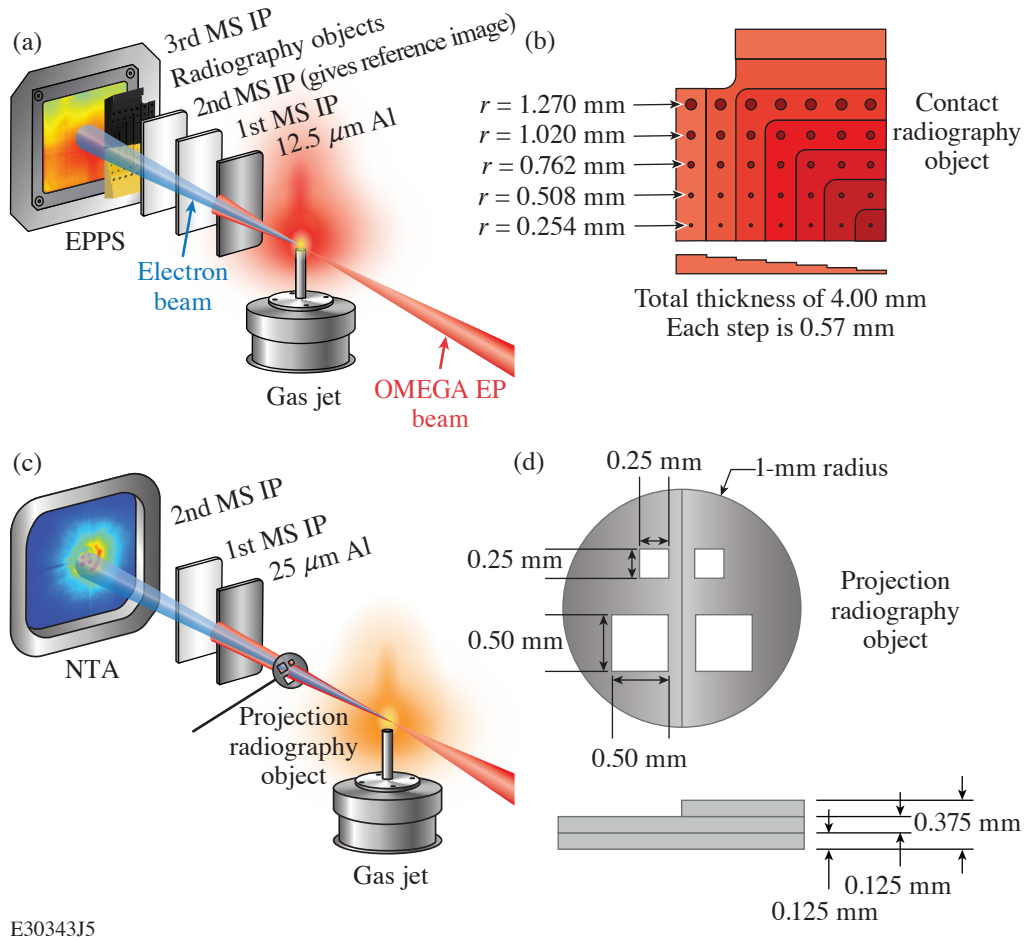
Figure 1

(a) Experimental setup for contact LPA eRad using radiography test objects (b) placed directly onto image plates and (c) projection LPA eRad using 2-mm-diam radiography test objects (d) offset from the image plates by distances ranging from 3.58 to 33.58 cm. MS IP: MS image plate; EPPS: electron–positron–proton spectrometer; NTA: near target arm.

Objects ranging from plastic to tungsten were radiographed at a wide variety of distances and thicknesses. This allowed testing the effect of target Z, density, thickness, and target magnification. The results of contact radiography can be seen in Fig. 2 and projection radiography in Fig. 3.

Resolutions nearing 90 μm were seen, but with little variation in magnification or target material. The resolution degraded with target thickness as expected, but nearly 4 mm of tungsten were able to be radiographed successfully. This shows the extreme penetrative capability of this new diagnostic platform. Laser-induced electric fields in projection radiography were also measured and found to be ~1 GV/m, which is in line with previous literature on the topic.[14]

1. E. L. Dewald *et al.*, Rev. Sci. Instrum. **89**, 10G108 (2018).

2. C. Courtois *et al.*, Phys. Plasmas **18**, 023101 (2011).

3. J. R. Rygg *et al.*, Science **319**, 1223 (2008).
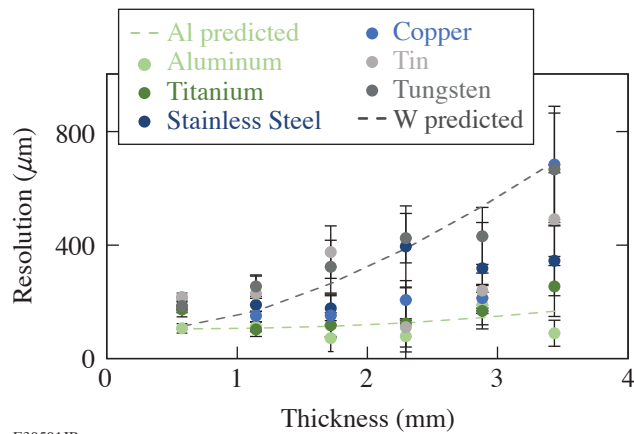
Figure 2
Average measured resolution of contact radiography test object versus target thickness. Theoretical predictions[15] for the tungsten and aluminum are included to guide the eye at the extremes of contact radiography test object Z numbers. The error bars are calculated using standard deviation between any repeat radiographs of the same target.
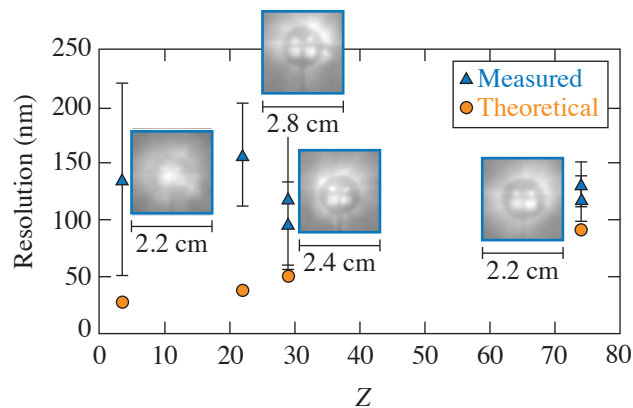
E30501JR

Figure 3
Resolution versus atomic number (Z) of the target material for the projection configuration when the image plate was 8 cm from the location of the best laser focus. Each data point has the radiograph recorded on the image plate next to it. Resolution is measured at the edges of each hole in the object as well as the outer edge. Error bars were calculated via the standard deviation between the resolution measurements on the same object.

E30338JR

4. A. B. Zylstra *et al.*, Rev. Sci. Instrum. **83**, 013511 (2012).

5. C. K. Li *et al.*, Phys. Plasmas **16**, 056304 (2009).

6. W. Schumaker *et al.*, Phys. Rev. Lett. **110**, 015003 (2013).

7. F. E. Merrill, Laser Part. Beams **33**, 425 (2015).

8. F. E. Merrill *et al.*, Appl. Phys. Lett. **112**, 144103 (2018).

9. F. Merrill *et al.*, Nucl. Instrum. Methods Phys. Res. B **261**, 382 (2007).

10. D. Hazra *et al.*, Phys. Rev. Accel. Beams **22**, 074701 (2019).

11. J. L. Shaw *et al.*, Sci. Rep. **11**, 7498 (2021).

12. F. Albert *et al.*, Nucl. Fusion **59**, 032003 (2018).

13. M. J. Berger *et al.*, (2017), *ESTAR*, *PSTAR*, and *ASTAR*: Computer Programs for Calculating Stopping-Power and Range Tables for Electrons, Protons, and Helium Ions (Ver. 2.0.1). [Online] Available: https://www.nist.gov/pml/stopping-power-range-tables-electrons-protons-and-helium-ions [17 August 2018].

14. J. L. Dubois *et al.*, Phys. Rev. E **89**, 013102 (2014).

15. A. Nassiri, Argonne National Laboratory, Urbana, IL, Report LA-165 (1991).

Development of a Hardened THz Energy Meter for Use on the Kilojoule-Scale, Short-Pulse OMEGA EP Laser

G. Bruhaug,[1,2] H. G. Rinderknecht,[1] Y. E,[3] M. S. Wei,[1] R. B. Brannon,[1] D. Guy,[1] R. G. Peck,[1] N. Landis,[1] G. Brent,[1]
R. Fairbanks,[1] C. McAtee,[1] T. Walker,[1] T. Buczek,[1] M. Krieger,[1] M. H. Romanofsky,[1] C. Mileham,[1] K. G. Francis,[3]
X. C. Zhang,[3] G. W. Collins,[1,2,4] and J. R. Rygg[1,2,4]

[1]Laboratory for Laser Energetics, University of Rochester
[2]Department of Mechanical Engineering, University of Rochester
[3]The Institute of Optics, University of Rochester
[4]Department of Physics and Astronomy, University of Rochester

Terahertz radiation occupies the frequency range between microwave and infrared radiation, making it a unique pump and probe of matter that interacts with matter in neither a purely photonic nor a bulk electronic fashion.[1–3] Because of the unique nature of THz radiation, there is a large interest in high-power sources for nonlinear time-domain spectroscopy and relativistic light–matter interactions at the extremes of low frequency;[1,3] however, the generation of such THz pulses is extremely difficult with traditional methods. Recent work with laser-plasma THz generation has shown great promise in scaling THz pulses to the terawatt and >100-mJ scale using ps, kJ-scale lasers to drive solid, liquid, or gaseous targets.[1] To maximize the THz power and pulse energy, lasers with both high energy (kJ) and high intensity (>10^{18} W/cm^2) must be used. These lasers are most commonly single shot and are well known for their immense electromagnetic pulse (EMP),[4] hard x-ray,[5] and charged-particle generation.[6] The OMEGA EP laser is especially challenging due to the peak EMP field measured being one of the highest seen on any laser (~500 kV/m) (Ref. 4). This adds to the already challenging task of THz detection due to the low efficiency (average of 0.1%) of laser THz generation in these systems. All available THz detection methods rely on electronics,[2] further compounding the EMP noise issue in these experiments.

This summary outlines the development of a ten-inch manipulator (TIM)–mounted THz energy meter, known as a THz background/energy meter (TBEM), for use on the kilojoule-class OMEGA EP laser and the associated challenges with the development of this detector. The TBEM is a broadband (0.3- to 10-THz or 1-mm to 30-μm) energy meter based on THz-sensitive pyrometers and capable of detecting broadband THz pulses as weak as ~50 μJ emitted in 4π or as strong as ~2 J emitted in 4π before suffering saturation of the detection element.

TBEM is a 112.5-cm-long, 20.9-cm-wide, TIM-mounted diagnostic weighing 33.1 kg primarily due to the inclusion of 19.8 kg of tungsten radiation shielding. As shown in Fig. 1, the diagnostic consists of a light-tight aluminum chassis with a front-mounted TPX[7] (THz and optical light transmissive) lens and filter pack extending 36.8 cm from the main body. This front lens allows for THz radiation to be collected 15 cm from target chamber center, maximizing the sensitivity of the detector. In front of the lens is a removable high-resistivity silicon wafer that acts as a THz-transmissive blast shield. The filter pack attached to the front lens can hold THz filters to alter the portion of the spectrum sampled and irises to reduce the amount of THz radiation sampled while operated in the forward position. This lens and filter assembly can also be removed and the detector operated while retracted from target chamber to further protect the electronics from EMP and radiation. A schematic of the detector and the THz transmission spectrum of the optical components can be seen in Fig. 2.

THz detection is accomplished by using commercially available nanojoule-sensitive pyrometers,[8] which are commonly used for commercial and scientific THz detection. A pyrometer is a broadband-sensitive energy meter that relies on the pyroelectric

E30139JR

(a)

(b)

E29796JR

Figure 2
(a) Full optical path of the TBEM detector and (b) THz transmission of the optical components and full detector.[7,9] PTF: polytetrafluoroethylene.

effect to detect a change in energy deposition.[2,8] The sensor is built in a series of layers similar to a capacitor with two electrodes around an inner layer of pyroelectric material. One electrode is darkened to best absorb the wavelength range of interest. Upon pulsed irradiation, the pyrometer will heat up and the polarization direction in the pyroelectric material will change. A charge disparity then develops across the pyroelectric crystal, and a voltage pulse is generated that is proportional to the amount of energy deposited into the sensor.

The initial concept for TBEM was built and tested for use on the Multi-Terawatt (MTW) laser to support THz target design campaigns. The results have been extremely promising. Four campaigns were then undertaken on OMEGA EP to test the TBEM detectors with the final two campaigns showing repeatable THz detection. The first campaign did not have the full complement of radiation shielding in place and suffered from massive x-ray and EMP noise problems (Fig. 3.). The second campaign had the radiation and EMP shielding upgraded and showed more-promising results. As with MTW, it was found that using plastic target stalks reduced the noise, but in this case the reduction was not enough to observe THz signal above the background.
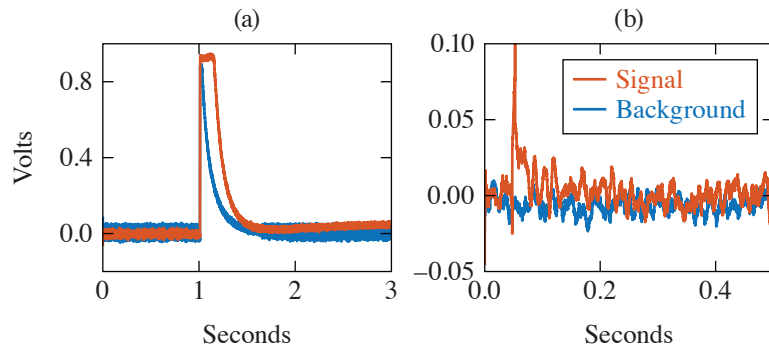
E30140JR

Figure 3
Example of data taken from one TBEM on the (a) first and (b) second OMEGA EP THz campaigns with ~100 J of laser energy used (July 2021 and March 2022, respectively). EMP and x rays, caused by extremely high background noise, can be seen in (a) when there was less shielding present on the detector.

For the third and fourth campaigns, the detectors were upgraded with the full complement of tungsten shielding described above, as well as improved cable EMP shielding. THz generation was reliably detected on both foil and microchannel targets with laser energies ranging from 100 to 500 J. Example THz detections from these experiments can be seen in Fig. 4.
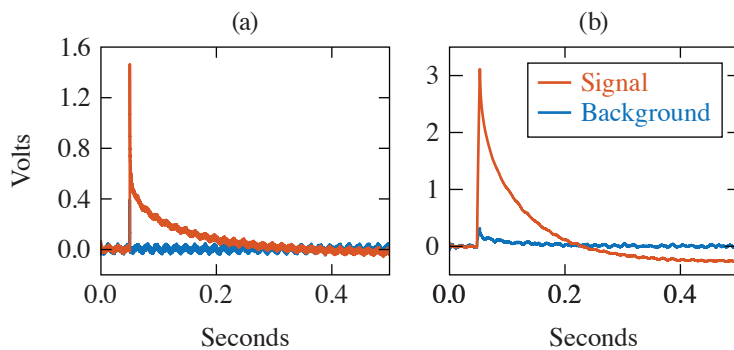
E30512JR

Figure 4
Example of data taken from one TBEM on third and fourth OMEGA EP campaign (June 2022): (a) from a foil irradiated with ~100 J of laser energy and (b) from a microchannel target irradiated with ~300 J of laser energy.

The THz yields were estimated to be ~130 mJ from the foil target and ~300 mJ from the microchannel target, which are in line with the estimated generation efficiencies of these target types for the given laser energy.[1,10] The additional EMP shielding on the pyrometer wiring was found to be crucial for the most energetic laser shots.

1. G. Liao *et al.*, Proc. Natl. Acad. Sci. **116**, 3994 (2019).

2. F. Sizov, Opto-Electronics Rev. **18**, 10 (2009); 223(E) (2010).

3. H. A. Hafez *et al.*, J. Opt. **18**, 093004 (2016).

4. S. Mondal *et al.*, J. Opt. Soc. Am. B **35**, A93 (2018).

5. C. Courtois *et al.*, Phys. Plasmas **18**, 023101 (2011).

6. J. L. Shaw *et al.*, Sci. Rep. **11**, 7498 (2021).

7. V. E. Rogalin, I. A. Kaplunov, and G. I. Kropotov, Opt. Spectrosc. **125**, 1053 (2018).

8. Gentec-EO, Accessed 23 March 2022, https://www.gentec-eo.com/products/qs5-thz-bl.

9. M. S. Kitai *et al.*, Radiophys. Quantum Electron. **57**, 881 (2015).

10. L. Yi and T. Fülöp, Phys. Rev. Lett. **123**, 094801 (2019).

Single-Shot Cross-Correlation of Counter-Propagating, Short Optical Pulses Using Random Quasi-Phase Matching

C. Dorrer and J. L. Shaw

Laboratory for Laser Energetics, University of Rochester

A single-shot cross-correlator based on the sum–frequency generation (SFG) of counter-propagating beams in SBN61 ($Sr_xBa_{1-x}Nb_2O_6$ with $x = 0.61$) has been demonstrated.[1] Random quasi-phase matching in disordered ferroelectric crystals such as SBN61 allows for nonlinear interactions in nonstandard geometries, e.g., the observation of a transverse second-harmonic–generation signal resulting from two co-propagating or counter-propagating pulses.[2,3] This diagnostic measures the cross-correlation between two laser facilities, leading to the relative delay between the pulses generated by each facility on every shot. It supports their precise co-timing and the study of their relative jitter with high precision over a time range larger than 150 ps.

The cross-correlation of optical pulses with instantaneous power profile $P_A(t)$ and $P_B(t)$ generated by the Multi-Terawatt (MTW) laser (λ_A = 1053 nm) and the idler of the MTW-OPAL laser (λ_B = 1170 nm) [Fig. 1(a)] were measured. The two beams are focused in a counter-propagating configuration in the underdense-plasma target chamber designed for Raman-amplification studies. Transverse SFG in an SBN61 maps out the cross-correlation signal $C_{AB}(\tau) = \int P_A(t)P_B(t-\tau)\mathrm{d}t$, where τ is the relative delay between the two pulses onto the longitudinal spatial coordinate. The generated transverse signal is re-imaged onto a camera, therefore allowing for single-shot cross-correlation acquisition over a range of relative delay set by the crystal length and group velocity of the two pulses, resulting in more than 150 ps for the 10-mm crystal used in these experiments. Both pulses generate a time-integrated transverse second-harmonic–generation signal at 526.5 nm and 585 nm, respectively, adding a background on the cross-correlation signal of interest [Fig. 1(b)]. Background-free acquisition with enhanced signal-to-noise ratio is obtained using a bandpass filter at the SFG wavelength (~550 nm). The cross-correlator has been used to co-time the two laser facilities at the common focal region where Raman-amplification in a gas jet are conducted. It has also provided valuable information on the relative jitter between the two laser facilities and for pulse-shape optimization.
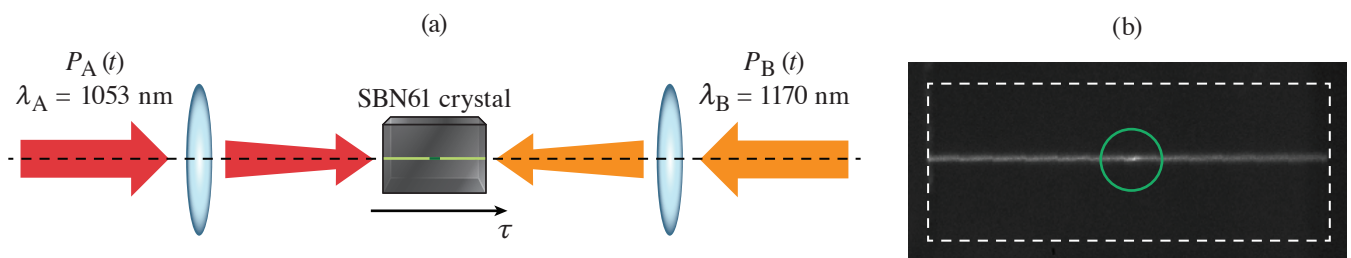
G13554JR

Figure 1

(a) Experimental setup. (b) Example of a signal acquired by the camera, without spectral filtering. The green circle identifies the cross-correlation signal, which is the only signal acquired by the camera when a bandpass filter at the SFG wavelength is used to remove the time-integrated SHG signals.

Fourier processing of the measured cross-correlation trace allows for extraction of its delay relative to reference and retiming for averaging purposes (Fig. 2). The collection of relative delays over a large number of shots represents the statistics of the jitter between the two laser facilities. As an example of application, Fig. 3(a) displays histograms of the relative delay between the two

G13555JR
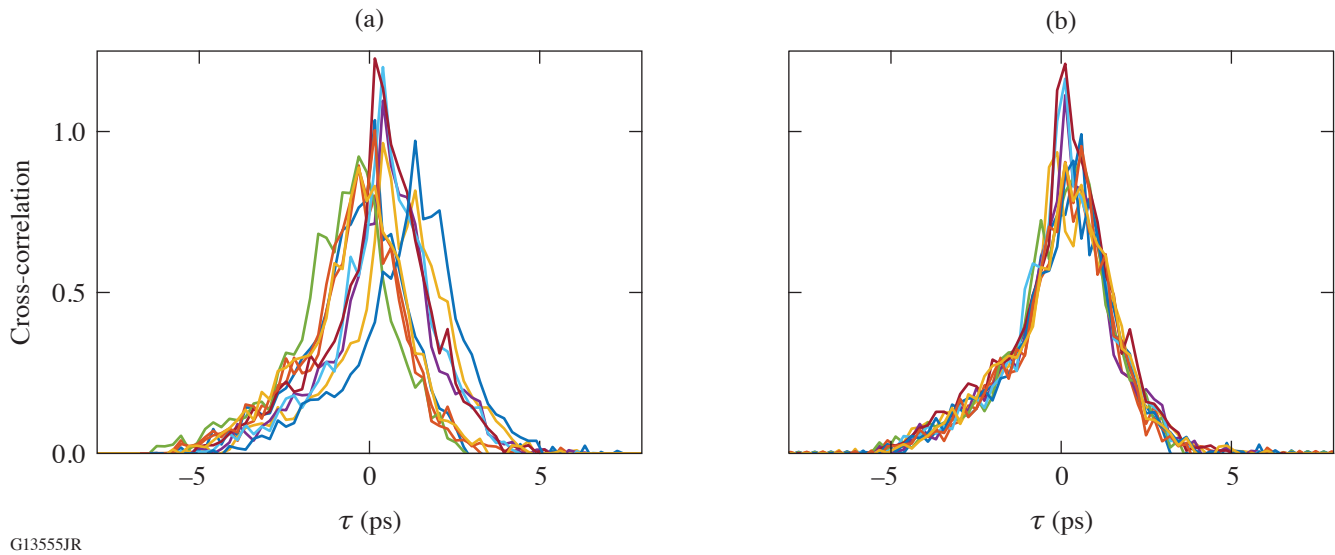
Figure 2
A set of ten measured single-shot cross-correlations (a) before and (b) after retiming.

G13560JR
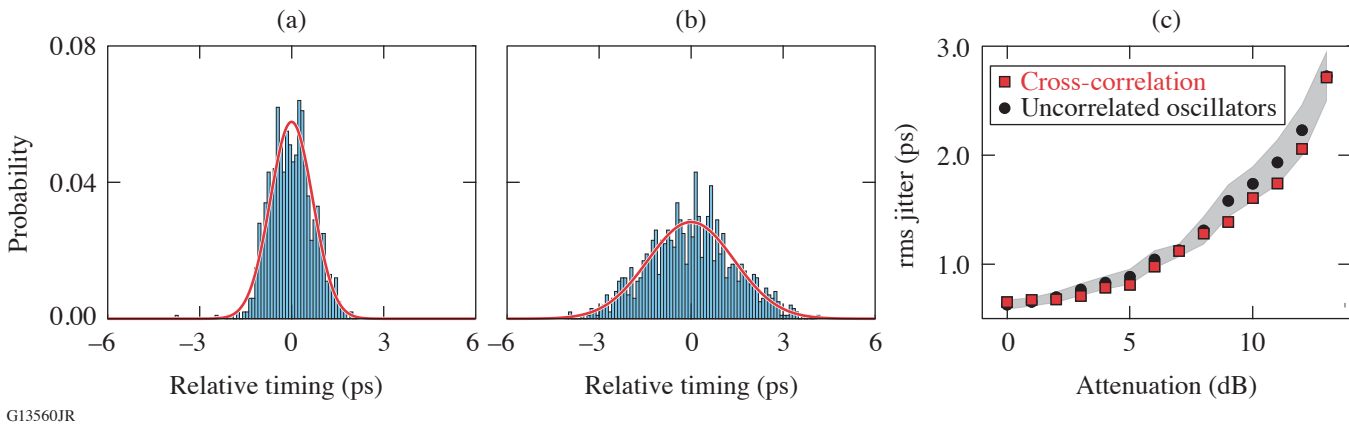
Figure 3
Probability histograms of the delay between the two laser sources measured (a) with a nominal synchronization-photodiode signal and (b) with a 9-dB attenuation. The bin size is 0.1 ps in all cases. A normal distribution with identical standard deviation has been added to (a) and (b) (red lines). On (c), the rms jitter determined from the measured cross-correlations (red squares) is compared to the rms jitter calculated from the jitter reported by the synchronization unit of the two mode-locked lasers (black circles, with confidence interval indicated by the shaded area).

facilities measured for three different synchronization configurations of the mode-locked laser seeding the MTW laser. Attenuation of its reference signal leads to poorer synchronization of that laser to the LLE reference frequency, thereby inducing a higher jitter for that particular laser and for the relative delay between the two facilities. The rms jitter calculated from the measured cross-correlations is in good agreement with the jitter calculated from the jitter of each mode-locked oscillator [Fig. 3(b)].

This simple approach supports the determination of the relative timing between two laser sources on a single shot, which is particularly important for low-repetition-rate sources. It also offers a direct approach to single-shot determination of the time-varying instantaneous power of an optical pulse by cross-correlation with a shorter ancillary pulse. Such determination is important for the development and optimization of chirped-pulse–amplification systems delivering pulses close to their Fourier transform–limited duration, but also for systems delivering pulses with a coherence time much shorter than their duration, e.g.,

incoherent pulses. Accurate single-shot temporal characterization with high resolution and long record length is paramount for safe operation and optimal interaction with the targets. SBN crystals as long as 20 mm are commercially available, leading to a 300-ps temporal window. Longer acquisition windows can be obtained by combining multiple crystals or implementing multiple passes in a single crystal with different relative delays between the two sources. Cross-correlations in disordered nonlinear crystals can also support the optimization of spatial overlap and timing in complex experiments involving multiple laser beams, such as the counter-propagating geometry used for Raman amplification and the crossing of beams at large angles used for Compton scattering.

1. C. Dorrer and J. L. Shaw, Opt. Express **30**, 16,677 (2022).

2. J. Trull *et al.*, Opt. Express **15**, 15,868 (2007).

3. R. Fischer *et al.*, Appl. Phys. Lett. **91**, 031104 (2007).

Multiparameter Laser Performance Characterization of Liquid Crystals for Polarization Control Devices in the Nanosecond Regime

K. L. Marshall,[1] K. R.P. Kafka,[1] N. D. Urban,[1] J. U. Wallace,[1,2] and S. G. Demos[1]

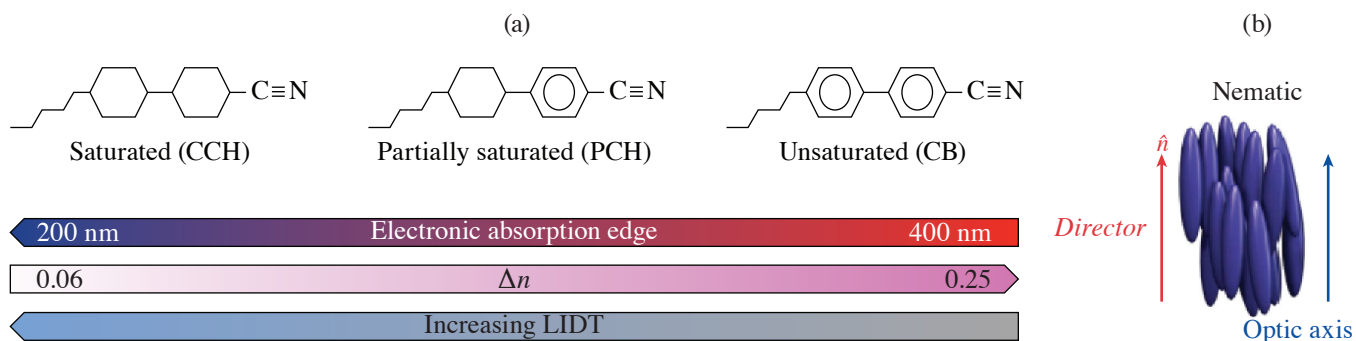[1]Laboratory for Laser Energetics, University of Rochester
[2]Department of Chemistry, D'Youville College

The interactions of liquid crystals (LC's) with polarized light have been studied widely and have spawned numerous device applications, including the fabrication of optical elements for high-power and large-aperture laser systems. Such devices have numerous advantages that include scalability to large apertures, cost effectiveness, high optical quality and contrast, broad angular tolerance, and laser-induced–damage thresholds (LIDT's) for optimized materials at 1054 nm of >30 J/cm^2, 3 J/cm^2, and 1 J/cm^2 at 1-ns, 10-ps, and 600-fs pulse durations, respectively.[1,2] Evaluation of the LIDT of LC materials has been performed historically in long-path-length LC cells (50 to 100 μm) to gain an understanding of the LC material's behavior under exposure to high-energy laser pulses without competing physicochemical interactions with surface-anchoring layers and conditions (LC elastic constants, boundary molecular tilt angle, alignment materials chemistry and application methods[2,3]). Although useful for screening LC materials by chemical class to determine general laser survivability, such long-path-length testing gives very little insight on how the LC's LIDT may be affected in device applications where the LC molecules are constrained in a monodomain alignment state induced by contact with substrates bearing a polymer alignment layer (e.g., wave plates, mirrors, and beam shapers). In such cases, variations in optical behavior as a function of laser beam polarization due to molecular orientation, chemical interactions, or generation of electric-field enhancements in the LC material are a distinct possibility.[4–6] This summary reports on the first study of the nanosecond-pulsed LIDT's dependence on incident polarization for several optical devices employing nematic and chiral-nematic LC's oriented by surface alignment layers. Accelerated lifetime testing was also performed to characterize the ability of these materials and devices to maintain their performance under multi-pulse irradiation with increasing laser fluence at both 1053 nm and 351 nm (Ref. 7).

Figure 1 shows generic molecular structures of LC components with differing degrees of π-electron density (saturation) that were evaluated for their multipulse laser damage behavior in optical element configurations typically used in high-peak-power lasers (e.g., circular polarizers and wave plates), where the LC molecular director, which defines the average long-range orientation of the LC molecular axes in the bulk, is constrained to adopt a monodomain or nearly monodomain orientation.

A pulsed nanosecond laser system operated at either its fundamental wavelength (1053 nm) or the third harmonic (351 nm) was used along with a novel detection system employing a polarization-sensitive camera to detect both the onset of performance degradation and classical LIDT of several LC mixture compositions in both circular polarizers and wave-plate device geometries. These measurements were designed to explore a "laser-induced functional threshold" (LIFT), defined as a reduction in one or more system-defined, key device functional parameters (e.g., transmission, reflection, birefringence, polarization rotation, contrast) that may occur at fluences lower than those required to produce the visible and permanent evidence of material modification typically defined as laser-induced damage. The point at which the value of LIFT drops below a system-defined tolerance metric is taken as the LIFT "trigger point." For the purposes of this study, the LIFT trigger pointy was a reduction in transmission to <98% (Ref. 7).

Testing of these LC materials at 1053 nm and 351 nm showed that their LIDT behavior depends significantly on the incident polarization state for laser light encountering the input surface of the LC test device at near-normal incidence (7°). For LC circular polarizer devices, the LIDT varied as a function of incident circular-polarization handedness by a factor of 30% to 80% for a given sample (Fig. 2). It appears that an angular dependence of high-peak-power LIDT on incident polarization in LC materials

(a)

Saturated (CCH) Partially saturated (PCH) Unsaturated (CB)

200 nm   Electronic absorption edge   400 nm

0.06 Δn 0.25

Increasing LIDT

(b)

Nematic

$\hat{n}$

Director

Optic axis

G13529JR

Figure 1

(a) Molecular structures for the three classes of LC compounds evaluated and a graphical representation of the dependence of optical absorbance, birefringence, and laser damage with respect to these classes. (b) Molecular ordering in the nematic LC phase. For this class of LC materials, both the LC director and the optic axis are parallell to the molecular axis.

(a)

Reflected CPL   Incident linear

Transmitted CPL

(b)

Transmitted CPL

(c)

RH circular polarizer, LIDT = 30.5 J/cm^2

$\geq 10\ p$ Chiral nematic LC (RH helix)

RHCP incident   RHCP transmitted

$\lambda_r = \bar{n}p$

Substrates

(d)

LH selective reflector, LIDT = 17.7 J/cm^2

LHCP reflected $\geq 10\ p$ Chiral nematic LC (RH helix)

LHCP incident $\lambda_r = \bar{n}p$

LHCP reflected   Substrates
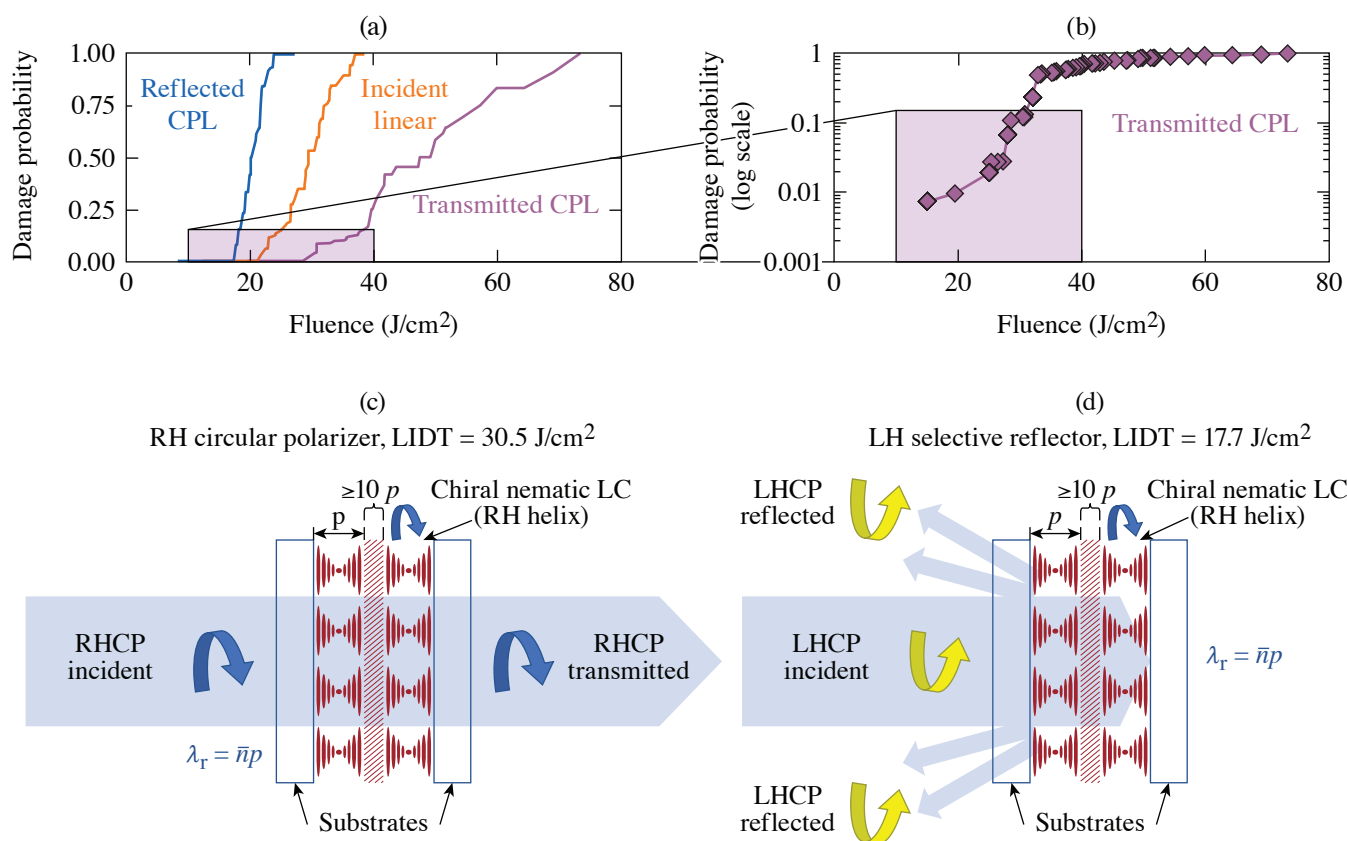
G13441JR

Figure 2

(a) Damage probabilities for the chiral-nematic LC circular polarizer/isolator device as a function of 1053-nm, 1.4-ns laser fluence and incident polarization; (b) damage probabilities for transmitted circularly polarized light pulses incident on the device at low fluence [corresponding to the inset in Fig. 2(a)]. The data, plotted on a logarithmic scale, represent an additional 250 sites of 1-on-1 damage data collected by line-scanning the sample; [(c),(d)] the interaction of circularly polarized light of opposite handedness on the LC structure, along with the representative LIDT thresholds. For (c), incident circular polarized light with the same twist sense as the LC helix (right-handed) is transmitted, whereas in (d) for the same device, incident circular polarization of the opposite handedness (left-handed) is selectively reflected due to Bragg scattering. A cell thickness of at least ten pitch lengths (*p*), indicated by the area filled with diagonal slashes near the center of the cell, is required to observe these effects with sufficient magnitude for device applications.

has not been reported previously. The results suggest that multipulse functionality was best preserved in LC devices having the highest degree of saturation.

Certain compositions of saturated, UV transparent nematic LC mixtures evaluated in a wave-plate geometry displayed remarkable robustness in LIFT testing at 351 nm, with one CCH-based LC mixture (LLE1202) being able to survive as many as 1000 1-ns pulses at 2 J/cm^2 (5-Hz repetition rate) before displaying any significant change in its functional performance (Fig. 3). The LIDT was seen to vary as a function of input polarization by 30% to 80% within the same device, while the multi-pulse LIFT depends on irradiation conditions such as laser fluence and wavelength.
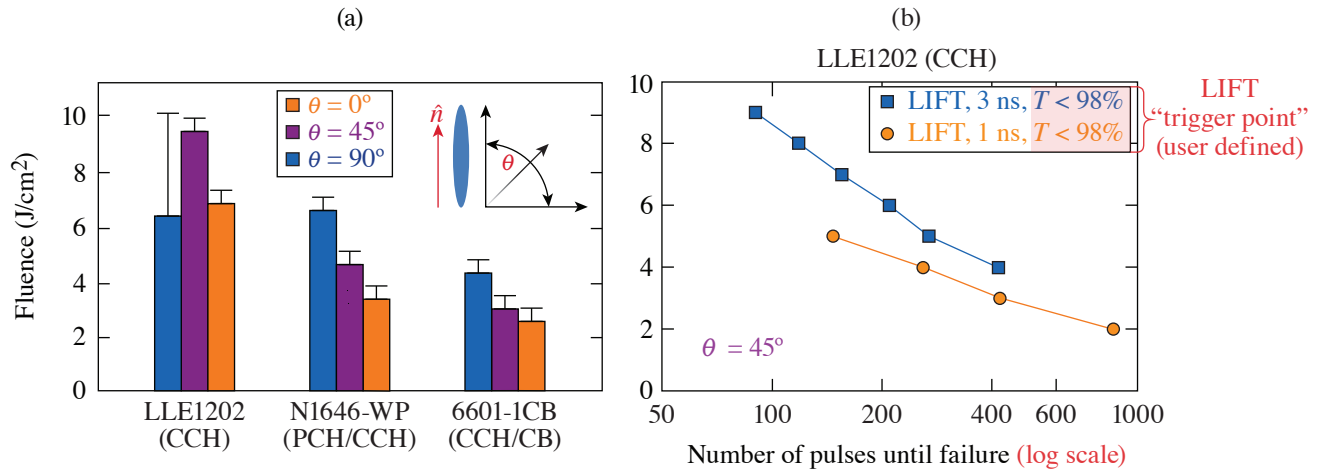
G13443JR

Figure 3

(a) LIDT at 351-nm, 1-ns pulse duration as a function of incident linear polarization angle with respect to the LC director. Uncertainty bars extend to the nominal 0% and 100% damage probability fluences. (b). LIFT results for LLE1210 at 351 nm for both 1-ns and 3-ns laser pulses delivered at a 5-Hz repetition rate. The high saturation of this CCH-based LC material allows it to withstand nearly 1000 pulses at 2 J/cm^2. The inset in (a) shows the orientation of the LC director with respect to the incident laser polarization.

These promising results highlight the potential of this class of LC materials in nanosecond-regime, high-peak-power lasers such as OMEGA for applications as polarization control and polarization-smoothing optics. Another distinct advantage of LC optics is that in the event they do sustain damage, they can be refurbished and reinstalled in a laser system with a relatively low cost of materials and effort. The results also illustrate the necessity of taking the molecular structure and electron delocalization of LC mesogens into account when designing new materials for such emerging applications.

1. S. D. Jacobs *et al.*, J. Opt. Soc. Am. B **5**, 1962 (1988).
2. T. Z. Kosc *et al.*, Sci. Rep. **9**, 16435 (2019).
3. A. Schmid *et al.*, Mol. Cryst. Liq. Cryst. **207**, 33 (1991).
4. J. Lu *et al.*, J. Appl. Phys. **80**, 5028 (1996).
5. C.-H. Wen, S. Gauza, and S.-T. Wu, J. Soc. Inf. Disp. **13**, 805 (2005).
6. Y. H. Wang *et al.*, IEICE Trans. Electron. **E-83-C**, 1553 (2000).
7. K. L. Marshall *et al.*, Sci. Rep. **12**, 10969 (2022).

Influence of Heat Treatments on Near-Surface Tritium Concentration Profiles

M. Sharpe, W. T. Shmayda, and J. J. Ruby

Laboratory for Laser Energetics, University of Rochester

At room temperature, tritium interacts with all metals (aluminum, copper, stainless steel, etc.) to some extent.[1] Such interactions can lead to a buildup of tritium on the metal's surface and just under the surface of the metal.[2–4] The presence of high tritium concentrations in these locations is a large concern for all tritium-handling facilities. These facilities contain a large quantity of metals that routinely come in contact with tritium gas. Over time, tritium buildup in these metals can lead to radiological hazards and high waste disposal costs. To mitigate tritium contamination in metals, it is common to heat the metal to high temperatures.[5,6] The details of this thermal desorption method (maximum temperature, dwell time, etc.) depend on the contaminated metal as well as the expected tritium dosing. To date, however, no systematic study has been performed showing how tritium migrates within the metal as a result of a chosen thermal desorption temperature and time. The current work addresses this gap in knowledge by showing how the tritium distribution within stainless steel, type 316 (SS316) responds to temperatures between 100°C and 300°C. The surface and near-surface concentrations were measured using a combination of a $ZnCl_2$ wash and sequential acid etching to reveal a high-resolution tritium concentration profile. Tritium deeper within the metal was measured using high-temperature thermal desorption to remove residual tritium from the bulk metal.

To measure the effect of heating on the tritium distribution within SS316, a series of samples were first exposed to tritium gas for 8 h at 25°C. Each sample was then heated to temperatures between 100°C and 300°C for 120 min under a stagnant, dry argon atmosphere. The tritium distribution was then measured by performing a $ZnCl_2$ wash first to remove surface tritium. Following this wash, the samples were then acid etched to reveal the tritium concentrations immediately under the surface (<100 μm). Finally, the residual tritium deeper in the samples was measured using high-temperature thermal desorption (550°C for 4 h). For comparison, several control samples were not heated prior to the $ZnCl_2$ wash, acid etching, and high temperature thermal desorption procedures.

The resulting concentration profiles (Fig. 1) show two notable deviations from the control samples. First, the surface activity decreases significantly with increasing preheating temperature as expected. Second, the near-surface (1 nm to 1 μm) tritium concentrations differ for only the 200°C and 300°C cases; the 100°C and 150°C preheating appears to have had no influence on the near-surface concentrations. Heating to temperatures greater than or equal to 200°C resulted in decreased concentrations in the near surface (~0.1 μm).

Integrating the concentration profiles shown in Fig. 1 reveals the total tritium remaining within each region of the SS316 sample. These integrals (Fig. 2) show that surface-bound tritium decreases with increasing preheating temperature, while tritium deeper in the metal (>1 μm) increases. Tritium quantities in the intermediate region (<1 μm) remain constant until the sample is heated to 200°C or greater. Above 200°C, the quantity of tritium decreases to a new, lower value.

These data indicate how tritium migrates within SS316 in response to moderate heating. Heating SS316 causes tritium to desorb from the surface and migrate deeper into the metal. Taking the median values of the data shown in Fig. 2, the quantity of tritium "lost" from the surface is greater than the tritium activity released from the surface. This indicates that tritium preferentially migrates into the metal as opposed to desorbing from the surface. Desorption from the surface is possibly not as favorable due to the gas conditions. The samples were kept under dry argon during the preheating phase. Past studies have shown that tritiated
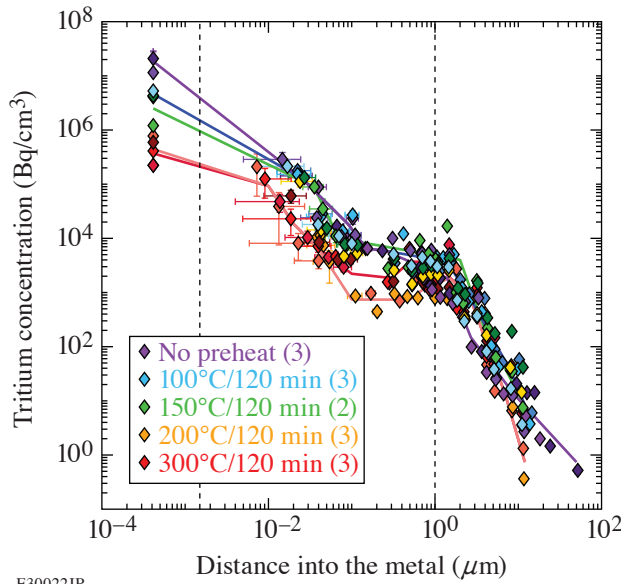
Figure 1
Tritium concentration profiles in the near surface of SS316 samples. Five preheating conditions are shown: no heating (purple), 100°C (blue), 150°C (green), 200°C (orange), and 300°C (red). Vertical dashed lines indicate different regions of the sample: surface (<1 nm), near-surface (<1 μm), and bulk (>1 μm). Each preheating condition was repeated with different SS316 samples that were exposed to tritium at the same time.

E30022JR
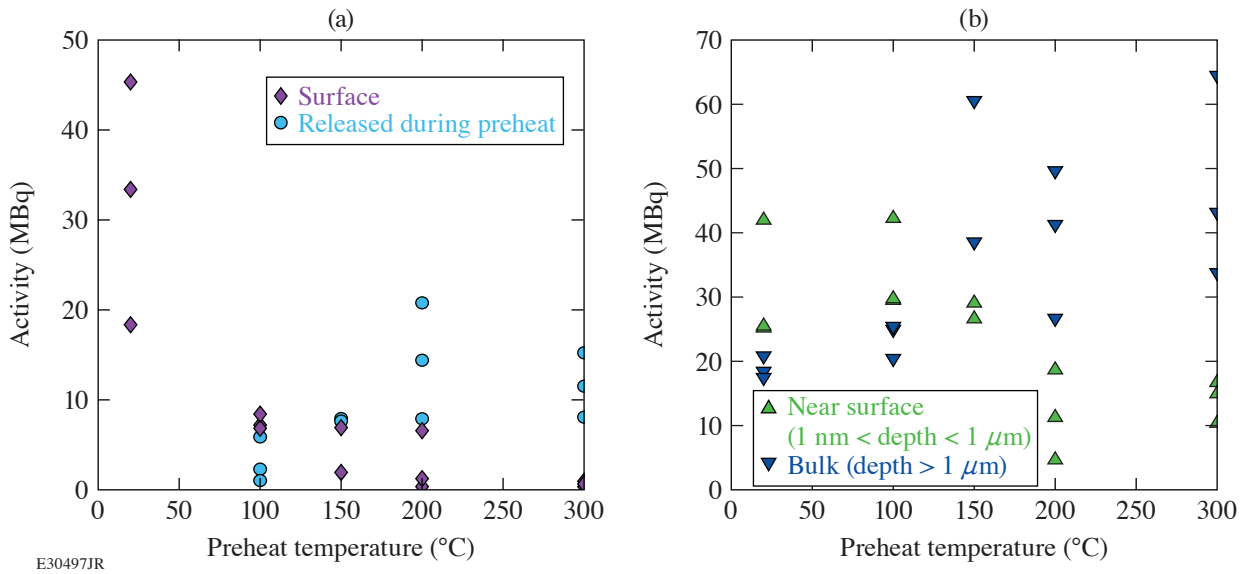
Figure 2
(a) Integrated tritium remaining on the surface and released during preheating and (b) tritium remaining in the near surface and bulk with respect to the preheating temperatures. Results from control samples are shown at 20°C.

water desorption is the primary release mechanism of tritium from SS316.[7–9] By limiting this mechanism for tritium desorption from the surface, tritium will preferentially migrate in the direction of the concentration gradient deeper into the metal.

Tritium quantities in the near surface do not appreciably change until the preheat temperature reaches 200°C (Fig. 1). These results indicate that a minimum temperature of 200°C is required to trigger near-surface tritium mobility for migration deeper into the substrate or desorption from the surface. Previous work has also demonstrated that heating SS316 to at least 200°C is required for the onset of desorption.[10,11] The increase in migration above 200°C indicates that tritium immediately below the surface is not bound at octahedral sites. The depletion of the near surface tritium and the increased desorbed tritium quantities by heating to 200°C suggests that tritium is bound in a hydrated iron (III) oxide: FeO(OH). Such binding explains three observations: First, hydrogen isotopes can be bound strongly to oxygen impurities in metals. Korzhavyi and Sandström used a density functional

theory calculation to simulate hydrogen interacting with an oxygen defect in copper.[12] Their results show a fourfold increase in the binding energy, as compared to a site without oxygen. Assuming oxygen in stainless steel has a similar effect, such deep trap states may explain the observed lack of tritium migration during the lengthy storage periods. Second, dehydration of hydrated iron (III) oxide occurs at 200°C (Ref. 13). Because tritium would be bound in the hydrate, dehydration would remove tritium from the near-surface region. Finally, dehydration may supply the oxygen and hydrogen/tritium necessary for tritiated water desorption from the surface. In this scenario, the primary pathway for tritium desorption is present even for dry inert gas atmospheres: the metal effectively supplies the water molecules for desorption.

The effect of heat treatments on the tritium distribution in SS316 samples was measured. It was found that the heating causes tritium to migrate both out of the sample and deeper into the bulk of the material. Tritium preferentially migrates deeper into the metal for temperatures less than 200°C, with very little desorbing from the surface. On reaching 200°C or above, dehydration of the hydrated iron (III) oxide occurs. The dehydration process reduces the tritium inventory in the near surface by allowing tritium to either desorb from the surface as tritiated water or diffuse deeper into the metal.

1. M. Nishikawa *et al.*, J. Nucl. Mater. **277**, 99 (2000).

2. A. Perevezentsev *et al.*, Fusion Sci. Technol. **41**, 746 (2002).

3. M. D. Sharpe *et al.*, Fusion Eng. Des. **130**, 76 (2018).

4. M. Sharpe, C. Fagan, and W. T. Shmayda, Fusion Sci. Technol. **75**, 1053 (2019).

5. A. N. Perevezentsev *et al.*, Fusion Sci. Technol. **52**, 84 (2007).

6. S. Rosanvallon *et al.*, Fusion Sci. Technol. **60**, 855 (2011).

7. K. Akaishi *et al.*, J. Vac. Sci. Technol. A **26**, 321 (2008).

8. M. J. Quinlan *et al.*, Fusion Sci. Technol. **54**, 519 (2008).

9. Y. Torikai *et al.*, Fusion Sci. Technol. **41**, 736 (2002).

10. W. T. Shmayda *et al.*, Fusion Sci. Technol. **68**, 766 (2015).

11. R.-D. Penzhorn *et al.*, Fusion Sci. Technol. **64**, 45 (2013).

12. P. A. Korzhavyi and R. Sandström, Comput. Mater. Sci. **84**, 122 (2014).

13. N. N. Greenwood and A. Earnshaw, eds. *Chemistry of the Elements*, 2nd ed. (Elsevier, New York, 1997).

Effective Mass Determination in Highly Resistive GaAs by Exploiting the Influence of a Magnetic Field on Optically Excited Transient THz Surface Emissions

G. Chen,[1,2] D. Chakraborty,[1,2] J. Cheng,[1,2] M. Mikulics,[3] C. Chimera,[4] I. Komissarov,[4] R. Adam,[5] D. E. Bürgler,[5] C. M. Schneider,[5,6] H. Hardtdegen,[3] and R. Sobolewski[1,2,4]

[1]Laboratory for Laser Energetics, University of Rochester
[2]Materials Science Graduate Program, University of Rochester
[3]Research Centre Jülich, Ernst Ruska Centre for Microscopy and Spectroscopy with Electrons, Germany
[4]Department of Electrical and Computer Engineering, University of Rochester
[5]Research Centre Jülich, Peter Grünberg Institute (PGI-6), Germany
[6]Department of Physics, University of California Davis

Generating broadband, free-space terahertz transients by pumping the surface of a semiconductor with femtosecond optical laser pulses is a well-established technique, generally called THz surface emission.[1] Several radiation models have been proposed to explain the THz surface emission such as surface depletion created by the internal electric field perpendicular to the sample surface,[2–5] nonlinear optical rectification,[6,7] and photocurrent generated by the photo-Dember effect.[8–10] It was also demonstrated that an external magnetic field applied in the plane of a semiconductor can tune the amplitude of the surface-emitted THz radiation. The enhancement of the THz amplitude was ascribed to the Lorentz force, induced by the applied magnetic field, which introduced an additional acceleration to the photocarriers.[11,12] Time-domain, nonequilibrium carrier relaxation dynamics can be characterized by an optical pump–probe spectroscopy technique,[13] which allows one to further analyze how the Lorentz force affects photocarriers and to determine the relationship between the THz transient amplitude enhancement and the semiconductor carrier mobility.

For these studies, five different, highly resistive (111)-oriented GaAs samples characterized by different mobilities and crystal-line conditions were used. Namely, a standard semi-insulating GaAs wafer (SI GaAs), a semi-insulating GaAs wafer annealed at 300°C (annealed GaAs), and three nitrogen-ion–implanted GaAs specimens, implanted at an energy of 191 keV with a dose of $\sim 8 \times 10^{11}$ ions/cm^2 (Refs. 14 and 15), and, subsequently, annealed at 300°C, 350°C, and 400°C, denoted as N-GaAs 300, N-GaAs 350, and N-GaAs 400, respectively.

Experiments were performed using THz time-domain spectroscopy (THz-TDS) and optical femtosecond pump–probe spectroscopy (F-PPS). In both cases, a commercial Ti:sapphire laser that generated a train of nominal, 100-fs-wide laser pulses at 800-nm wavelength and 76-MHz repetition rate was used. In the THz-TDS setup,[16] the laser beam was split into two branches with a 90:10 power ratio. The high-power branch, after bouncing from a retroreflector mounted on a delay stage, was focused on our test GaAs sample to generate bursts of electromagnetic radiation, i.e., single-picosecond transients with the frequency spectrum extending into THz, while the low-power branch was used for the THz transient detection and focused on a commercial low-temperature–grown GaAs photoconductive (PC) THz detector with z-axis polarization sensitivity (perpendicular to the optical table).[17] A 5-mm-diam and $\sim$10-mm-focal-length Teflon™ (polytetrafluoroethylene) lens, located between the test sample and the THz detector, collimated the transmitted THz radiation. In addition, an external magnetic field **B** was applied in the sample plane along the x axis, while the surface-emitted THz radiation was collected along the y direction, as indicated in Fig. 1. The F-PPS system was implemented to measure the nonequilibrium carrier dynamics in the samples. In this setup[18,19] optical pulses were split into two beams by a 60/40 beam splitter. Pump pulses had the higher power, and the beam was modulated with an acousto-optic modulator. The lower-power probe beam was delayed with respect to the pump by reflection from a retroreflector
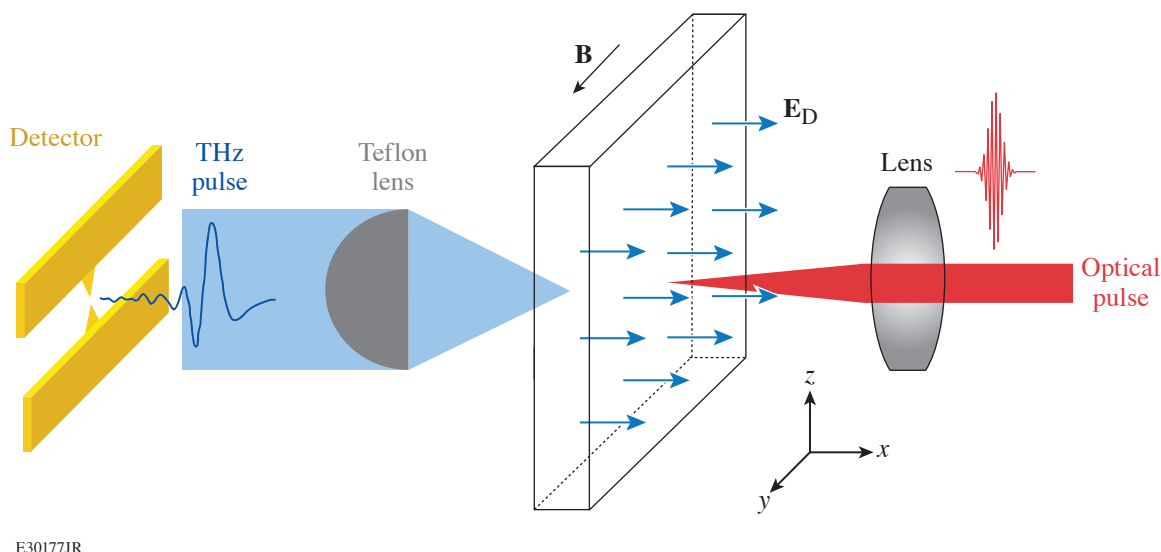
E30177JR

Figure 1

Schematics of the basic experimental geometry. The surface of the sample is parallel to the x–z plane. The built-in depletion electric field $\mathbf{E}_D$ is along the y axis and perpendicular to the sample surface. A lens is used to focus a laser beam at the surface of the sample, and a Teflon lens placed after the sample collimates the emitted THz radiation toward a PC THz detector aligned in such a way that it can only sense the z component of the THz transient. An external magnetic field applied along the x axis was used in the $\mathbf{B}$-field enhancement experiments.

mounted on a delay stage. Both pump and probe beams were focused on the same spot of the sample; the beam size of the probe (~20 μm in diameter) was kept slightly smaller than that of the pump beam (~30 μm in diameter) to ensure probing only the optically excited area of the sample. To limit the probe-related electron heating to a minimum and to ensure a decent signal-to-noise ratio, the power ratio of the pump to probe beams was set to ~10:1. The probe beam was reflected at the sample surface and directed toward a photodetector connected to a lock-in amplifier to record the normalized reflectivity change ($\Delta R/R$) waveforms as a function of the time delay between the pump and probe pulses.

Figure 2 shows the dependence $k = (q/m^*)\tau_1$, where q is the elementary charge, m^* is the electron effective mass, and τ_1 is the relaxation time, for all five types of GaAs samples (black circles) and reveals a universal linear relationship (black solid line). This indicates that τ_1, derived based on the Drude model, is the trapping time for the samples. During this time, the Lorentz force accelerates electrons before they get trapped by defect states. Therefore, a high density of defects/traps in a semiconductor, e.g., in case of the N-GaAs samples, leads to a shorter carrier lifetime, which, in turn, limits the impact of the magnetic field on the THz transient.

The next important conclusion from Fig. 2 is that within the linear fit, the effective mass $m^* = q/(k/\tau_1)$ for all samples is exactly the same and the extracted value is $m^*/m_0 = 0.059$ (m_0 is the electron mass), which is close to the accepted value of 0.063 for GaAs single crystals,[20] and illustrated by the dashed line corresponding to the k dependence for $m^*/m_0 = 0.063$. The latter is an interesting result and shows that despite the large differences in the crystallinity of the test samples, the effective mass derived from our magnetic-field experiments remains constant and very close to the effective mass of electrons in GaAs with a perfect crystalline structure. The only deviation from the ideal m^* value observed was for the annealed GaAs sample. Contrary to the other samples, the clear distinction between trapping and recombination processes is somewhat difficult to establish.

In conclusion, we exhaustively analyzed the transient emission of THz signals, emitted from highly resistive GaAs samples with different crystallinity, excited by femtosecond optical pulses. The observed magnetic field impacted the THz transient generation, and the corresponding enhancement factor was directly proportional to the applied $\mathbf{B}$ field. Interestingly, the slope of the enhancement factor dependence was directly proportional to the samples' nonequilibrium trapping time measured using
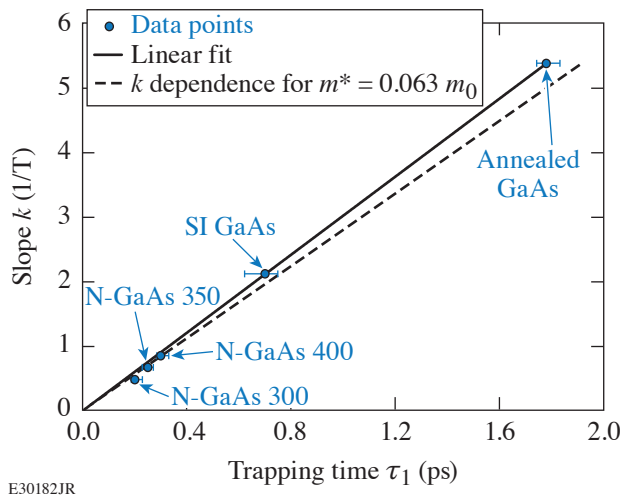
Figure 2
Dependence of the slope k on the trapping time τ_1. The circles are experimental data, and the black line is the best linear fit yielding $m^*/m_0 = 0.059$. The dashed line corresponds to the k dependence for the literature $m^*/m_0 = 0.063$.

femtosecond optical pump–probe spectroscopy. The latter enabled the determination of the electron effective mass $m^*/m_0 = 0.059$ that was very close to the literature m^* value for GaAs single crystals. The latter reveals that GaAs samples with very different crystallinity, including highly defected, N-implanted samples, all have an m^* value essentially equal to that of the ideal crystal.

1. X.-C. Zhang *et al.*, Appl. Phys. Lett. **56**, 1011 (1990).
2. X.-C. Zhang and D. H. Auston, J. Appl. Phys. **71**, 326 (1992).
3. R. Kersting *et al.*, Phys. Rev. B **58**, 4553 (1998).
4. J. N. Heyman *et al.*, Phys. Rev. B **64**, 085202 (2001).
5. J. S. Hwang *et al.*, Appl. Phys. Lett. **87**, 121107 (2005).
6. S. L. Chuang *et al.*, Phys. Rev. Lett. **68**, 102 (1992).
7. M. Reid, I. V. Cravetchi, and R. Fedosejevs, Phys. Rev. B **72**, 035201 (2005).
8. K. Liu *et al.*, Phys. Rev. B **73**, 155330 (2006).
9. R. Mendis *et al.*, J. Appl. Phys. **98**, 126104 (2005).
10. A. Reklaitis, J. Appl. Phys. **108**, 053102 (2010).
11. X.-C. Zhang *et al.*, Appl. Phys. Lett. **62**, 2003 (1993).
12. C. Weiss, R. Wallenstein, and R. Beigang, Appl. Phys. Lett. **77**, 4160 (2000).
13. A. Othonos, J. Appl. Phys. **83**, 1789 (1998); **84**, 1708(E) (1998).
14. M. Mikulics *et al.*, Appl. Phys. Lett. **87**, 041106 (2005).
15. M. Mikulics *et al.*, Appl. Phys. Lett. **88**, 041118 (2006).
16. R. Adam *et al.*, Appl. Phys. Lett. **114**, 212405 (2019).
17. A. Geižutis *et al.*, Opt. Mater. **30**, 786 (2008).
18. J. Zhang *et al.*, J. Appl. Phys. **110**, 113112 (2011).
19. J. Serafini *et al.*, Semicond. Sci. Technol. **31**, 045006 (2016).
20. G. Margaritondo, in *Encyclopedia of Condensed Matter Physics*, edited by F. Bassani, G. L. Liedl, and P. Wyder (Elsevier, Oxford, 2005), pp. 311–321.

An Assessment of Generating Quasi-Static Magnetic Fields Using Laser-Driven "Capacitor" Coils

J. L. Peebles, J. R. Davies, D. H. Barnak, F. Garcia-Rubio, P. V. Heuer, G. Brent, R. Spielman, and R. Betti

Laboratory for Laser Energetics, University of Rochester

Over the previous decade, numerous experiments have been performed using a laser to drive a strong, quasi-static magnetic field. Field strength and energy density measurements of these experiments have varied by many orders of magnitude, painting a confusing picture of the effectiveness of these laser-driven coils (LDC's) as tools for generating consistent fields. At the higher end of the field energy spectrum, kilotesla field measurements have been used to justify future experimental platforms, theoretical work, and inertial confinement fusion concepts. In this work we present the results from our own experiments designed to measure magnetic fields from LDC's as well as a review of the body of experiments that have been undertaken in this field. We demonstrate how problems with prior diagnostic analyses have led to overestimates of the magnetic fields generated from LDC's.

The first aspect of these experiments that must be addressed is conversion of laser energy to magnetic-field energy. While it is easy to claim results are feasible as long as energy in the magnetic field is less than the energy in the driving laser, the reality is that no laser experiment has a significant amount of free energy to generate a magnetic field. For certain experiments, the total laser absorption can be as high as 90%, but for the majority of experiments using drivers similar to those in most LDC experiments, it is much lower (50%). Hot-electron production is a potential source of free energy. Up to ~30% of the laser energy could be converted to hot electrons at the higher values of $I\lambda^2$ used.[1] For the parameters of most LDC experiments with lower $I\lambda^2$, however, a smaller percentage of the laser energy would be converted into hot electrons.[2] When considering that all the potential energy sinks for this conversion, at most half the energy put into hot electrons can be converted to current. Therefore, a physically reasonable upper limit on laser-energy conversion to magnetic energy would appear to be 15% and, in most cases, should be much less. Examining each LDC experiment's energy conversion by integrating the field energy density ($B^2/2\mu_0$) over a $10 \times 10 \times 10$-mm^3 volume produces the results in Fig. 1.[3–15]

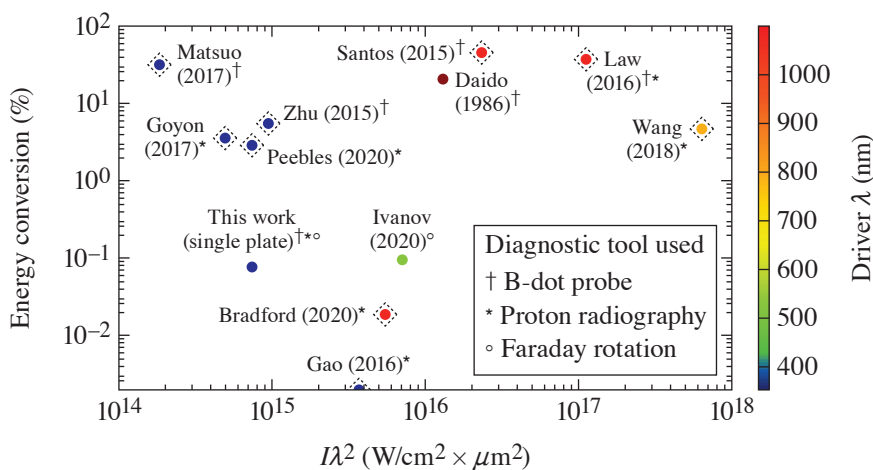Figure 1

The calculated energy conversion from laser energy to field energy for the variety of LDC experiments.[3–15] Superscripts denote the diagnostic tool used to arrive at the result, while dotted diamonds around a shot indicate the presence of a short-pulse beam on the experiment. Experiments with conversion over 10% stand out because they have suspiciously high energy conversion.

E30081JR

Looking at the body of experiments, a trend emerges: several experiments measured fields that contained energy equal to 30%–40% of the energy of the driving laser. These experiments also coincidentally measured the primary result using the B-dot while a short-pulse, high-intensity laser was present. This is highly indicative that the B-dot probe responds differently to these experiments than other diagnostics. To address this, we performed our own experiments with LDC's using the entire battery of magnetic-field diagnostics: axial and transverse proton probing, Faraday rotation, and B-dot probes, as shown in Fig. 2. Two types of coils were tested to examine the effect of having the second plate on the target and were driven by a 1-ns, up-to-1.25-kJ, long-pulse UV beam.

(a)
Double radiography configuration

(b)
Faraday rotation

E30069JR
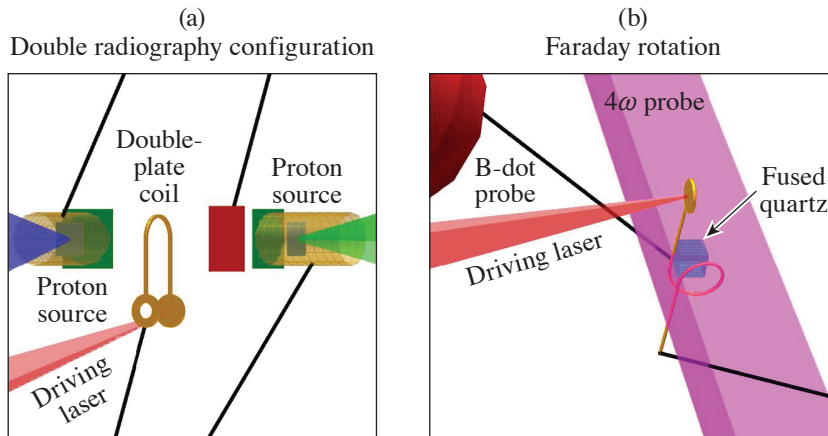
Figure 2
Experimental platform used to study the fields generated by LDC targets using a battery of diagnostics. (a) One campaign used both the sidelighter and backlighter beams to simultaneously probe the coil transverse and axially with protons. (b) A setup used the 4ω probe with a piece of fused quartz for Faraday rotation (polarimetry). All experiments had a B-dot probe placed roughly 2 cm from the loop attached to a 6-GHz-bandwidth balun and scope.

Several results from our experiments are shown in Fig. 3. A 40-T reference magnetic field was generated by MIFEDS (magneto-inertial fusion electrical discharge system) and probed by the axial proton probe [Fig. 3(a)]. As protons travel through the magnetic field, a secondary deflection from the radial magnetic field induces a rotation of the reference mesh. This rotation increases with field strength and decreases with proton energy. The same proton probe was applied to our LDC's and produced no measurable rotation. This indicates that the magnetic field in the LDC is below the measurement threshold (20 kA in the coil) for the axial probe. Using the more-sensitive transverse proton probe on the LDC produces a bulge near the top of the LDC, indicative of a small current of 2.5 kA. This current is far below that measured by most of the experiments shown in Fig. 1 and indicates a much poorer laser-to-field-energy conversion ratio.

(a)

(b)

(c)
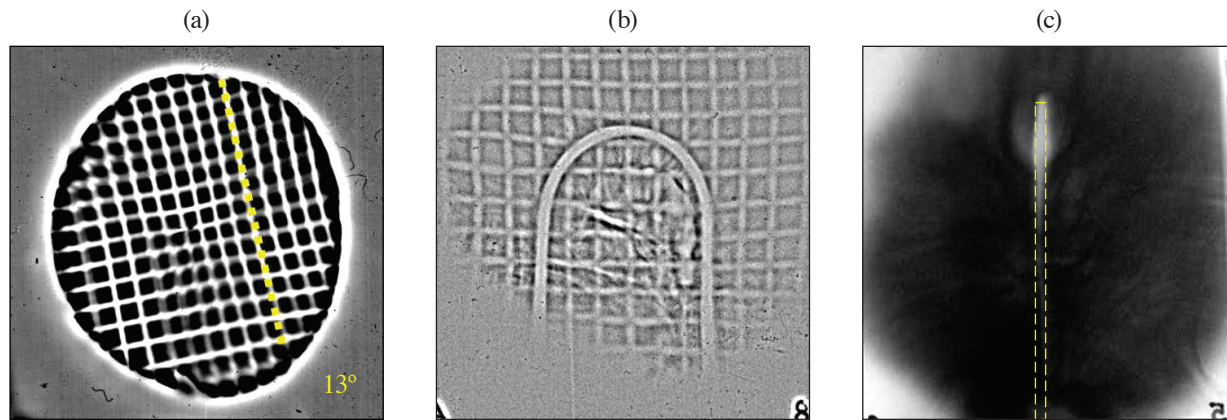
E30080JR

Figure 3
Axial proton probes of a known magnetic field generated by (a) MIFEDS and (b) a double-plate LDC. In (a) MIFEDS generated a 40-T field that induced an apparent rotation of the mesh fiducial dependent on the proton energy. This diagnostic technique is sensitive to fields generated by currents greater than 20 kA. In (b) no such rotation is measured, indicating that any current must be less than 20 kA. (c) A transverse proton probe of the same LDC shows a slight bulge near the top of the coil, indicating a current of ~2.5 kA.

Supplementing the proton radiography measurements were the Faraday rotation and B-dot probe diagnostics. Faraday rotation measures the magnetic field in a medium by comparing the rotation difference between orthogonal polarizations as they pass through the medium in the presence of a magnetic field. In the case of our LDC experiment, no significant rotation was measured in the two polarizations of the 4ω probe. The error in the measurement between the two polarizations is $\pm 2\%$, which corresponds to a measurement limit of a 7.5-kA current in our coil, consistent with a 2.5-kA measurement of the proton probe. The B-dot probe acquired measurements in all experimental configurations, both with and without the short-pulse beams. When comparing the data in Fig. 4 it is clear that the B-dot probe is heavily influenced by the presence of the short-pulse beam. Since the short pulse-beams were timed 1 ns after the long-pulse drive beam in order to probe the interaction after the drive, the signal contributions between the two types of beams can be differentiated on the scope. When we account for the scope and cable attenuation based on assumed signal frequency, the signal from the long-pulse beam implies a current of 62.5 kA, much higher than all other diagnostics. The signal from the short pulse is roughly an order of magnitude higher than that of the long pulse, implying a very unrealistic current of over 600 kA.
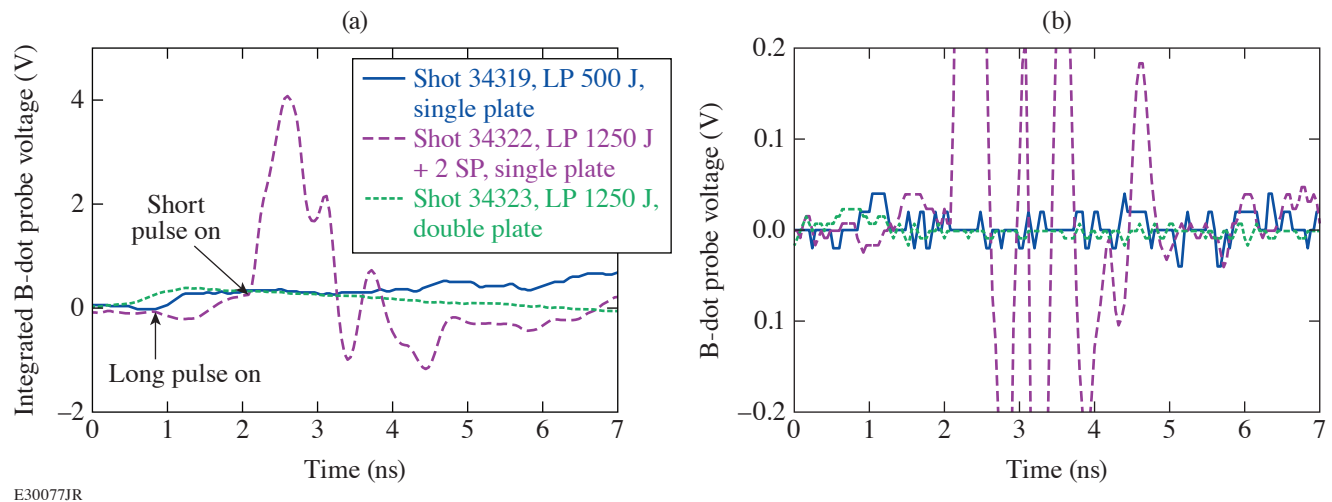

E30077JR

Figure 4

(a) Integrated B-dot probe signals for three different shots: two without short-pulse beams with different coil types and one with the short-pulse beams. The signal with the short-pulse beams is over 10× higher (4 V compared to 0.34 V) than that of the long-pulse beam drive only. The spike in signal from the short pulse is delayed compared to the long pulse due to the beam timings used on the experiment and time of flight from target to B-dot probe. (b) Raw data for the same shots, demonstrating the poor signal-to-noise ratio on the experiments without the short pulse. The signal is varying as quickly as the diagnostic can measure, indicating that the majority of signal is oscillating faster than 6 GHz.

While a B-dot probe (with differentiation) is designed in theory to measure only a changing magnetic field, in reality the entire probe and cabling is subject to effects that are not completely neutralized, such as capacitive coupling, where electric fields can induce significant voltage. The signal generated on the B-dot probe by the short-pulse beam clearly indicates current that is unphysical from a conservation of energy perspective; however, this effect explains the conclusions of many previous LDC experiments shown in Fig. 1. The "highest performing" experiments also utilized a B-dot probe in conjunction with proton radiography using a short-pulse, high-intensity beam. Similar to our experiment, other diagnostics (proton radiography or Faraday rotation) typically indicated field values far lower than the B-dot probe; however, in most of these experiments the B-dot probe result is given preference because of its larger value, despite the poorer accuracy of the method. When we account for this short-pulse interference of the B-dot probe, the majority of results fall into more-reasonable energy conversion ratios of, at most, a few percent.

We began experiments on laser-driven coils to develop a consistent platform for applying and measuring external magnetization of an experiment. In some regards we were successful: a field was measured that was relatively consistent across all diagnostics; however, the field values we measured departed severely from those in other publications. These experiments comprehensively demonstrated that laser-driven coils are not well described by a circuit or capacitor model nor do they produce

uniform consistent fields. Our experiments at best could convert less than a percent of driving laser energy into the magnetic field at the coil, far less than the optimistic conclusions of other experiments. B-dot probes and Faraday rotation were found to be ineffective at measuring magnetic fields in our higher-power LDC experiments because they were subject to the extreme radiation and electric-field environment. Proton radiography produced a precise and detailed picture of electrostatic and magnetic fields around the LDC, but a higher degree of confidence in our conclusions drawn from radiographs was obtained only by probing in two directions simultaneously.

1. J. R. Davies, Plasma Phys. Control. Fusion **51**, 014006 (2009).
2. C. Garban-Labaune *et al.*, Phys. Rev. Lett. **48**, 1018 (1982).
3. H. Daido *et al.*, Phys. Rev. Lett. **56**, 846 (1986).
4. J. J. Santos *et al.*, New J. Phys. **17**, 083051 (2015).
5. K. F. F. Law *et al.*, Appl. Phys. Lett. **108**, 091104 (2016).
6. C. Courtois *et al.*, J. Appl. Phys. **98**, 054913 (2005).
7. A. Tarifeño, C. Pavez, and L. Soto, J. Phys.: Conf. Ser. **134**, 012048 (2008).
8. L. Gao *et al.*, Phys. Plasmas **23**, 043106 (2016).
9. C. Goyon *et al.*, Phys. Rev. E **95**, 033208 (2017).
10. W. Wang *et al.*, Phys. Plasmas **25**, 083111 (2018).
11. B. J. Zhu *et al.*, Appl. Phys. Lett. **107**, 261903 (2015).
12. K. Matsuo *et al.*, Phys. Rev. E **95**, 053204 (2017).
13. V. V. Ivanov *et al.*, Phys. Plasmas **27**, 033102 (2020).
14. P. Bradford *et al.*, High Power Laser Sci. Eng. **8**, e11 (2020).
15. J. L. Peebles *et al.*, Phys. Plasmas **27**, 063109 (2020).

Pulsed-Power Innovations for Next-Generation, High-Current Drivers

R. B. Spielman

Laboratory for Laser Energetics, University of Rochester

Recent proposals to build larger high-current drivers to be used for high-energy-density physics, inertial confinement fusion, radiation effects testing, and basic science will present challenges.[1] Drivers significantly larger than the Z Machine at Sandia National Laboratories encounter increasing difficulties in water power flow, insulator performance, and vacuum power flow. The physics requirements of imploding loads limit a designer's flexibility in choosing machine parameters such as current rise time, driving impedance, and total inductance. This summary enumerates these physics constraints and shows how they impact driver design. This leads to the conclusion that advances in pulsed-power understanding and pulsed-power capabilities are needed to control risk and to build a cost-effective driver at peak currents of ~60 MA.

The Z machine, driving an imploding load, requires a peak insulator voltage of ~4 MV while delivering up to 25 MA to the load.[2] The current rise time is ~100 to 110 ns and the overall implosion times are 100 ns to 120 ns (Refs. 3–5). Scaling Z today at 25 MA to a new next-generation pulsed-power facility (NGPPF) at 60 MA requires that the driving voltage scale proportionally with the increased peak current (other parameters held constant). This results in a driver with a peak voltage at least ~2.4× larger than Z.[6,7] These scaled voltages will exist at all locations in the driver for all times during the pulse. This summary describes the physics constraints on driver parameters, discusses the pulsed-power impact on the pulsed-power design, and finally asks if advances in pulsed-power physics understanding and pulsed-power engineering can reduce the risk and cost of an NGPP driver.

Magneto-Rayleigh–Taylor (MRT) physics drives Z-pinch drivers to implosions times of 100 ns or less.[2,8,9] In the case of an NGPPF driver, implosion quality is paramount. It becomes difficult to justify a significant increase in the implosion time (current rise time) to reduce the voltage (and power) risk beyond 100 ns unless MRT can be stabilized to some extent.

Electrical coupling efficiency to the load is a huge part of driver optimization. Simplistically, the electrical coupling (to stored magnetic energy) is optimized when $L/Zt \sim 1$, where L is the total inductance of the load, Z is the impedance of the driver, and t is the rise time of the current. Given from MRT consideration that the current rise time t is constrained, we see that increases in the load inductance L must be accompanied by an increase in driver impedance Z. However, the coupling efficiency to the load is $\sim \Delta L/L$, where ΔL is the change in inductance due to the dynamic load and L here is the total final inductance. For a convergence ratio of ~10:1, the change in inductance of a 2-cm-long load is ~9.4 nH. We see that coupling to the load is optimized for lower total inductances. As a result, the overall coupling efficiency from available driver energy drives us to a lower inductance and lower impedance driver. The driver inductance and impedance are not free parameters.

Higher-voltage NGPP drivers force larger gaps in the water section of any driver because, for a voltage rise time of ~100 ns, the threshold for electrical discharges in water is 300 kV/cm. The only ways to increase the gap in the water section near the load are to increase the radius of the insulator stack (height scales with radius at constant impedance) and increase the impedance of the water lines. Both of these approaches will be required.

The largest-diameter parts that can be built and shipped across the country are roughly 6 m in diameter. With this assumption, the only additional way to increase the driver voltage is by using multiple levels of insulators and magnetically insulated

transmission lines (MITL's). (See Fig. 1 for a four-level example.) The key advantage of increasing the number of MITL levels is an increase in the water transmission-line gap for a given insulator stack radius because the levels are driven in parallel. A secondary impact is the paralleling of the MITL inductances at the post-hole convolute. Inductance is a secondary impact because the reduced current per MITL level forces an increase in MITL inductance to hold the electron vacuum flow nearly constant. The number of MITL levels and the insulator stack radius effectively determine the maximum current for a given design.
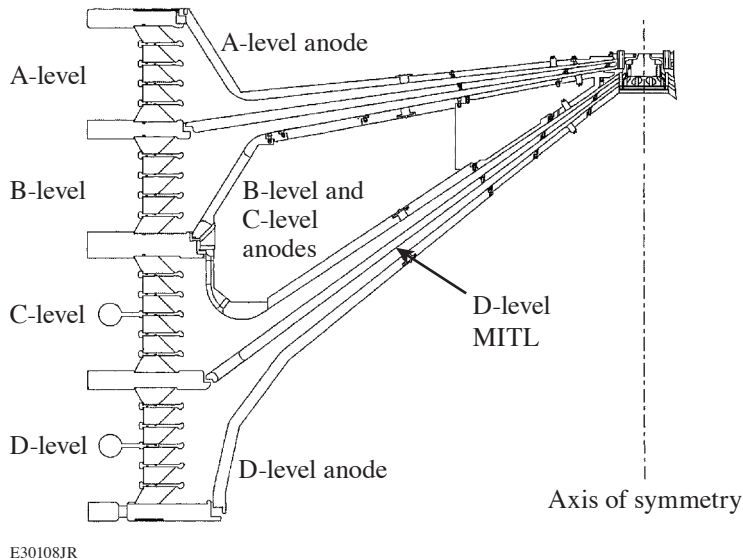

Figure 1
Schematic of a double-disk MITL that shows the insulator stack, the vacuum flare region, the MITL's, the post-hole convolute, the inner disk MITL, and the load region.

E30108JR

An impedance of $Z = 6.67$ h/r Ω per level for a four-level MITL is used to estimate the peak current of a Z machine–like design. One potential design impedance is 0.180 Ω, so the individual level impedance is now increased to 0.72 Ω. This results in a water-transmission line gap of 32.4 cm at a radius of 3 m. Following the arguments of maximum electric field above, the peak allowed voltage is ~4.8 MV and the peak current is ~50 MA. Higher-current drivers will require a larger-radius insulator stack, a higher driving impedance, and/or more MITL levels.

The increased voltage on NGPPF (everywhere and at all times) will create difficulties in pulsed-power design and result in increased current losses and reduced coupling efficiency to dynamic loads. Mitigating losses by increasing physical gap results in an increase in inductance that reduces peak current and decreases coupling efficiency. Further increases in driving voltage are required to obtain the design load current. This is a strong feedback effect that can limit the overall magnitude of a potential NGPP driver. Kinetic energy delivered to a relevant load becomes the key metric for comparing various driver designs. It is possible to design a pulsed-power driver that achieves 60 MA at the load that couples insufficient energy to a dynamic load.

It is likely that there is an effective limit to the peak current and kinetic energy of a pulsed-power driver that is based on cost, shot rate, and programmatic impact. A 60-MA-class driver can be built but such a driver, based on today's pulsed-power understanding, will be costly and inefficient.

1. D. B. Sinars *et al.*, Phys. Plasmas **27**, 070501 (2020).

2. T. W. Hussey and N. F. Roderick, Phys. Fluids **24**, 1384 (1981).

3. E. A. Weinbrecht *et al.*, in *2005 IEEE Pulsed Power Conference*, edited by J. Maenchen and E. Schamiloglu (IEEE, Monterey, CA, 2005), pp. 170–173.

4. M. E. Savage *et al.*, in *16th IEEE International Pulsed Power Conference*, edited by E. Schamiloglu and F. Peterkin (IEEE, New York, 2007), Vol. 2, pp. 979–984.

5. M. E. Savage *et al.*, in 2011 IEEE Pulsed Power Conference, edited by R. P. Joshi (IEEE, Piscataway, NJ, 2011), pp. 983–990.

6. W. A. Stygar *et al.*, Phys. Rev. Spec. Top., Accel. Beams **10**, 030401 (2007).

7. W. A. Stygar *et al.*, Phys. Rev. ST Accel. Beams **18**, 110401 (2015).

8. N. F. Roderick and T. W. Hussey, J. Appl. Phys. **56**, 1387 (1984).

9. T. W. Hussey *et al.*, Phys. Plasmas **2**, 2055 (1995).

FY22 Q2 Laser Facility Report

J. Puth, M. Labuzeta, D. Canning, and R. T. Janezic

Laboratory for Laser Energetics, University of Rochester

During the second quarter of FY22, the Omega Facility conducted 322 target shots on OMEGA and 238 target shots on OMEGA EP for a total of 570 target shots (see Tables I and II). OMEGA averaged 9.9 target shots per operating day, averaging 90.8% Availability and 95.6% Experimental Effectiveness. OMEGA EP averaged 8.8 target shots per operating day, averaging 94.8% Availability and 96.9% Experimental Effectiveness.

Table I: OMEGA Laser System target shot summary for Q2 FY22.

Program	Laboratory	Planned Number of Target Shots	Actual Number of Target Shots
ICF	LLE	110	111
	LANL	11	12
	SNL	11	8
ICF Subtotal		132	131
HED	LLE	33	25
	LANL	22	27
	LLNL	55	43
	SNL	11	11
HED Subtotal		121	106
LBS	LLE	22	18
	LLNL	27.5	29
LBS Subtotal		49.5	47
NLUF		22	23
Calibration		0	25
Grand Total		324.5	332

NLUF: National Laser Users Facility

Table II: OMEGA EP Laser System target shot summary for Q2 FY22.

Program	Laboratory	Planned Number of Target Shots	Actual Number of Target Shots
ICF	LLE	24.5	38
	LLNL	14	11
ICF Subtotal		38.5	49
HED	LLE	7	7
	LANL	14	16
	LLNL	28	29
HED Subtotal		49	52
LBS	LLE	14	22
	LLNL	14	23
LBS Subtotal		28	45
CMAP		14	16
LaserNetUS		14	18
NLUF		28	38
Calibration	LLE	0	20
Grand Total		171.5	238

CMAP: Center for Matter at Atomic Pressures

Publications and Conference Presentations

Publications

C. H. Allen, M. Oliver, L. Divol, O. L. Landen, Y. Ping, M. Scholmerich, R. Wallace, R. Earley, W. Theobald, T. G. White, and T. Döppner, "Toward an Integrated Platform for Characterizing Laser-Driven, Isochorically Heated Plasmas with 1 mm Spatial Resolution," Appl. Opt. **61**, 1987 (2022).

P. T. Campbell, C. A. Walsh, B. K. Russell, J. P. Chittenden, A. Crilly, G. Fiksel, L. Gao, I. V. Igumenshchev, P. M. Nilson, A. G. R. Thomas, K. Krushelnick, and L. Willingale, "Measuring Magnetic Flux Suppression in High-Power Laser-Plasma Interactions," Phys. Plasmas **29**, 012701 (2022).

T. J. B. Collins, C. Stoeckl, R. Epstein, W. A. Bittle, C. J. Forrest, V. Yu. Glebov, V. N. Goncharov, D. R. Harding, S. X. Hu, D. W. Jacobs-Perkins, T. Z. Kosc, J. A. Marozas, C. Mileham, F. J. Marshall, S. F. B. Morse, P. B. Radha, S. P. Regan, B. Rice, T. C. Sangster, M. J. Shoup III, W. T. Shmayda, C. Sorce, W. Theobald, and M. D. Wittman, "Causes of Fuel–Ablator Mix Inferred from Modeling of Monochromatic Time-Gated Radiography of OMEGA Cryogenic Implosions," Phys. Plasmas **29**, 012702 (2022).

C. Dorrer and M. Spilatro, "Spectral and Temporal Shaping of Spectrally Incoherent Pulses in the Infrared and Ultraviolet," Opt. Express **30**, 4942 (2022).

M. Formanek, D. Ramsey, J. P. Palastro, and A. Di Piazza, "Radiation Reaction Enhancement in Flying Focus Pulses," Phys. Rev. A **105**, L020203 (2022).

A. M. Hansen, K. L. Nguyen, D. Turnbull, B. J. Albright, R. K. Follett, R. Huff, J. Katz, D. Mastrosimone, A. L. Milder, L. Yin, J. P. Palastro, and D. H. Froula, "Cross-Beam Energy Transfer Saturation: Ion Heating and Pump Depletion," Plasma Phys. Control. Fusion **64**, 034003 (2022).

G. W. Jenkins, C. Feng, and J. Bromage, "Energy Scaling Beyond the Gas Ionization Threshold with Divided-Pulse Nonlinear Compression," Opt. Lett. **47**, 1450 (2022).

V. V. Karasiev, D. I. Mihaylov, and S. X. Hu, "Meta-GGA Exchange-Correlation Free Energy Density Functional to Increase the Accuracy of Warm Dense Matter Simulations," Phys. Rev. B **105**, L081109 (2022).

M. F. Kasim, D. Watson-Parris, L. Deaconu, S. Oliver, P. Hatfield, D. H. Froula, G. Gregori, M. Jarvis, S. Khatiwala, J. Korenaga, J. Topp-Mugglestone, E. Viezzer, and S. M. Vinko, "Building High Accuracy Emulators for Scientific Simulations with Deep Neural Architecture Search," Mach. Learn.: Sci. Technol. **3**, 015013 (2022).

R. G. Kraus, R. J. Hemley, S. J. Ali, J. L. Belof, L. X. Benedict, J. Bernier, D. Braun, R. E. Cohen, G. W. Collins, F. Coppari, M. P. Desjarlais, D. Fratanduono, S. Hamel, A. Krygier, A. Lazicki, J. Mcnaney, M. Millot, P. C. Myint, M. G. Newman, J. R. Rygg, D. M. Sterbentz, S. T. Stewart, L. Stixrude, D. C. Swift, C. Wehrenberg, and J. H. Eggert, "Measuring the Melting Curve of Iron at Super-Earth Core Conditions," Science **375**, 202 (2022).

M. C. Marshall, M. G. Gorman, D. N. Polsin, J. H. Eggert, M. K. Ginnane, J. R. Rygg, G. W. Collins, and L. D. Leininger, "Diamond Formation in Double-Shocked Epoxy to 150 GPa," J. Appl. Phys. **131**, 085904 (2022).

J. Meinecke, P. Tzeferacos, J. S. Ross, A. F. A. Bott, S. Feister, H.-S. Park, A. R. Bell, R. Blandford, R. L. Berger, R. Bingham, A. Casner, L. E. Chen, J. Foster, D. H. Froula, C. Goyon, D. Kalantar, M. Koenig, B. Lahmann, C.-K. Li, Y. Lu, C. A. J. Palmer, R. D. Petrasso, H. Poole, B. Remington, B. Reville, A. Reyes, A. Rigby, D. Ryu, G. Swadling, A. Zylstra, F. Miniati, S. Sarkar, A. A. Schekochihin, D. Q. Lamb, and G. Gregori, "Strong Suppression of Heat Conduction in a Laboratory Replica of Galaxy-Cluster Turbulent Plasmas," Sci. Adv. **8**, eabj6799 (2022).

S. F. Nwabunwanne and W. R. Donaldson, "Interdigitated Electrode Geometry Variation and External Quantum Effi-

ciency of GaN/AlGaN–Based Metal–Semiconductor–Metal UV Photodetectors," Proc. SPIE **12001**, 120010F (2022).

J. J. Pilgram, M. B. P. Adams, C. G. Constantin, P. V. Heuer, S. Ghazaryan, M. Kaloyan, R. S. Dorst, D. B. Schaeffer, P. Tzeferacos, and C. Niemann, "High Repetition Rate Exploration of the Bierman Battery Effect in Laser Produced Plasmas Over Large Spatial Regions," High Power Laser Sci. Eng. **10**, e13 (2022).

N. R. Shaffer and C. E. Starrett, "Dense Plasma Opacity via the Multiple-Scattering Method," Phys. Rev. E **105**, 015203 (2022).

T. T. Simpson, D. Ramsey, P. Franke, K. Weichman, M. V. Ambat, D. Turnbull, D. H. Froula, and J. P. Palastro, "Spatiotemporal Control of Laser Intensity Through Cross-Phase Modulation," Opt. Express **30**, 9878 (2022).

G. F. Swadling and J. Katz, "Novel Design for a Polarizing DUV Spectrometer Using a Wollaston Prism and Its Application as a Diagnostic for Measuring Thomson Scattering Data in the Presence of Strong Self-Emission Backgrounds," Rev. Sci. Instrum. **93**, 013501 (2022).

W. Theobald, D. Cao, R. C. Shah, C. A. Thomas, I. V. Igumenshchev, K. A. Bauer, R. Betti, M. J. Bonino, E. M. Campbell, A. R. Christopherson, K. Churnetski, D. H. Edgell, C. J. Forrest, J. A. Frenje, M. Gatu Johnson, V. Yu. Glebov, V. N. Goncharov, V. Gopalswamy, D. R. Harding, S. X. Hu,

S. T. Ivancic, D. W. Jacobs-Perkins, R. T. Janezic, T. Joshi, J. P. Knauer, A. Lees, R. W. Luo, O. M. Mannion, F. J. Marshall, Z. L. Mohamed, S. F. B. Morse, D. Patel, J. L. Peebles, R. D. Petrasso, P. B. Radha, H. G. Rinderknecht, M. J. Rosenberg, S. Sampat, T. C. Sangster, W. T. Shmayda, C. M. Shuldberg, A. Shvydky, C. Sorce, C. Stoeckl, M. D. Wittman, and S. P. Regan, "Enhanced Laser-Energy Coupling with Small-Spot Distributed Phase Plates (SG5-650) in OMEGA DT Cryogenic Target Implosions," Phys. Plasmas **29**, 012705 (2022).

A. J. White, L. A. Collins, K. Nichols, and S. X. Hu, "Mixed Stochastic-Deterministic Time-Dependent Density Functional Theory: Application to Stopping Power of Warm Dense Carbon," J. Phys.: Condens. Matter **34**, 174001 (2022).

S. Zhang, D. E. Fratanduono, M. C. Marshall, J. R. Rygg, A. E. Lazicki, A. Shvydky, D. Haberberger, V. N. Goncharov, T. R. Boehly, G. W. Collins, and S. X. Hu, "Species Separation in Polystyrene Shock Release Evidenced by Molecular-Dynamics Simulations and Laser-Drive Experiments," Phys. Rev. Research **4**, 013126 (2022).

S. Zhang, M. A. Morales, R. Jeanloz, M. Millot, S. X. Hu, and E. Zurek, "Nature of the Bonded-to-Atomic Transition in Liquid Silica to TPa Pressures," J. Appl. Phys. **131**, 071101 (2022).

D. Zhao, R. Betti, and H. Aluie, "Scale Interactions and Anisotropy in Rayleigh–Taylor Turbulence," J. Fluid Mech. **930**, A29 (2022).

Forthcoming Publications

S.-W. Bahk, I. A. Begishev, R. Roides, C. Mileham, R. Cuffney, C. Feng, B. M. Webb, C. Jeon, M. Spilatro, S. Bucht, C. Dorrer, and J. Bromage, "Effect of the Pump Beam Profile and Wavefront on the Amplified Signal Wavefront in Optical Parametric Amplifiers," to be published in Optics Express.

A. Bose, J. Peebles, C. A. Walsh, J. A. Frenje, N. V. Kabadi, P. J. Adrian, G. D. Sutcliffe, M. Gatu Johnson, C. A. Frank, J. R. Davies, R. Betti, V. Yu. Glebov, F. J. Marshall, S. P. Regan, C. Stoeckl, E. M. Campbell, H. Sio, J. Moody, A. Crilly, B. D. Appelbe, J. P. Chittenden, S. Atzeni, F. Barbato, A. Forte, C. K. Li, F. H. Séguin, and R. D. Petrasso, "Effect of Strongly Magnetized Electrons and Ions on Heat Flow and Symmetry of Inertial Fusion Implosions," to be published in Physical Review Letters.

G. W. Jenkins, C. Feng, and J. Bromage, "Simultaneous Contrast Improvement and Temporal Compression Using Divided-Pulse Nonlinear Compression," to be published in Optics Express.

D. Kim, R. F. Smith, I. K. Ocampo, F. Coppari, M. C. Marshall, M. K. Ginnane, J. K. Wicks, S. J. Tracy, M. Millot, A. Lazicki, J. R. Rygg, J. H. Eggert, and T. S. Duffy, "Structure and Density of Silicon Carbide to 1.5 TPa and Implications for Extrasolar Planets," to be published in Nature Communications.

T. Z. Kosc, H. Huang, T. J. Kessler, and S. G. Demos, "Angular Dependence of the Transverse Raman Scattering in KDP and DKDP in Geometries Suitable for Beam Polarization Control," to be published in Optics Express.

L. S. Leal, A. V. Maximov, E. C. Hansen, J. R. Davies, D. H. Barnak, J. L. Peebles, K. M. Woo, P. V. Heuer, A. B. Sefkow, and R. Betti, "The Effect of Laser Preheat in Magnetized Liner Inertial Fusion at OMEGA," to be published in Physics of Plasmas.

R. W. Paddock, H. Martin, R. T. Ruskov, R. H. H. Scott, W. Garbett, B. M. Haines, A. B. Zylstra, E. M. Campbell, T. J. B. Collins, R. S. Craxton, C. A. Thomas, V. N. Goncharov, R. Aboushelbaya, Q. S. Feng, M. W. von der Leyen, I. Ouatu, B. T. Spiers, R. Timmis, R. H. W. Wang, and P. A. Norreys, "Pathways Towards Break Even for Low Convergence Ratio Direct-Drive Inertial Confinement Fusion," to be published in the Journal of Plasma Physics.

D. N. Polsin, A. Lazicki, X. Gong, S. J. Burns, F. Coppari, L. E. Hansen, B. J. Henderson, M. F. Huff, M. I. McMahon, M. Millot, R. Paul, R. F. Smith, J. H. Eggert, G. W. Collins, and J. R. Rygg, "Structural Complexity in Ramp-Compressed Sodium to 480 GPa," to be published in Nature Communications.

G. F. Swadling, C. Bruulsema, W. Rozmus, and J. Katz, "Quantitative Assessment of Fitting Errors Associated with Streak Camera Noise in Thomson Scattering Data Analysis," to be published in Review of Scientific Instruments.

Conference Presentations

E. M. Campbell, "Perspectives on Inertial Fusion Energy," presented at LLE Research and Review, 14 January 2022.

———

S. F. Nwabunwanne and W. R. Donaldson, "Interdigitated Electrode Geometry Variation and External Quantum Efficiency of GaN/AlGaN-Based Metal–Semiconductor–Metal UV Photodetectors," presented at Photonics West 2022, San Francisco, CA, 22–27 January 2022.

———

P. V. Heuer, S. Feister, N. A. Murphy, and J. R. Davies, "Open Source Software and Data Formats for High-Energy-Density Physics," presented at Laser-Plasma–Accelerator Control Systems and Machine Learning, virtual, 24–28 January 2022.

———

R. B. Spielman, E. M. Campbell, C. Deeney, P. Tzeferacos, and J. D. Zuegel, "Short-Pulse Lasers for Directed-Energy Hypersonic Defense, Swarms, and More," presented at the Visit of J. Stiles, Rochester, NY, 26 January 2022.

———

The following presentations were made at the National Ignition Facility and Jupiter Laser Facility User Meeting, Livermore, CA, 7–9 February 2022:

A. Armstrong, A. Reyes, M. B. P. Adams, P. Farmakis, E. C. Hansen, Y. Lu, D. Michta, K. Moczulski, D. Q. Lamb, and

P. Tzeferacos, "Implementation and Verification of Braginskii Viscosity in the *FLASH* Code."

L. Ceurvorst, L. Masse, S. F. Khan, D. Martinez, N. Izumi, V. Smalyuk, T. Goudal, V. Bouffetier, A. Casner, B. Canaud, V. N. Goncharov, and I. V. Igumenshchev, "Observing the Effects of Ablation and Perforation on the Deeply Nonlinear Rayleigh–Taylor Instability."

G. W. Collins, "Extreme Matters: Pressure to Explore New Worlds and Revolutionary States of Matter."

P. Farmakis, M. McMullan, A. Reyes, J. Laune, M. B. P. Adams, A. Armstrong, E. C. Hansen, Y. Lu, D. Michta, K. Moczulski, D. Q. Lamb, and P. Tzeferacos, "Expanding the Tabulated Equation-of-State Implementations in the *FLASH* Code of the *SESAME* Database."

Y. Lu, S. Feister, J. Meinecke, F. Miniati, G. Gregori, A. Bott, A. Reyes, E. C. Hansen, J. T. Laune, B. Reville, J. S. Ross, D. Q. Lamb, and P. Tzeferacos, "Numerical Modeling of Laser-Driven Plasma Experiments Aiming to Study Turbulent Dynamo and Thermal Conduction at the National Ignition Facility."

K. Moczulski, A. Reyes, M. B. P. Adams, A. Armstrong, P. Farmakis, E. Hansen, Y. Lu., D. Michta, D. Q. Lamb, and P. Tzeferacos, "Implementation and Verification of LC Circuit for Z-Pinch *FLASH* Simulations."

D. N. Polsin, G. W. Collins, J. R. Rygg, X. Gong, M. Huff, M. K. Ginnane, M. McMahon, E. Zurek, A. Lazicki, S. Bonev, M. Gorman, R. Briggs, J. H. Eggert, and J. Wark,

"Transforming Simple Metals to Topological Insulators: Sodium to 18 Mbar."

———————

V. Gopalaswamy, R. Betti, J. P. Knauer, D. Patel, A. Lees, A. R. Christopherson, K. M. Woo, C. A. Thomas, D. Cao, O. M. Mannion, R. C. Shah, C. J. Forrest, Z. L. Mohamed, C. Stoeckl, V. Yu. Glebov, S. P. Regan, D. H. Edgell, M. J. Rosenberg, I. V. Igumenshchev, P. B. Radha, K. S. Anderson, J. R. Davies, T. J. B. Collins, V. N. Goncharov, E. M. Campbell, R. Janezic, D. R. Harding, M. J. Bonino, S. Sampat, S. F. B. Morse, M. Gatu Johnson, R. D. Petrasso, C. K. Li, and J. A. Frenje, "Fusion Energy via Laser-Driven Inertial Confinement," presented at Reed College Physics Seminar, virtual, 9 February 2022.

———————

E. M. Campbell, "Perspectives on Inertial Fusion Energy," presented at the Rochester Institute of Technology Spring Seminar, Rochester, NY, 10 February 2022.

———————

W. Theobald, "LLE is Leading Innovative ICF/IFR Diagnostic Development, which is Amplified Through Participation in the National Diagnostics Working Group," presented at the Workshop on New Inertial Fusion Energy/High-Energy-Density Physics Laser Facility, virtual, 10 February 2022.

———————

V. V. Karasiev, D. I. Mihaylov, S. X. Hu, S. B. Trickey, and J. W. Dufty, "Meta-GGA Exchange-Correlation Free-Energy Density Functional: Achieving Unprecedented Accuracy for Warm-Dense-Matter Simulations," presented at the 61st Sanibel Symposium, St. Simons Island GA, 13–18 February 2022.

———————

J. D. Zuegel, "High-Energy Lasers for Driving Dynamic Materials Experiments," presented at the NNSA Advanced Photon Sources Sector Opportunities Workshop, virtual, 15–17 February 2022.

———————

E. M. Campbell, "Perspectives on Inertial Fusion Energy," presented at the PB11 Science Seminar, virtual, 17 February 2022.

———————

C. Deeney, "National Nuclear Security: 21st Century Science and Technology Perspectives," presented at the World Affairs Council, West Palm Beach, FL, 21 February 2022.

———————

D. H. Froula, "Thomson Scattering from a Different Perspective," presented at the Oxford Seminar, Oxford, UK, 21 February 2022.

———————

J. D. Zuegel, "Kilojoule Lasers for Dynamic Compression Studies," presented at Science with High-Power Lasers, PETRA IV Workshop, virtual, 22–23 February 2022.

———————

The following presentations were made at the Inertial Fusion Energy Science and Technology Workshop, virtual, 22–24 February 2022:

V. N. Goncharov, "Inertial Fusion Energy Target Designs with Advanced Laser Technologies."

J. D. Zuegel, "A Broad View of Solid-State Laser Drivers for Inertial Fusion Energy."

———————

E. M. Campbell, "LLE Perspective," presented at the Office of Experimental Sciences Executives Meeting, virtual, 24 February 2022.

———————

J. P. Palastro, "Research at the Laboratory for Laser Energetics," presented at the Physical Sciences and Astronomy Recruitment Event, Rochester, NY, 25 February 2022.

———————

E. M. Campbell, "Perspectives on Inertial Fusion Energy," presented at the Plasma Science and Fusion Center Seminar, virtual, 7 March 2022.

———————

The following presentations were made at the Ecosystem for Collaborative Leadership and Inclusive Innovation in Plasma Science and Engineering, Alexandria, VA, 9–11 March 2022:

G. W. Collins, "Extreme Matters: Pressures to Explore New Worlds and Revolutionary States of Matter."

P. Tzeferacos, "Laser-Driven Experiments Shed New Light on Magnetized Turbulence and Fluctuation Dynamo in Astrophysical Plasmas."

J. D. Zuegel, "Multi-Petawatt Physics Prioritization (MP3) Workshop."

———

The following presentations were made at Matter in Extreme Conditions from Material Science to Planetary Physics, Montgenevre, France, 12–19 March 2022:

D. A. Chin, P. M. Nilson, D. T. Bishel, R. Paul, E. Smith, X. Gong, M. K. Ginnane, B. J. Henderson, D. N. Polsin, S. X. Hu, J. R. Rygg, G. W. Collins, D. Trail, A. Amouretti, M. Harmand, O. Mathon, R. Torchio, J. J. Ruby, F. Coppari, A. Coleman, and Y. Ping, "X-Ray Absorption Spectroscopy Temperature Measurements at High-Energy-Density Conditions."

D. H. Froula, "Thomson Scattering from a Different Perspective."

S. X. Hu, V. V. Karasiev, P. M. Nilson, D. T. Bishel, D. A. Chin, K. Nichols, R. Paul, R. Goshadze, M. Ghosh, J. Hinz, S. Zhang, D. I. Mihaylov, G. W. Collins, N. Shaffer, L. A. Collins, A. J. White, V. Recoules, N. Brouwer, M. Torrent, I. E. Golovkin, M. Gu, T. Walton, and S. B. Hansen, "Understanding Matter in Extreme Conditions with *ab initio* Calculations."

Z. K. Sprowal, L. E. Hansen, M. F. Huff, D. N. Polsin, D. G. Hicks, T. R. Boehly, J. R. Rygg, and G. W. Collins, "Accessing High Density States in D_2 Using Double Shock."

———

The following presentations were made at the APS March Meeting, Chicago, IL, 14–18 March 2022:

M. Ghosh, S. Zhang, and S. X. Hu, "*Ab Initio* Investigation of the Cooperative Diffusion in Body-Centered-Cubic Iron Under Inner-Core Conditions of Earth and Super-Earth Exoplanets."

R. M. N. Goshadze, V. V. Karasiev, D. I. Mihaylov, and S. X. Hu, "Equation of State of Metallization of CH Along the Principal Hugoniot."

B. J. Henderson, M. C. Marshall, J. R. Rygg, D. N. Polsin, L. E. Hansen, M. K. Ginnane, and G. W. Collins, "Silica Aerogel as a Bright Optical Source for High-Energy-Density Experiments."

M. Huff, J. R. Rygg, G. W. Collins, T. R. Boehly, D. N. Polsin, M. Nakajima, B. J. Henderson, M. C. Marshall, T. A. Suer, D. E. Fratanduono, M. Millot, R. F. Smith, C. A. McCoy, and L. E. Hansen, "Measurements of Sound Speed in Iron Shock Compressed to ~3000 GPa."

R. Paul, S. Zhang, V. V. Karasiev, and S. X. Hu, "Thermal-Induced Evolution of Magnetic Properties of FeO_2 Under High Pressures."

S. Zhang, M. A. Morales, R. Jeanloz, M. Millot, S. X. Hu, and E. Zurek, "Nature of the Bonded-to-Atomic Transition in Liquid Silica at Extreme Conditions."

———

M. Ghosh, S. Zhang, and S. X. Hu, "An Exotic Phase of Iron in Earth's Inner Core: A First-Principles–Based Study on the Mechanism of Cooperative Diffusion in Body-Centered-Cubic Iron," presented at the University of Rochester Graduate Education and Postdoctoral Affairs Research Symposium, Rochester, NY, 23 March 2022.

———

C. Deeney, "The Laboratory for Laser Energetics: Progress in Science and Technology," presented at the Plasma Science and Fusion Center Seminar, virtual, 28 March 2022.